First Single Particle Measurements of the Proton and Antiproton Magnetic Moments

First Single Particle Measurements of the Proton and Antiproton Magnetic Moments

A thesis presented

by

Jack Michael DiSciacca

to

The Department of Physics

in partial fulfillment of the requirements

for the degree of

Doctor of Philosophy

in the subject of

Physics

Harvard University

Cambridge, Massachusetts

May 2013

Thesis advisor

Gerald Gabrielse

Author

Jack Michael DiSciacca

First Single Particle Measurements of the Proton and Antiproton Magnetic Moments

Abstract

We report a new comparison of the proton (p) and antiproton ($\bar{p}$) magnetic moments. In nuclear magnetons, $\mu_p/\mu_N = 2.792\ 846\ (7)$ [2.5 ppm], while $\mu_{\bar{p}}/\mu_N = 2.792\ 845\ (12)$ [4.4 ppm]. The unprecedented accuracy of the antiproton measurement is 680 times more precise than previous work. These first single-particle measurements provide a stringent test of CPT invariance. Our comparison, $\mu_{\bar{p}}/\mu_p = -1.000\ 000\ (5)$ [5.0 ppm], is consistent with the prediction of the CPT theorem. We also report the observation of a single proton spin flip, opening a path to improved precision by an additional factor of 10^3 or 10^4.

Contents

List of Figures

List of Tables

Publications

1. **Resolving an Individual One-Proton Spin Flip to Determine a Proton Spin State**
   J. DiSciacca, M. Marshall, K. Marable, and G. Gabrielse,
   Phys. Rev. Lett. **110**, 140406 (2013).

2. **One-Particle Measurement of the Antiproton Magnetic Moment**
   J. DiSciacca, M. Marshall, K. Marable, G. Gabrielse, S. Ettenauer, E. Tardiff, R. Kalra, D. W. Fitzakerley, M. C. George, E. A. Hessels, C. H. Story, M. Weel, D. Grzonka, W. Oelert, and T. Sefzick, *Phys. Rev. Lett.* **110**, 130801 (2013).

3. **Direct Measurement of the Proton Magnetic Moment**
   J. DiSciacca and G. Gabrielse, *Phys. Rev. Lett.* **108**, 153001 (2012).

4. **Self-Excitation and Feedback Cooling of an Isolated Proton**
   N. Guise, J. DiSciacca, and G. Gabrielse, *Phys. Rev. Lett.* **104**, 143001 (2010).

Acknowledgments

This research was only possible with the contributions and dedication of many people. I would first like to thank Jerry Gabrielse for his continued support, motivation and guidance throughout this work. I am grateful for the opportunity to work on this research project, which has been interesting, challenging and rewarding.

It has been my pleasure and privilege to work with wonderful colleagues during my graduate studies. I would like to thank Nick Guise who introduced me to the lab and the experiment. We worked closely for several years and I learned much from Nick. His interest in the project as well as his continued willingness to discuss questions and ideas have been tremendously helpful.

I am very grateful to Mason Marshall and Kathryn Marable who were both brave enough to move with the experiment to CERN. Their good cheer and skill were indispensable this past year as we worked together on the antiproton measurement. As I now leave the experiment in their capable hands, I look forward to seeing the results as they guide the project forward.

For the antiproton work, I had the privilege of joining the ATRAP collaboration where I benefited from the hard work of many colleagues. I worked most closely with Dan Fitzakerley and Stephan Ettenauer. Dan was instrumental in getting the experiment interfaced with the AD and it has been my pleasure to see Stephan take over the experimental operation as I have written my thesis.

At Harvard, I overlapped with many graduate students, postdocs and undergraduates in our lab. I would like to thank Josh Dorr, Elise Novitski, Phil Richerme, Steve Kolthammer, Rob McConnell, Yulia Gurevich, Shannon Fogwell Hoogerheide, Josh Goldman, Dave Hanneke, David Le Sage, Ben Spaun, Paul Hess, Kyle Flanagan, Rita

Kalra, Eric Tardiff, and Nate Jones. My fellow labmates provided both inspiration from their good examples as well as useful knowledge on more technical questions.

We are very fortunate to have a gifted support staff at Harvard. The expertise and kindness of Jan Ragusa, Stan Cotreau, Louis Defeo and Jim MacArthur have been crucial. They have all contributed substantially with their hard work and skill as well as with their smiles and good humor.

I would like to conclude by thanking my family and friends, who have been a constant source of inspiration, encouragement and support. I am grateful to my good friends who have made grad school much more than labwork. Above all, I am thankful for having such a wonderful family, Mom, Dad, Becky, Kevin and especially Renee.

For my parents

Chapter 1

Introduction

In this thesis, we report the first single particle measurements of the proton and antiproton magnetic moments [1, 2]. The antiproton result is a 680-fold improvement in precision, providing a precision test of CPT invariance. Our comparison is consistent with the CPT theorem prediction. In addition to the magnetic moment measurements, we have demonstrated the ability to prepare and measure the spin state by detecting a single spin flip [3]. This opens the path to making improved magnetic moment measurements of both the proton and antiproton with precision at the ppb level, representing a further improvement of 10^3 or 10^4. These measurements are enabled by the high signal-to-noise detection of the proton axial motion with a self-excited oscillator [4].

1.1 The Proton and Antiproton Magnetic Moments

The magnetic moment of a particle is determined by the spin, charge, mass and dimensionless g-factor. Factoring out $\hbar/2$ from the spin, yields the expression for the magnetic moment in terms of a dimensional estimate and the dimensionless g-factor

$$\boldsymbol{\mu} = \frac{g}{2}\frac{q\hbar}{2m}\frac{\boldsymbol{S}}{\hbar/2}\,. \tag{1.1}$$

For the proton and antiproton, the dimensional estimate is the nuclear magneton $\mu_N = e\hbar/(2m_p)$ and the scaled spin is $\boldsymbol{\sigma} = \boldsymbol{S}/(\hbar/2)$. The p and $\bar{p}$ magnetic moments, $\boldsymbol{\mu}_p = \mu_p\boldsymbol{\sigma}$ and $\boldsymbol{\mu}_{\bar{p}} = \mu_{\bar{p}}\boldsymbol{\sigma}$, can now be expressed as

$$\mu_p = \frac{g_p}{2}\mu_N\,, \tag{1.2}$$

$$\mu_{\bar{p}} = -\frac{g_{\bar{p}}}{2}\mu_N\,. \tag{1.3}$$

From this, it is clear that a measurement of $g/2$ for the proton or antiproton provides a measurement of the magnetic moment in units of nuclear magnetons.

The primary results of this thesis are the first direct measurements of the proton and antiproton magnetic moments and the first using a single particle [1, 2]. The results are

$$\frac{\mu_p}{\mu_N} = \frac{g_p}{2} = 2.792\,846\,(7)\ [2.5\ \text{ppm}], \tag{1.4}$$

$$\frac{\mu_{\bar{p}}}{\mu_N} = -\frac{g_{\bar{p}}}{2} = -2.792\,845\,(12)\ [4.4\ \text{ppm}]. \tag{1.5}$$

The antiproton measurement represents a factor of 680 improvement in precision over exotic atom spectroscopy, where the precision has remained essentially unchanged for the past 25 years [5, 6]. The result is consistent with the CPT theorem prediction

that the magnitudes be the same while the signs are opposite,

$$\mu_{\bar{p}}/\mu_p = -1.000\,000\,(5)\ [5.0\ \text{ppm}], \tag{1.6}$$

$$\mu_{\bar{p}}/\mu_p = -0.999\,999\,2\,(44)\ [4.4\ \text{ppm}]. \tag{1.7}$$

The first is a direct comparison that uses the μ_p measured using the same trap electrodes as the antiproton measurement [1]. The second comparison is indirect, using the more precise μ_p deduced indirectly from three measurements and two theoretical corrections [7, 8].

We also report the first observation of a single proton spin flip [3], opening a path to an improved magnetic moment measurement with precision at the part per billion level, an improvement by an additional factor of 10^3 or 10^4. In our research, we profited from parallel work on proton spin flips [9]. This independent effort yielded a proton magnetic moment measurement with a 8.9 ppm precision consistent with our earlier measurement [10] and a simultaneously reported detection of a single proton spin flip [11].

1.2 History

There has been a long and successful history of magnetic moment measurements for the proton. The first proton measurements by Stern in the early 1930's were carried out using molecular beam techniques at the forefront of atomic physics [12, 13]. Although not realized at the time, the fact that the proton g-factor was substantially different from 2 provided the first evidence of the quark substructure of the proton [14]. Stern's discovery of the proton magnetic moment was recognized with a Noble prize.

Further developments of magnetic resonance with molecular beams by Rabi improved the precision in the following years [15], earning Rabi a Nobel prize the year after Stern was awarded his.

In the following decade, research by Purcell and Bloch led to the development of nuclear magnetic resonance [16, 17]. This work, also recognized by a Nobel prize, led to improved precision in the proton magnetic moment [16]. Further progress was made in the the 1950's when Ramsey and Kleppner developed the hydrogen maser [18, 19]. Contributing to Ramsey's a Nobel prize, the hydrogen maser also was used to make the most precise measurement proton magnetic moment [19, 7]. The current 10 ppb measurement was performed by Kleppner and colleagues in 1972, leading to the current determination of the proton magnetic moment [7, 20]. The history of the precision in the proton and antiproton magnetic moment measurements is shown in Fig. 1.1.

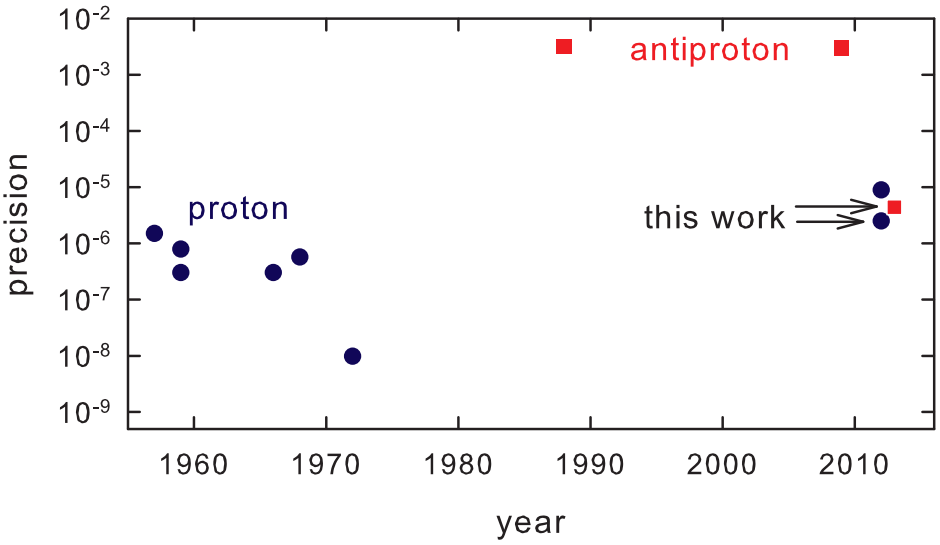

Figure 1.1: The history of the proton and antiproton magnetic moments.

The precise determinations of the proton magnetic moment involved bound protons. As a result, the free-proton magnetic moment has to be extracted from the measured values. In the most precise determination, $\mu_p/\mu_N = g_p/2$ is determined by

$$\frac{\mu_p}{\mu_N} = \frac{g_p}{2} = \frac{g_e}{2}\frac{m_p}{m_e}\frac{\mu_p(H)}{\mu_e(H)}\frac{g_e(H)}{g_e}\frac{g_p}{g_p(H)} \ . \tag{1.8}$$

The experimentally measured quantities are g_e, m_p/m_e, and $\frac{\mu_p(H)}{\mu_e(H)}$. The most accurate of these is the electron g-factor, g_e, measured by our group at Harvard to < 0.001 ppb [21]. The proton-electron mass ratio, m_p/m_e, is also currently known better than 1 ppb level [22] and the proton-electron magnetic moment ratio, $\frac{\mu_p(H)}{\mu_e(H)}$, is known to 10 ppb [7]. There are also two correction terms from theory, $\frac{g_e(H)}{g_e}$ and $\frac{g_p}{g_p(H)}$. These are corrections to the conversion from bound to free g-factors that have been calculated to better than 1 ppb [8]. The current limit to the proton magnetic moment is the proton-electron magnetic moment ratio for hydrogen, this sets the overall precision of $\mu_p/\mu_N = g_p/2 = 2.792\ 847\ 356\ (23)$.

While the techniques used for the proton have been very successful, they are not yet transferable to the antiproton magnetic moment measurement. An alternative method achieved a precision of three parts-per-thousand [5, 6], with a value of $\mu_{\bar{p}}/\mu_n = -g_{\bar{p}}/2 = -2.8005\ (90)$. Exotic atoms of Pb were used within which an antiproton replaces an electron to form a so-called heavy antiprotonic atom [5]. A recent update using antiproton helium achieved a similar precision with $\mu_{\bar{p}}/\mu_n = -g_{\bar{p}}/2 = -2.7862\ (83)$ [6].

1.3 CPT Symmetry

The primary motivation for measuring the proton and antiproton magnetic moments is to test the combined Charge, Parity and Time reversal symmetry (CPT). Charge conjugation is the the exchange of particles and antiparticles. Parity reversal is achieved by inverting the sign of spatial coordinates $\vec{x} \rightarrow -\vec{x}$. Time reversal is similar in that it requires the inversion of time, $t \rightarrow -t$. The CPT theorem states that any local, Lorentz-invariant quantum field theory is invariant under the combined transformation of CPT [23]. Given that the Standard Model is built in the framework of such a quantum field theory, a discovery of CPT violation would be a demonstration of physics beyond the Standard Model.

1.3.1 History

In the past fifty years, the field of physics has seen the discovery of P and CP violation [24, 25]. Until 1956, it was widely believed that the laws of physics were symmetric under parity reversal. However, after a thorough literature review, Lee and Yang found that there was no experimental test of parity violation in the weak force and proposed experiments to investigate this [26]. The experimental discovery of such parity violation followed shortly thereafter, with pioneering work done by Wu [24]. To measure parity violation, Wu and collaborators used a sample of spin polarized ^{60}Co. This species can undergo a β decay, an effect governed by the weak interaction. The experiment detected electrons emitted from the decay. In a strong magnetic field and at cryogenic temperatures, the nuclei remain polarized for several minutes as the sample warms. During this initial time, the sample is polarized and the electrons

were preferentially emitted in the opposite direction as the nuclear spin [24]. This is a violation of parity reversal symmetry because under a parity transformation, the nuclear spin remains unchanged but the direction of the electrons is inverted. For their theoretical work, Lee and Yang were awarded the Nobel prize.

After parity violation was discovered, the combined symmetry of CP was proposed as the true invariant of nature [27]. However, further experimental work by Cronin and Fitch demonstrated CP violation using neutral kaons [25]. In their experiment, Cronin and Fitch measured the decay products of the weak force eigenstates of the neutral kaon, K_S and K_L. The distinction between the two, namely the lifetime, gives rise to the naming scheme for the short and long particles. If these particles were symmetric under CP, K_S and K_L would also be the CP eigenstates, indicating there could be no mixing between the two species.

Using the different lifetimes, Cronin and Fitch prepared a beam of K_L after allowing the beam to travel a distance 300 K_S decay lengths. When measuring the decay products of this purified beam, the signature of K_S decays indicated mixing between the K_L and K_S, providing evidence of CP violation [25]. This work earned Cronin and Fitch the Nobel prize. In the time after this original demonstration, there have been a number of very clear demonstrations of CP violation in the kaon system as well as with B mesons [28, 29]. Furthermore, the presence of CP violation was used by Kobayashi and Maskawa to successfully predict the third generation of quarks [30].

In the Standard model, CPT symmetry is exact. However, there are indications of physics beyond the Standard Model. Some noteworthy examples include the fact that gravity has so far eluded a description consistent with the Standard Model. Another

prominent discrepancy is the asymmetry in the abundance of matter and antimatter. This discrepancy is one motivation for precise comparisons of antimatter and matter particles.

One possible explanation for the matter and antimatter asymmetry is the violation of CPT symmetry. If coupled with violation of baryon number, this can possibly account for the present asymmetry [31]. It should be noted that another such possibility for explaining the matter-antimatter asymmetry involves CP violation, coupled with the baryon number violation as well as thermal non-equilibrium, proposed by Sakharov [32].

The importance of testing the Standard Model as well as a possibly providing an explanation for the matter and antimatter asymmetry has led to a number of experimental tests of CPT invariance [33]. Because we do not have a prediction for where CPT is violated, the general experimental procedure is to perform precision measurements on simple systems achieving strict bounds on quantities such as fractional mass differences or magnetic moment differences for particle and antiparticle pairs.

The current experimental tests of CPT invariance demonstrate an impressive record, the results are all consistent with CPT invariance. The most precise CPT test is currently given by a mass difference measurement in the neutral kaon system [34]. This test is made in the mesonic sector where the mass ratio $|(m_{\bar{K}^0} - m_{K^0})/m_{K^0}|$ has been bounded to be less than 0.6×10^{-18} [34, 33]. In the baryonic sector, the most precise CPT test comes from the charge-to-mass ratio of a single proton and antiproton achieving a precision of 9×10^{-11} [35]. For leptons, the most precise test comes from the electron and positron magnetic moments with a fractional precision

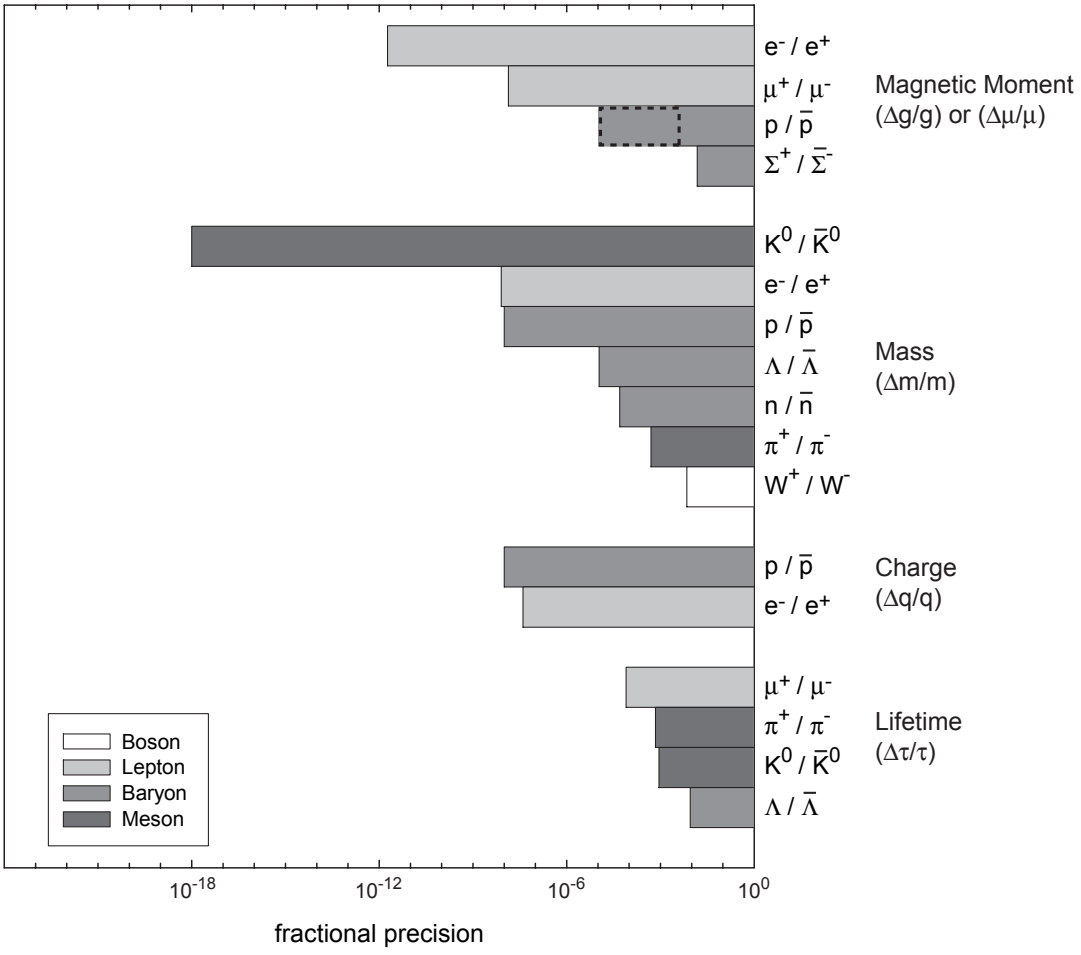

Figure 1.2: Tests of CPT invariance. The dashed box shows the improvement for the proton and antiproton magnetic moment ratio.

of 2×10^{-12} [36]. Figure 1.2 illustrates these and other tests of CPT invariance. The improvement in the proton and antiproton magnetic moment ratio is shown in the dashed box in Fig. 1.2. The result is consistent with CPT invariance with a precision of 4.4×10^{-6} [2].

1.4 Overview of this Work

Chapter 2 introduces the apparatus used for the experimental results presented in this thesis. When I joined the experiment, there was a solid apparatus that Nicholas Guise built as part of his thesis work [4, 37]. I contributed several upgrades to the apparatus, including new detection amplifiers, modifications for antiproton loading, and a new analysis trap in which the proton and antiproton magnetic moments measurements were made, as well as the first observation of single spin flips.

Chapter 3 describes the techniques for detecting and driving a single particle. The chapter provides an overview of the circuits used to damp and amplify the axial and cyclotron signals. The technique of axial feedback to both reduce the temperature and establish the self-excited oscillator is detailed. The process of obtaining a single particle is also described.

Chapter 4 investigates the axial frequency stability. In particular, the focus is on possible sources of instability that come from the cyclotron state. A quadratic dependence of the axial frequency stability and cyclotron state presents one of the most significant hurdles for the experiment. The axial frequency stability achieved enables the scientific results of this thesis.

Chapter 5 describes the proton magnetic moment measurement. The measure-

ment principle and procedure is outlined as well as an overview of the line shapes of the data. Systematic effects are outlined and the contributions to the error in the result are presented. The result is the first single-particle measurement of the proton magnetic moment.

Chapter 6 presents the work with antiprotons. The chapter first focuses on cooling and trapping a single antiproton. The trap used was two times smaller than was used to first demonstrate the trapping and cooling methods [38, 39]. The following work focused on the preliminary experiments for the magnetic moment measurement, such as the magnetic field stability as well as the axial frequency stability in the accelerator hall. The antiproton magnetic moment measurement result achieves a precision of 4.4 ppm, representing a factor of 680 improvement.

Chapter 7 reports the work with single spin flip detection. A framework for analyzing the efficiency and fidelity of such measurements is presented along with the experimental results. A correlation function shows the clear signature of single spin flips. This work opens the path to ppb measurements of the proton and antiproton magnetic moments. Chapter 8 provides a summary of the work presented in this thesis.

Chapter 2

Apparatus and Measurement Principle

The precision in Penning trap measurements is due to a detailed understanding and experimental control of the system. Much work has been devoted to single particle trapping, detection, cooling and systematic studies for precision measurements [40]. Components such as stable magnetic and electric fields, low noise detection and cryogenic techniques are crucial for the measurement. While much work has been done in the field of precision measurements in Penning traps [40], an overview of the most relevant features for antiproton and proton magnetic moment measurements will be outlined.

2.1 The Penning Trap

The Penning trap consists of a superposition of static electric and magnetic fields. The appropriate choice of these fields allows for single particle trapping and detection. A large and homogeneous magnetic field in the z-direction provides radial confinement for ions as they undergo cyclotron orbits around field lines. Confinement parallel to the magnetic field is established using a static electric quadrupole potential, $V \sim 2z^2 - \rho^2$. This potential creates harmonic confinement, resulting in the axial motion of a trapped particle. Using these fields, and cryogenic temperatures to avoid collisions, a particle can be trapped for many months.

The fields and corresponding ion motions in a Penning trap are shown in Fig. 2.1. While the scale is not representative of the actual experimental parameters, it gives a sense for the frequency hierarchy. Section 2.1.1 outlines the experimental frequencies and amplitudes.

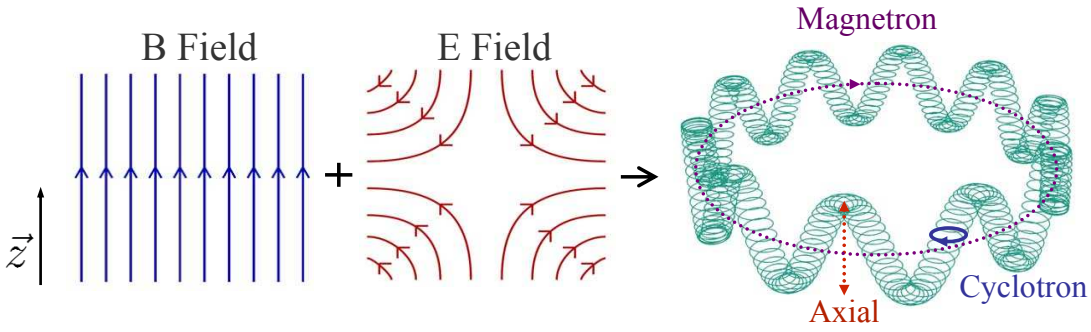

Figure 2.1: The magnetic and electric quadrupole fields combine to create the axial, cyclotron and magnetron orbits for a charged particle in a Penning trap.

The radial component of the electric quadrupole potential is important for two rea-

sons. The first consequence is that it shifts the measured cyclotron frequency from the free space cyclotron frequency. This must be accounted for in magnetic moment measurements, as will be discussed in Section 2.2. The second impact is that the radial term of the electric quadrupole potential is anti-trapping, meaning the resulting magnetron motion is unbound. While, the rate at which the magnetron motion grows is quite slow, meaning the motion is effectively metastable, it is still important to frequently reduce the magnetron radius to ensure it does not increase over time. Reducing the magnetron radius is discussed in more detail in Chapter 3.

2.1.1 Trap Frequencies

The trap frequencies are set by the strengths of the corresponding fields. The cyclotron frequency is set by the strength of the magnetic field, $B\hat{z}$, and the axial frequency is set by the electric field strength. The magnetron frequency is determined by both the magnetic field and electric field strengths. The harmonic axial motion is established using the electric quadrupole field mentioned before, in particular, the field for an ideal quadrupole is given by

$$V = V_0 \frac{z^2 - \rho^2/2}{2d^2} \,. \tag{2.1}$$

The voltage, V_0, is the applied trap voltage and the length scale is determined by the trap geometry. The relations between ρ_0, z_0 and our open-access trap are detailed in reference [41]. The effective trap length scale is defined by,

$$d^2 = \frac{1}{2}\left(z_0^2 + \frac{1}{2}\rho_0^2\right). \tag{2.2}$$

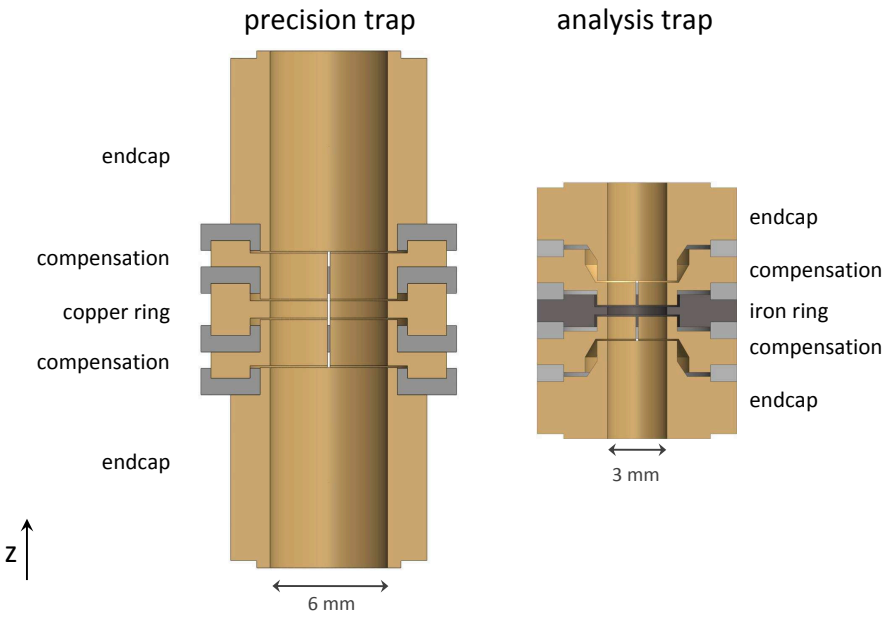

Figure 2.2: The precision and analysis traps.

In general, the potential in an actual Penning trap is not exactly an ideal quadrupole. To better quantify and optimize the potential, we expand it around the center of the trap in Legendre polynomials. Given the reflection symmetry $z \to -z$, we consider only the even terms in the expansion. This gives an expression for the potential in powers of distance from the trap center,

$$V(\mathbf{r}) = \frac{V_0}{2} \sum_{\substack{k=0 \\ \text{even}}}^{\infty} C_k \left(\frac{r}{d}\right)^k P_k\left(cos\,\theta\right) \ . \tag{2.3}$$

The coefficients of this expansion determine how harmonic the trap is. An ideal quadrupole potential would be given by $C_2 = 1$ with all other coefficients zero. The higher order terms add anharmonicity to the axial oscillation, which broadens the axial response. To address this, the trap is designed to be compensated and orthogonal [40, 41]. The compensation comes from two additional electrodes above and below

the ring electrode. The expression for the C_k coefficients below illustrates the ability to use the compensation voltage to tune the C_4 term to zero. The orthogonality of the trap is an experimentally useful feature. The geometry of the trap is chosen such that D_2 is very close to zero, meaning that changes in the axial frequency are suppressed when the anharmonicity is tuned by adjusting the compensation voltage.

$$C_k = C_k^{(0)} + \frac{V_c}{V_0} D_k \ . \tag{2.4}$$

The above expression for the C_k coefficients is determined by the geometry of the trap. Expressions for the $C_k^{(0)}$ and D_k can be found in reference [41]. The voltages V_C and V_0 are related to the voltages we apply to the compensation and ring electrodes, V_{comp} and V_{ring} respectively. For a proton, the relationships between the applied voltages and the expansion voltages are,

$$V_0 = -V_{ring} \ , \tag{2.5}$$

$$V_c = V_{comp} - V_{ring}/2 \ . \tag{2.6}$$

Combining these factors and coefficients, gives the expression for the axial frequency. For purely harmonic motion with the particle on the center axis of the trap, we take $\rho \to 0$ and $C_k \to 0$ for $k > 2$. This gives an axial frequency of

$$\nu_z = \frac{1}{2\pi}\sqrt{\frac{qV_0C_2}{md^2}} \ . \tag{2.7}$$

The anharmonicity causes the axial frequency to have shifts proportional to powers of the ratio of the oscillation amplitude, A, and the trap dimension, d. This ratio illustrates the usefulness of oscillations much smaller than the size of the trap. The two lowest order anharmonic terms are expressed below. We tune C_4 close to zero

with the comp voltage. In addition, open endcap traps have the useful feature that the geometry can be selected to have a compensated, orthogonal trap as well as have C_6 vanish [41]. In practice, how well the trap is orthogonalized depends on machining tolerances, so we expect some small, but non-zero contribution from C_6. As a result, tuning the compensation potential is likely not only tuning $C_4 = 0$, but a combination of C_4 and C_6.

$$\bar{\nu}_z^2(A) = \nu_z^2 \left[1 + \frac{3C_4}{2C_2}\left(\frac{A}{d}\right)^2 + \frac{15C_6}{8C_2}\left(\frac{A}{d}\right)^4 + \ldots\right] \tag{2.8}$$

While the axial frequency is set by the applied voltages, the cyclotron and spin frequencies are set by the magnetic field strength. In free space, that is ignoring the effect of the electric field, the frequencies are given by

$$\nu_c = \frac{qB}{m}\,, \tag{2.9}$$

$$\nu_s = 2\mu B/h = \frac{g}{2}\nu_c\,. \tag{2.10}$$

The addition of the electric field shifts the free space cyclotron frequency to the trap modified cyclotron frequency, ν_+. The trap modified cyclotron frequency is what we can measure in the apparatus, given by

$$\nu_+ = \nu_c - \nu_-\,, \tag{2.11}$$

for the ideal case. In practice, the Brown-Gabrielse invariance theorem is needed to extract the free space cyclotron frequency from the measured trap frequencies [40]. Given possible misalignment between the electric and magnetic fields or the presence of harmonic distortions of the trapping potentials, the free space cyclotron frequency can still be extracted from the three measured trap frequencies [40],

$$f_c = \sqrt{f_+^2 + f_z^2 + f_-^2}. \tag{2.12}$$

This equation allows for high precision measurement of the cyclotron frequency in the presence of unavoidable imperfections. The combined electric and magnetic fields introduces the magnetron motion, ν_-. The magnetron frequency is given by

$$\nu_- = \frac{\nu_z^2}{2\nu_+} \,. \tag{2.13}$$

2.1.2 Experimental Frequencies and Parameters

The frequencies of the motions outlined above set the detection requirements of the experiment. These frequencies can be tuned by changing the trapping potential of the axial trap or by changing the magnetic field. The frequencies used for the experiment are detailed in Table 2.1. For a proton and antiproton, the axial and

Table 2.1: The approximate frequencies for the precision and analysis traps.

motion	precision trap	analysis trap
magnetron	1.9 kHz	5.0 kHz
axial	570 kHz	920 kHz
cyclotron	86 MHz	79 MHz
spin	240 MHz	220 MHz

cyclotron frequencies are in the 1 MHz and 100 MHz range respectively. In practice, we typically measure the RF noise spectrum in the environment of the experiment and determine the optimum frequencies for the particle. For the cyclotron frequency, this was informed by the radio stations that dominate the spectrum above 88.1 MHz at Harvard. For the axial frequency in the 1 MHz range, we tune away from the AM radio stations. Avoiding these stations is important because they can drive the

particle motion despite careful shielding and filtering. The magnetic field and voltages determine the frequencies. The values typically used for the experiment are listed in Table 2.2.

Table 2.2: The trap voltages, magnetic fields and dimensions. The trap voltage is negative for protons. The dimensions are given for room temperature.

parameter	precision trap	analysis trap
magnetic Field	5.7 T	5.2 T
trap voltage (V_0)	-1.5 V	-1.2 V
trap radius (ρ_0)	3.0 mm	1.5 mm
trap height (z_0)	2.930 mm	1.465 mm
trap size (d)	2.578 mm	1.289 mm

2.1.3 Oscillation Amplitudes and Quantum Numbers

The oscillation amplitudes can be extracted from the classical energies given by the amplitudes of the orbits. The expressions for the energies of the cyclotron, axial and magnetron motions respectively, E_c, E_z, and E_ℓ are below. Equating the cyclotron and axial energies with $k_B T$, the thermal amplitudes can be extracted. Given the unbound nature of the magnetron motion, a coupling to 4 K would continually increase the radius. As a result, this motion is intentionally left uncoupled except for a sideband coupling, discussed in Chapter 3. The amplitudes for 4 K cyclotron and axial motions are estimated in Table 2.3. The magnetron radius is given by the sideband cooling limit discussed in Sec. 3.5.

$$E_c = m\omega_+^2\rho_c^2/2\,. \tag{2.14}$$

$$E_z = m\omega_z^2 z^2/2\,. \tag{2.15}$$

$$E_\ell = \frac{m}{2}\left(\omega_m^2 - \frac{\omega_z^2}{2}\right)\rho_m^2 \approx \frac{-m\omega_z^2\rho_m^2}{4}\,. \tag{2.16}$$

Table 2.3: The approximate oscillation amplitudes for the precision and analysis traps. The cyclotron and axial values are for thermal equilibrium at 4 K. The magnetron radius is from sideband cooling that equalizes the average magnetron and axial quantum numbers (Sec. 3.5).

motion	precision trap (μm)	analysis trap (μm)
magnetron	$\rho_m \approx 6$	$\rho_m \approx 5$
axial	$z \approx 70$	$z \approx 40$
cyclotron	$\rho_c \approx 0.5$	$\rho_c \approx 0.5$

It is useful to introduce the quantum mechanical framework for the motions of the trapped particle. This is particularly important for the magnetic moment measurement that employs spin flips and cyclotron jumps. The axial, magnetron and cyclotron motions of the trapped particle are all harmonic motions. As a result, the energies E_c, E_z, and E_ℓ for the cyclotron, axial and magnetron motions respectively, have nearly the typical harmonic oscillator ladder. The negative magnetron energy indicates the motion is unbound.

$$E_c = \hbar\omega_+ \left(n + \frac{1}{2}\right) \tag{2.17a}$$

$$E_z = \hbar\omega_z \left(k + \frac{1}{2}\right) \tag{2.17b}$$

$$E_\ell = -\hbar\omega_m \left(\ell + \frac{1}{2}\right) \tag{2.17c}$$

Equating these energies with $k_B T$ gives the approximate average quantum numbers. Again, for the magnetron case, the quantum number is given after SB cooling, which is simply the axial quantum number. For the axial motion in the precision trap, 4 K translates to a quantum number of 150,000. In the analysis trap, the higher axial frequency gives 90,000. The magnetron quantum numbers for a SB cooled particle are the same. The cyclotron state in both traps is roughly 1000 at 4 K.

2.1.4 The Apparatus and Trap Wiring

The magnetic field for the experiment is created using a superconducting solenoid. As seen in Fig. 2.4, this is the primary contributor to the size of the experiment. The magnet has two dedicated cryogen spaces to keep the coils at 4 K. A liquid nitrogen reservoir radiatively shields the liquid helium dewar that holds the coils. The helium dewar has a capacity of 50 liters and the liquid nitrogen dewar holds 80 liters. We typically fill the magnet helium dewar before the level reaches the coils, before 80 percent, this translates to filling the magnet every 2-3 weeks. The liquid nitrogen is filled every 2-3 weeks..

The trap is lowered into the bore of the magnet and requires two additional cryogen spaces. The auxiliary dewar, located at the bottom of the magnet, holds liquid

nitrogen and cools the inner bore of the magnet. The auxiliary dewar has a capacity of approximately 60 liters requiring a fill every 6 days or so. Having the bore of the magnet at liquid nitrogen temperature greatly decreases the radiative load on the 4 K experiment. The experiment liquid helium dewar comprises the middle section of the experiment. This 4 liter dewar is made from OFE copper to reduce temperature gradients as the helium level drops within it.

The electrodes are held in a trap vacuum enclosure that is evacuated at room temperature to approximately 1×10^{-7} Torr and sealed with a cold weld of an annealed OFE copper pump out port made using a pinch-off tool[1]. The trap is conduction cooled by a thermal connection to the experiment helium dewar. Cryopumping of the closed volume created a pressure better than 5×10^{-17} Torr in a similar system [42]. This low pressure is particularly important for work with antiprotons to avoid annihilation with background gas. With this experiment, we were able to hold a single antiproton for over a month.

Just above the trap can region of the experiment is the tripod which holds the cold electronics. In this region, the signals from the particle are amplified and sent out to room temperature on stainless microcoax lines. Twisted pairs of thin constantan wire carrying the DC biases for the trap electrodes or the low frequency drives are broken out to filters and copper twisted pairs before connecting to the corresponding feedthrough pin at the top of the trap can. Higher frequency drives, such as the cyclotron and spin flip drives, are sent down stainless microcoax lines to the tripod.

Filtering these lines is particularly important for this experiment. Given the small

[1]Team Company Inc. Pinch-off Systems 2 Sewall Ave., Brookline, MA 617 232-1860 Part Number MCI-38A-T1

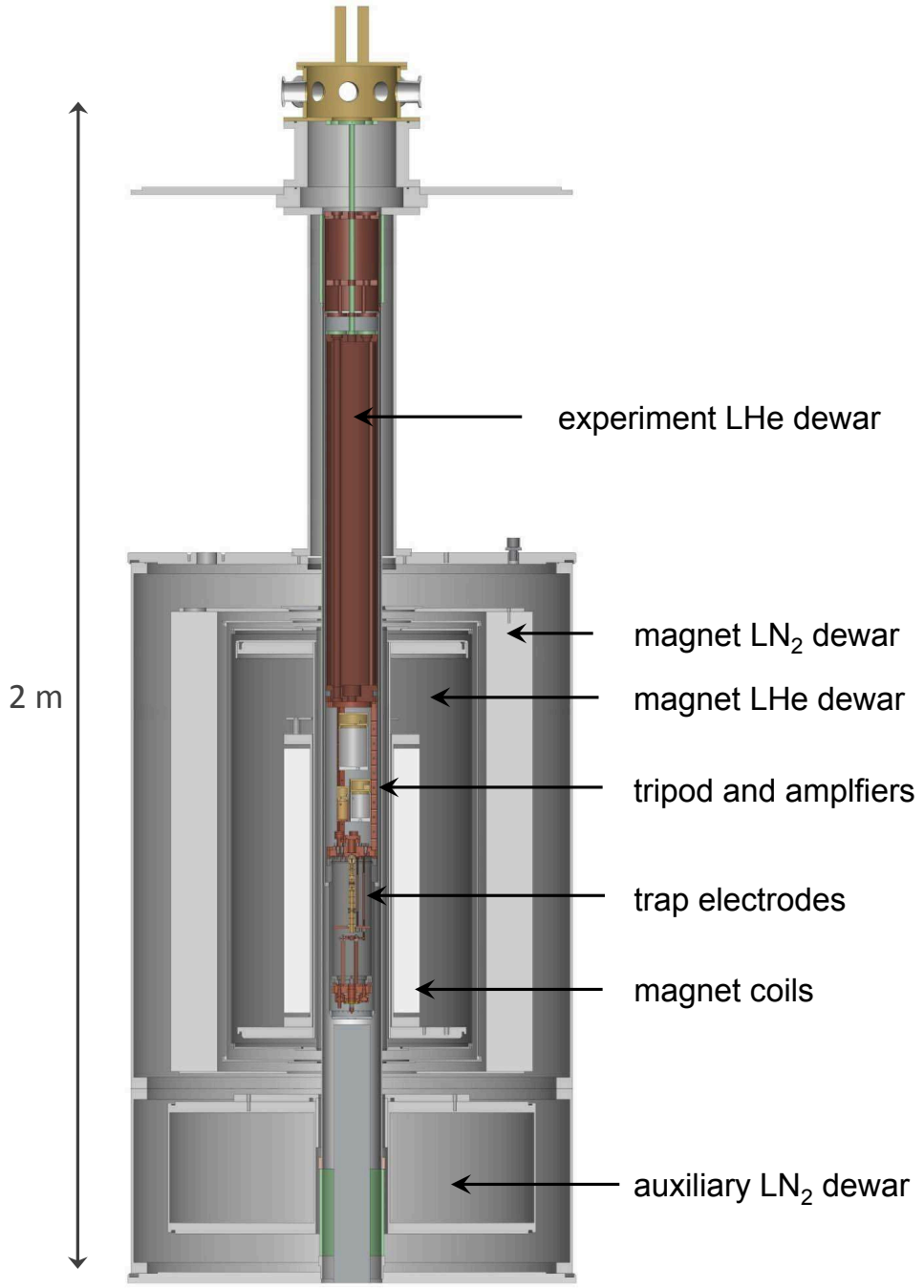

Figure 2.3: The experiment with the magnet, trap electrodes, and cryogen dewars.

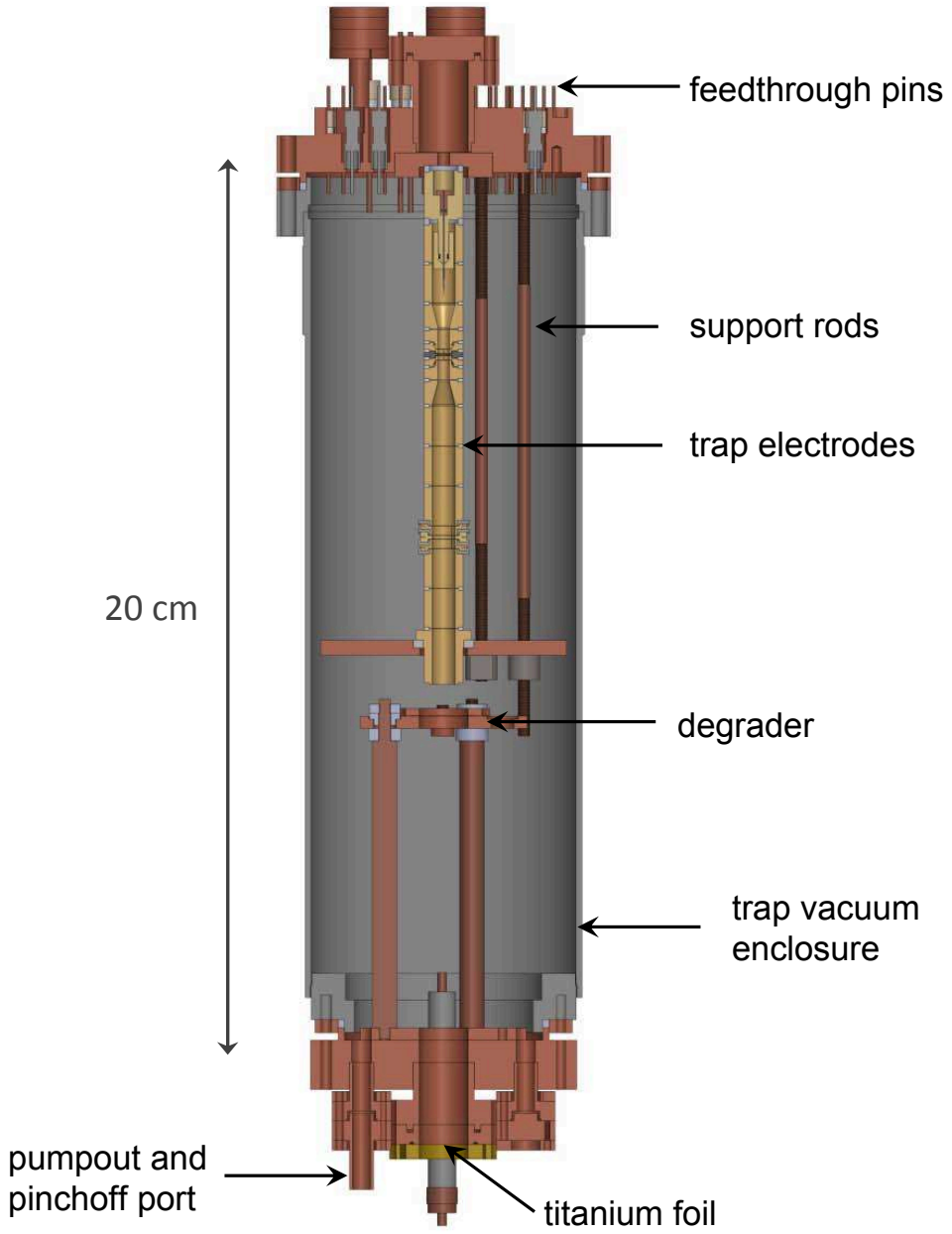

Figure 2.4: The trap vacuum enclosure, electrical feedthrough pins and electrodes.

shift from a spin flip, voltage stability of approximately 0.1μV over a time period of 30 seconds is required. To reduce short term instability and improve filtering, the trap voltages are established by cryogenic capacitors, typically 5 to 10 μF in size for the most sensitive lines. The time constant on this filter is 5 to10 seconds given the 1 MΩ biasing resistor. For the most precise axial frequency measurements, a 100 MΩ resistor is used for a time constant of over 15 minutes. Longer term stability and tunability is established by a Fluke 5440 series precision voltage calibrator.

In addition to DC filtering, the RF lines must also be filtered. As will be discussed in more detail in Sec. 4.2, noise driving the cyclotron motion in the analysis trap can prevent the magnetic moment measurement. This requires careful filtering of Johnson noise as well as other RF noise that can be picked up by the drive lines. The complete schematic for the trap wiring is shown in Fig. 2.5. The wiring schematics for the analysis and precision traps are shown in Fig. 2.6 and Fig. 2.7.

2.2 Magnetic Moment Measurement Principle

In a Penning trap, the magnetic moment is determined by a ratio of the spin and cyclotron frequencies. Essentially, the spin frequency measures the size of the magnetic moment through the $\boldsymbol{\mu} \cdot \mathbf{B}$ interaction, while the cyclotron frequency measures the magnetic field. The magnetic moment, given by $g/2$, can now be expressed in terms of the spin and cyclotron frequencies,

$$\frac{g}{2} = \frac{\nu_s}{\nu_c} \,. \tag{2.18}$$

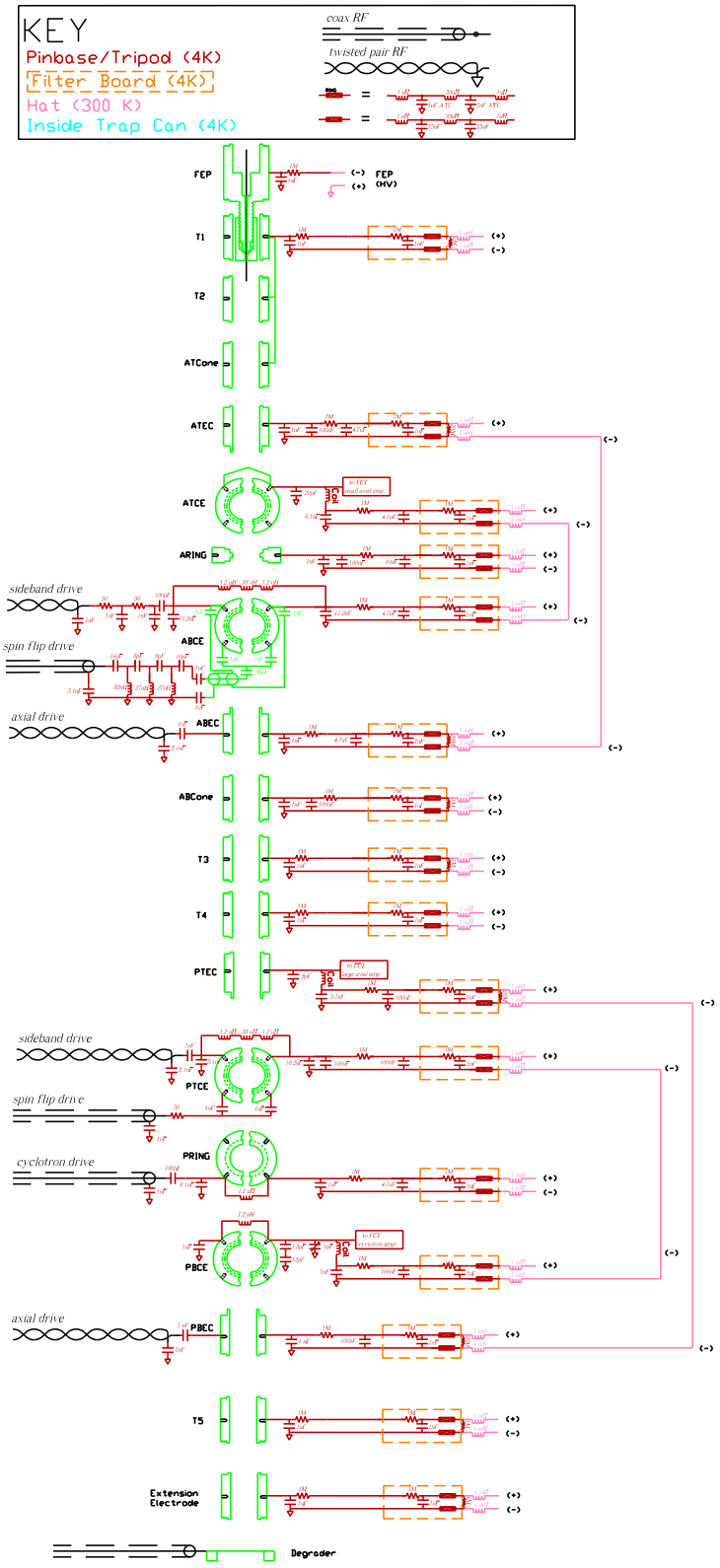

Figure 2.5: The DC and RF wiring schematic.

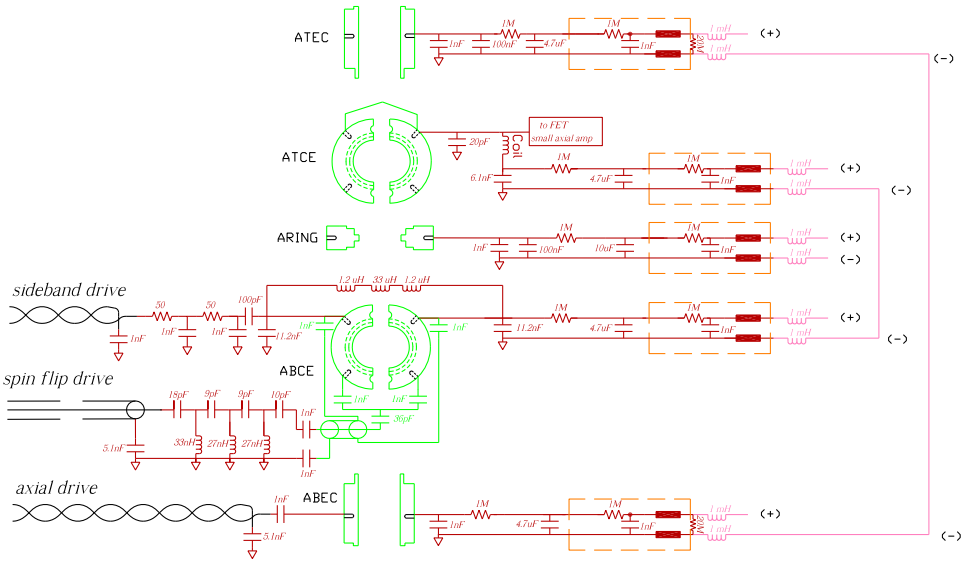

Figure 2.6: The DC and RF wiring schematic for the analysis trap.

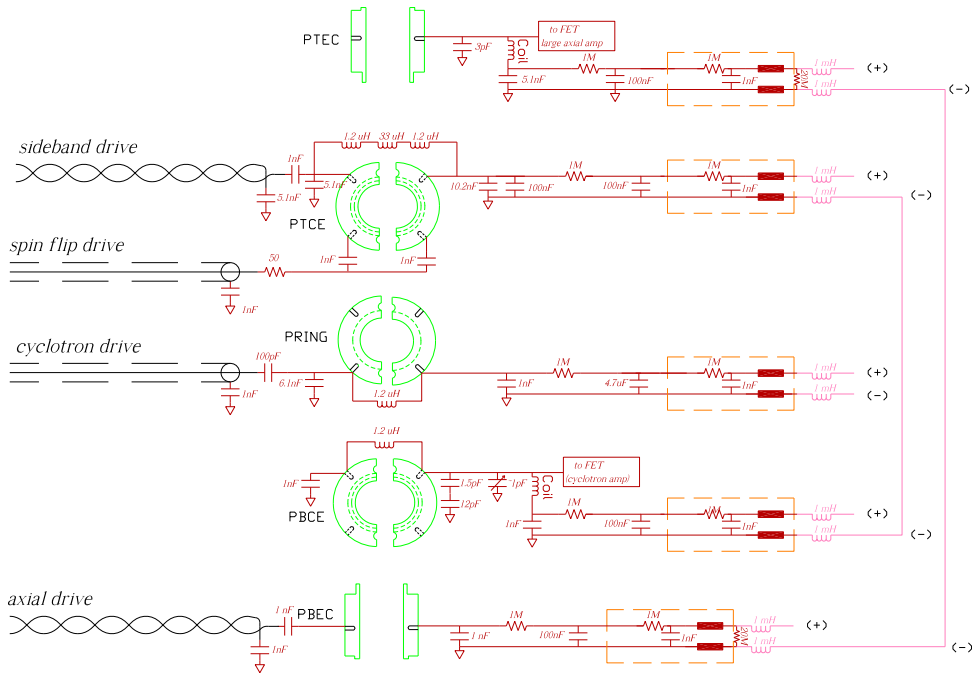

Figure 2.7: The DC and RF wiring schematic for the precision trap.

The elegance of this expression is striking. Much progress has been made in the field of precise time and frequency measurements. Employing a ratio of frequencies takes advantage of this body of work as well as eliminates important systematic effects by using the particle as its own co-magnetometer.

2.3 Magnetic Gradient

To measure the cyclotron and spin frequencies, the magnetic moments are coupled to the axial motion for a non-destructive measurement of the states. This coupling is accomplished by a magnetic gradient given by

$$\Delta\mathbf{B} = B_2[(z^2 - \rho^2/2)\hat{B} - (\hat{B}\cdot\mathbf{z})\rho\,]. \tag{2.19}$$

We typically assume the particle is at the center of the trap, taking $\rho = 0$, simplifying this equation to, $\Delta\mathbf{B} = B_2 z^2 \hat{B}$. This gradient is generated by the iron ring electrode in the analysis trap. In the large background field from the solenoid, the iron saturates and produces a magnetic field determined by the geometry of the electrode. Previous work has gone through a careful analysis and explanation of the relevant magnetic gradient calculations [40, 37].

2.3.1 Axial Frequency in a Magnetic Gradient

The magnetic gradient z^2 scaling couples the magnetic moments of the particle to the axial frequency. This is accomplished by the interaction between the magnetic moments of the particle and the gradient, giving $\Delta H \sim \mu z^2$. As a result, a change

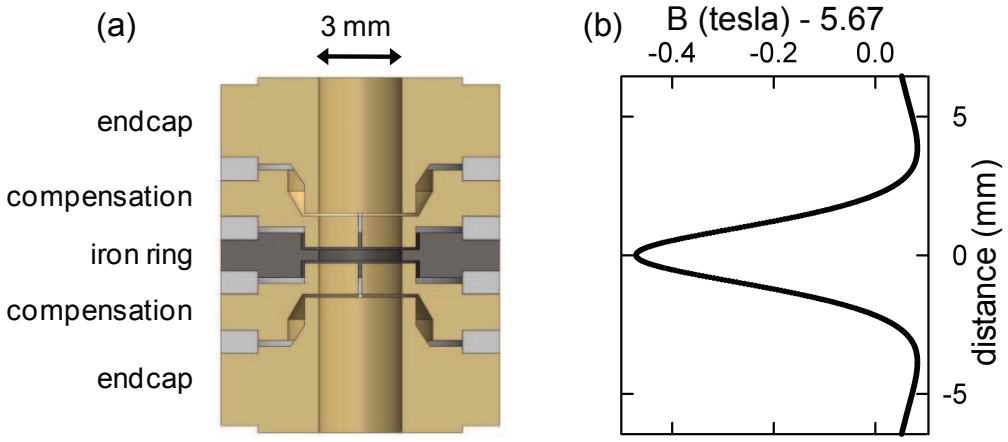

Figure 2.8: (a) The analysis trap where the ring electrode is made from high purity iron. (b) The magnetic field caused by the iron ring in the background magnetic field from the solenoid.

in the magnetic moment of the particle changes the axial frequency. There are three magnetic moments of the particle. The first is due to the spin of the particle, as a result, a spin flip changes the axial frequency. The two other moments are associated with the effective current established by the particle as it undergoes cyclotron and magnetron motion. Accounting for the different sizes of these magnetic moments allows for an expression for the axial frequency shift for changes in the spin, cyclotron and magnetron states, respectively m_s, n and ℓ,

$$\Delta\nu_z \propto \left[\frac{gm_s}{2} + \left(n + \frac{1}{2}\right) + \frac{\nu_-}{\nu_+}\left(\ell + \frac{1}{2}\right)\right] . \tag{2.20}$$

The frequency shifts from a spin flip, a cyclotron jump and magnetron state change are given by approximately 130 mHz, 50 mHz and 3 μHz respectively for a calculated bottle gradient of 290 000 T/m^2 and an axial frequency of 920 kHz.

While necessary for the measurement, the large magnetic gradient also introduces

some experimental challenges. The first issue with the magnetic gradient is that cyclotron state changes by even 3 quanta, cause an axial frequency shift larger than that of a spin transition. For a 4 K particle, the cyclotron state of roughly 1000, this sets a strict requirement on the stability of this state. Johnson noise, damping resistance or anomalous heating seen in the ion trapping community are candidates for driving cyclotron transitions [43]. The second issue with the magnetic gradient is that it substantially broadens the spin and cyclotron lines, which decreases the precision of the magnetic moment measurement. This effect is discussed further in Chapter 5.

To obtain the eventual precision at the ppb level, two traps need to be used in the experiment. The analysis trap is needed to read-out the spin state of the particle, while a precision trap is needed for a low gradient trap to drive the spin flips for the spin frequency measurement used to determine the g-value. This type of measurement scheme was first implemented for bound electron g-value measurements [44, 45, 46]. Using two traps introduces the experimental challenge of transferring a single proton over lengths of approximately 2 inches between the traps.

2.3.2 Residual Gradient in the Precision Trap

The large magnetic gradient in the analysis trap creates a residual magnetic gradient in the precision trap. This must be considered when designing the trap for the ppb measurement. The current electrode stack, shown in Fig. 2.9, uses a single iron ring in the analysis trap. This allows less restriction when loading antiprotons in the precision trap. In the past, a second iron ring was positioned on the other side of the

precision trap to cancel the odd terms of the magnetic gradient. The cost of this is a factor of two in the even terms of the gradient.

The residual magnetic gradient from the iron ring in the precision trap can be quantified using the expansion

$$B_{tot} = B_0 + zB_1 + z^2B_2 + ... \tag{2.21}$$

These components can be calculated using the formalism in references [40, 37]. For the current experimental parameters, given by the iron ring dimensions and the spacing between the iron ring and the precision trap, the components are [40]

$$B_0 = 0.0003\ T\ , \tag{2.22}$$

$$B_1 = 0.02\ T/m\ , \tag{2.23}$$

$$B_2 = 0.8\ T/m^2\ . \tag{2.24}$$

These must be compared to the values from the macor spacers in the precision trap, which may contribute approximately -8 T/m^2 to the B_2 term, given the magnetization of macor reported in reference [40]. This gradient should be addressed either with an improved design that cancels the macor contributions using a clever design [42, 47], or by using quartz spacers as in the electron experiment [48, 49].

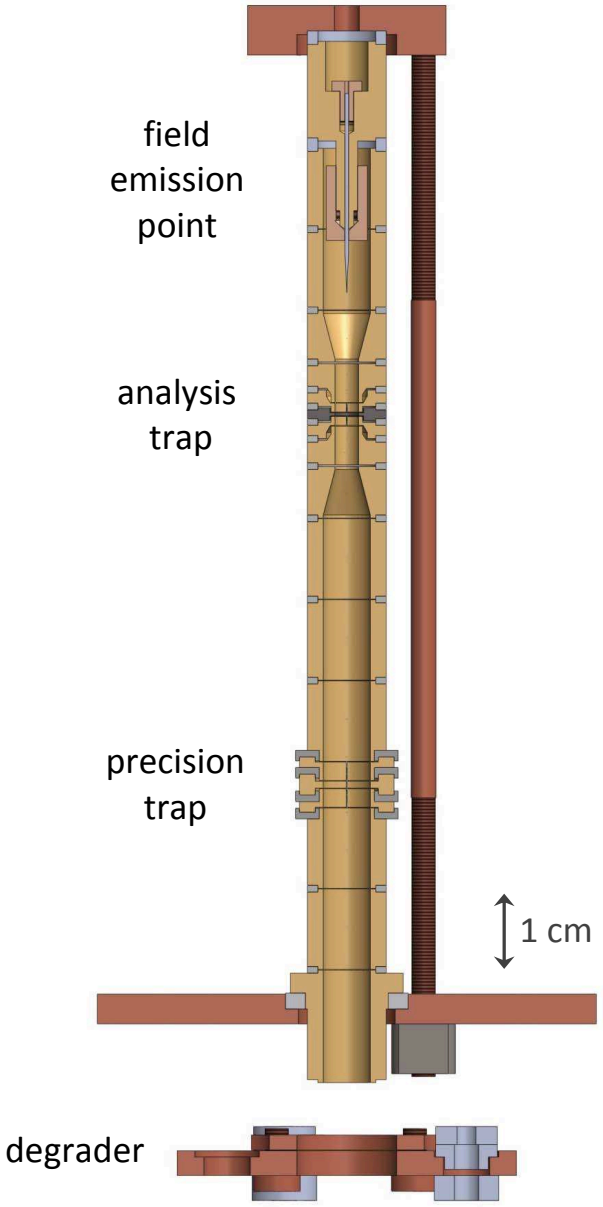

Figure 2.9: The electrode stack. The precision trap is located several cm away from the analysis trap to reduce the residual magnetic gradient from the iron ring.

Chapter 3

Detecting and Driving a Single Particle

The underlying principle of detecting a single ion in a Penning trap is the tiny image currents created by the particle. As the particle undergoes the characteristic motions in the trap, the movement induces a small, but detectable image current in the surrounding electrodes. The amplitude of the oscillation sets the size of the current. As the amplitude increases, the velocity of the particle increases, therefore increasing the current. For the harmonic axial motion, the current is

$$I = \frac{e\kappa}{2z_0}\dot{z} = \frac{e\kappa}{2z_0} A \cdot \omega_z \sin(\omega_z t) \; . \tag{3.1}$$

Where A is the oscillation amplitude, κ is a geometric factor from the trap, z_0 is the spacing between the endcaps and ω_z is the angular axial frequency. For a sense of scale, the size of this current in the analysis trap at 4 K is 25 fA. Given the small size of this signal, much effort is devoted to optimizing the detection electronics.

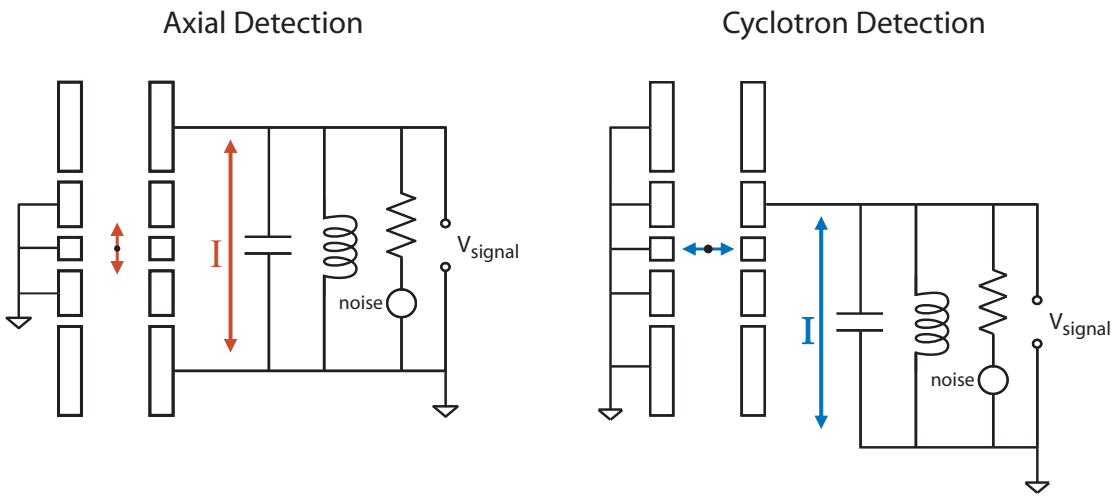

Figure 3.1: The tuned circuits and trap connections for axial and cyclotron detection.

3.1 Amplifiers

The image currents are damped, amplified and detected using tuned circuit amplifiers connected to the trap with the appropriate symmetry. The tuned circuits are high quality LC circuits. The unavoidable losses due to imperfect inductors and capacitors leads to a finite quality factor, Q, and an effective resistance on resonance given by

$$Q = \frac{\Delta\omega_{3dB}}{\omega}\,, \tag{3.2}$$

$$R_{eff} = \frac{Q}{\omega C} = Q\omega L\,. \tag{3.3}$$

Where ω is the resonant frequency, L is the inductance and C is the capacitance. The LC circuit is composed of an external inductor added in parallel to the unavoidable capacitance that comes largely from the trap electrodes themselves. Other contributions to the capacitance are the distributed capacitance in the inductor as well as the

connections to the electrode such as the feedthrough pin.

To detect the cyclotron motion, an electrode must be split radially with the tuned circuit connected across the two halves. This establishes a resistance across the electrode at the cyclotron frequency, providing a damping mechanism for the image current. As the current passes through the resistor, a voltage is generated and then amplified by an HEMT FET (Fujitsu FHX13LG high electron mobility transistor), matched to 50 Ohms, and further amplified at room temperature.

3.1.1 Damping and the Equivalent Circuit

The interaction between the particle and the tuned circuit introduces a damping term in the equation of motion for the charged particle. For the axial motion, the result is a damped harmonic oscillator of the form

$$\ddot{z} + \gamma_z \dot{z} + \omega_z(A)^2 z = 0 \, . \tag{3.4}$$

A is the amplitude of the axial oscillation that can shift the oscillation frequency from the trap anharmonicity introduced in Chapter 2, and γ_z is the damping width of the particle. The damping width, $\gamma_z = \left(\frac{e\kappa}{2z_0}\right)^2 \frac{R}{m}$, is set by the size of the resistor used to damp the motion, the size of the trap and the geometry used to pick-up the image current, as well as the charge and mass of the particle.

From the damped harmonic oscillator equation, it is possible to express the interaction between the particle and damping resistor as a lumped circuit element system [50, 51]. In the resulting circuit, the particle is modeled as a series LC circuit. This equivalence can be seen by using the current from Eq. 3.1, expressing the detected signal as $V_{signal} = IR$, and matching terms with the differential equation for

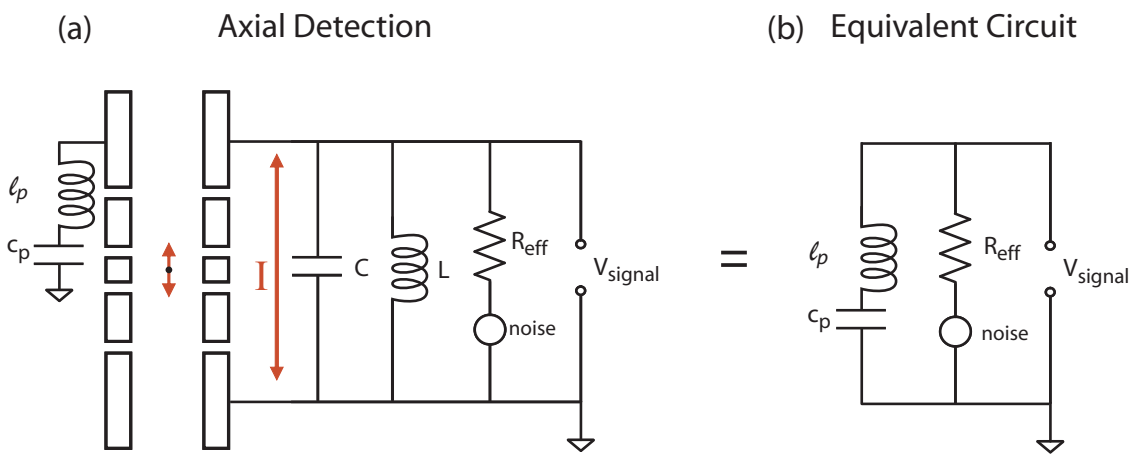

Figure 3.2: The tuned circuit and equivalent lumped circuit for the axial motion.

current in a series LC circuit

$$\ell_p \frac{dI}{dt} + \frac{1}{c_p} \int I \, \mathrm{d}t = V_{signal} \; . \tag{3.5}$$

Typical values for an axial frequency of 1 MHz are

$$\ell_p = m_p \left(\frac{2z_0}{e\kappa} \right)^2 \approx 3 \times 10^6 \text{ H} \tag{3.6}$$

$$c_p = \frac{1}{\ell_p \omega_z^2} \approx 9 \times 10^{-21} \text{ F} \; . \tag{3.7}$$

This description is helpful for understanding the axial response from a particle in the absence of an externally applied drive. In this case, the Johnson noise from the tuned circuit is still present and the series LC resonance of the particle centered at the axial frequency shorts this noise to ground. The result is a dip in the noise resonance. This will be discussed further in Section 3.2.2 with examples from a single proton.

3.1.2 Noise Resonances

The signature of the tuned circuit is the so-called noise resonance. The effective resistance of the tuned circuit creates a Lorentzian line shape in noise power given by the Johnson noise of the circuit, $V_n = \sqrt{4k_B T R_{eff} B}$. Here, T is the temperature, R_{eff} is the effective resistance and B is the bandwidth. Typical noise resonances for the amplifiers are shown is Fig. 3.4.

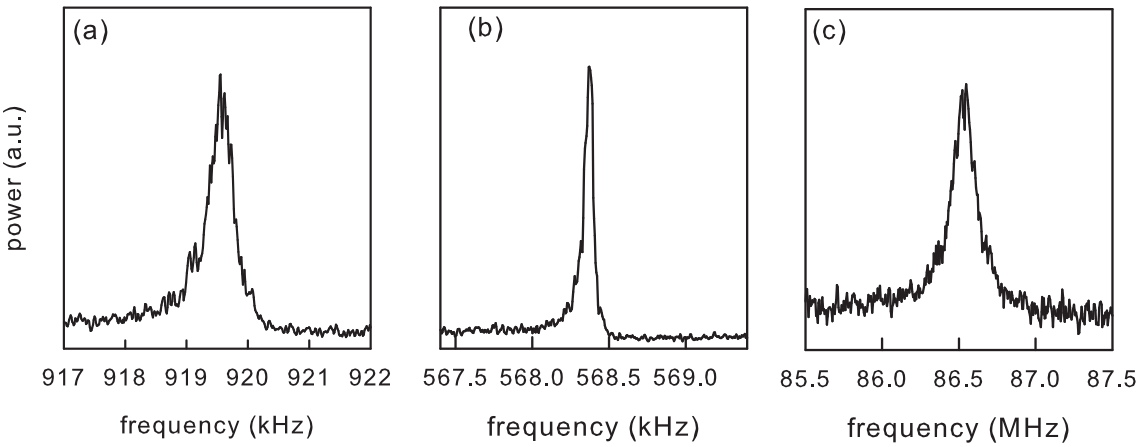

Figure 3.3: The tuned circuit noise resonances for the (a) small axial (b) large axial and (c) cyclotron amplifiers.

The second stage amplifier is a bit different from the first stage. Instead of tuning out the trap capacitance with an inductor, both the input and output of the second stage are matched to 50 Ohm. This allows for matching to the first stage drain as well as the room temperature outputs. As a result of the 50 Ohm input matching, the second stage amplifier is a broader band amplifier. This eliminates concerns about detuning between the first and second stage resonances. It should be noted, that positive feedback has been used in a second stage amplifier design and does provide

increased signal-to-noise, at the possible cost of amplifier tuning and stability [52]. The second stage amplifier is used to further increase the signal-to-noise of the signal from the trap by elevating the signal level further above the noise level of room temperature detection. Furthermore, as will be discussed further in Sec. 3.2.3, it allows for a lower axial temperature of the particle.

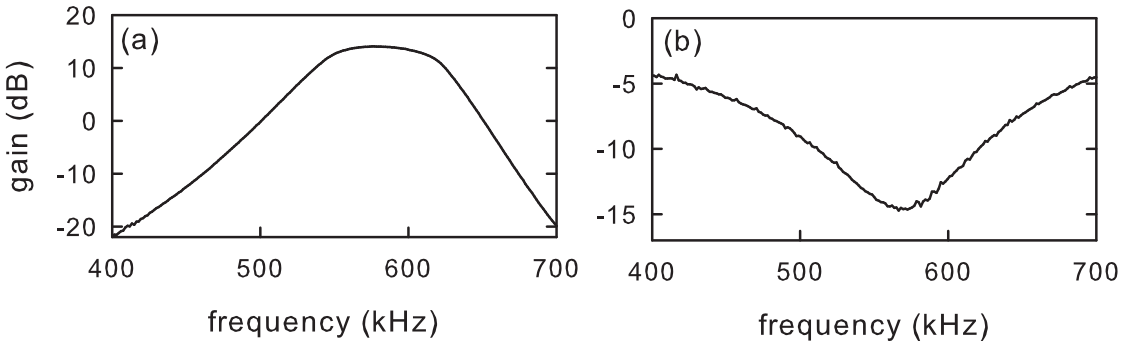

Figure 3.4: (a) The gain through the second stage amplifier. (b) The reflection from the pi-net.

3.1.3 Signal-to-Noise

The signal-to-noise of the detection system is quite important because it sets the averaging time needed to see a signal. Furthermore, for resolving a spin flip or cyclotron jump, the signal-to-noise determines to the averaging time needed to resolve the small axial frequency shifts. The signal is given by the voltage drop across the tuned circuit from the image current. The noise comes from the Johnson noise of the effective resistance of the tuned circuit. The ratio of these two voltages gives the

signal-to-noise,

$$S/N = \frac{V_{signal}}{V_{noise}} = \frac{(e\kappa)/(2z_0)A\omega_z R}{\sqrt{4k_B TRB}} \,. \tag{3.8}$$

For reference, the signal-to-noise for a proton in thermal equilibrium with a tuned circuit of 10 MΩ at 1 MHz and 4 K is approximately 1. This motivates using of a driven, narrowband detection technique, such as the self-excited oscillator discussed further in Section 3.2.3 [53, 54, 52].

3.1.4 Detection Circuits

The voltage created by the image current through the tuned circuit must be coupled out of the cryogenic part of the experiment. This causes two main issues, the first is that the tuned circuits are high impedance, coupling this to a 50 Ohm coax would substantially load the tuned circuit, compromising the signal-to-noise. The second issue is that room temperature Johnson noise decreases the signal-to-noise, so it is important to have the highest possible signal level from the tuned circuit. To address these issues, a HEMT FET is used to facilitate impedance matching, providing roughly 20 dB of gain.

Care must be taken when designing the amplifier circuit board. Given the high effective resistance of the tuned circuit, it is possible to create comparable loss resistances. Both the input impedance of the FET and gate bias resistors create effective resistances in parallel with the tuned circuit that decrease the Q. These losses can be minimized by proper matching to 50 Ohms using the pi-net circuit on the drain side of the FET. On the gate side, large bias resistors must be used. This is especially true for the large axial tuned circuit that has effective resistances approaching 100

MΩ.

The impact of the FET on the tuned circuit is a bit more involved to calculate, but is important for the complete circuit analysis [37, 52]. Matching to 50 Ohms and different loads from the pi-net, can introduce either positive of negative feedback on the front end of the circuit. As a result, the amp front end resonance is typically tuned slightly above the center frequency of the pi-net matching circuit. More details on this can be found in two previous theses [52, 37].

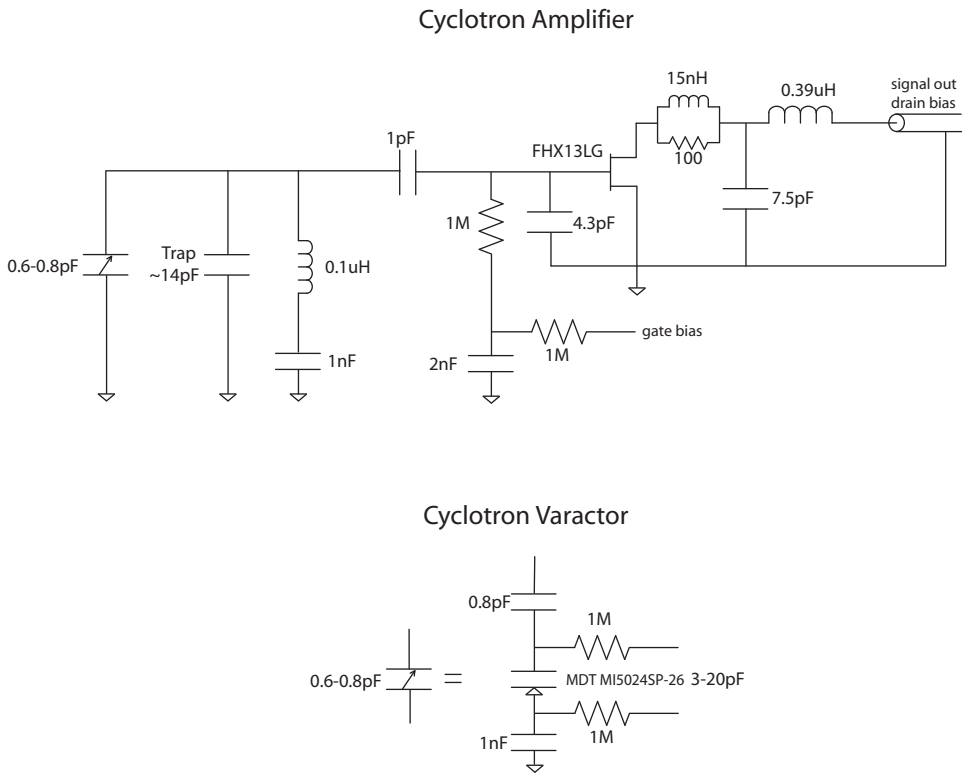

Figure 3.5: The circuit for the cyclotron amplifier.

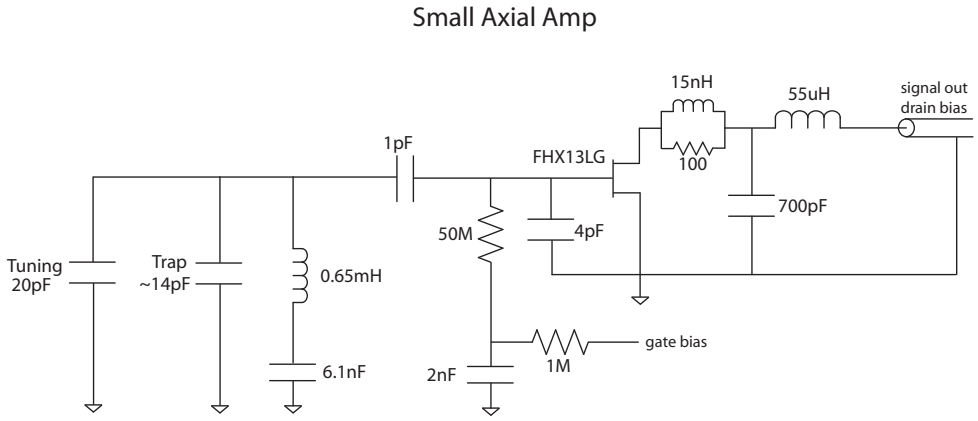

Figure 3.6: The circuit for the small axial amplifier.

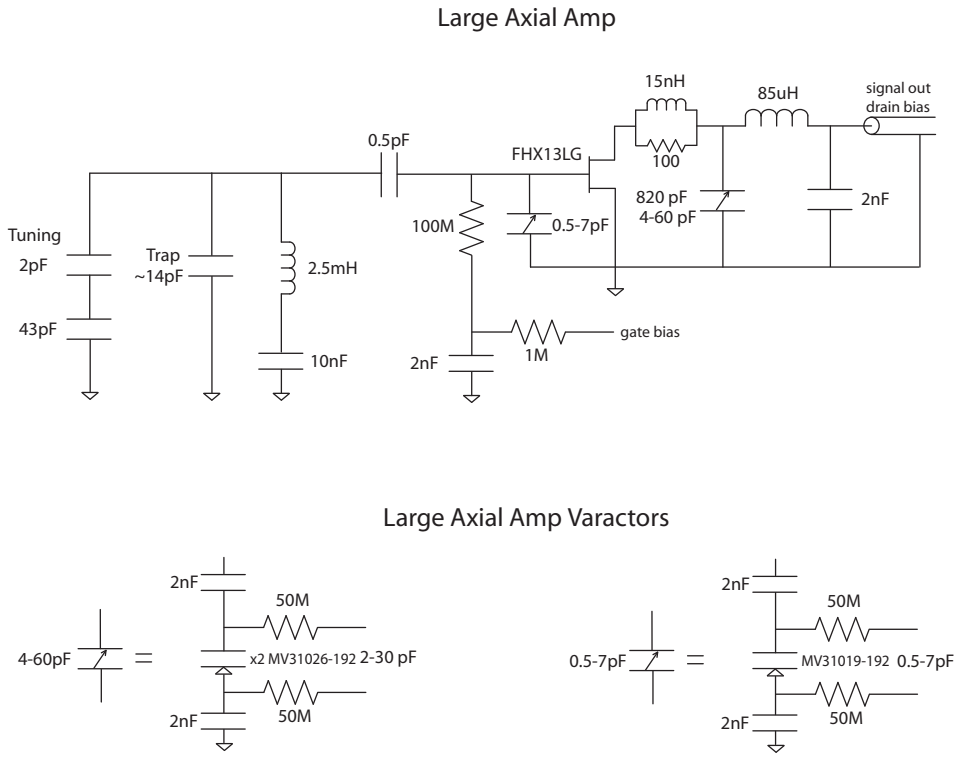

Figure 3.7: The circuit for the large axial amplifier.

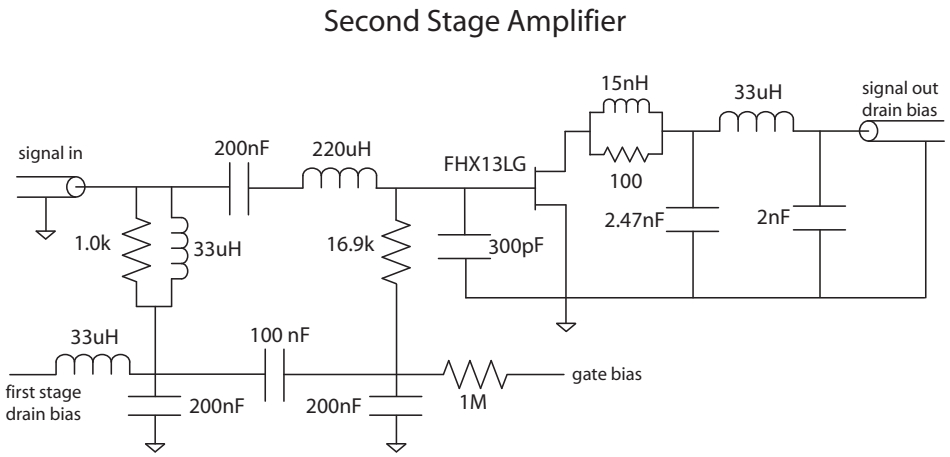

Figure 3.8: The circuit for the second stage amplifier.

3.1.5 Varactors

The circuits for the cyclotron and large axial amps have voltage-tunable capacitors, known as varactors. Using a tuning voltage, these varactors can change either the tuned circuit resonant frequency, the pi-net tuning, or capacitive divider at the input to the FET. For the cyclotron amplifier, the varactor is used to tune the tuned circuit frequency to the cyclotron frequency established by the magnetic field. The need for this tuning is seen by the half-width of the cyclotron amp which is roughly 200 kHz. This frequency span corresponds to a change of roughly 0.1 pF in capacitance of the tuned circuit. Given the fact that the amplifier's effective resistance drops as the amp is detuned from the particle, to maintain the highest damping and signal-to-noise possible, the amplifier must be tuned to better than 0.1 pF.

The front end tuning of the cyclotron amp is useful because the cyclotron frequency is set by the magnetic field. Given the stability requirements of the magnetic field, as well as the relative time and complications of ramping the field, it is easier to tune the

cyclotron amp to the proper frequency than tune the magnet to the cyclotron amp. As shown in Fig. 3.9, the cyclotron varactor provides a tuning range of approximately 200 kHz at 4 K. While the varactor is useful, the tuning range is limited and the varactor may be limiting the amplifier Q in the magnetic field. It may be worthwhile attempting to tune the cyclotron amp only with fixed capacitors to test this.

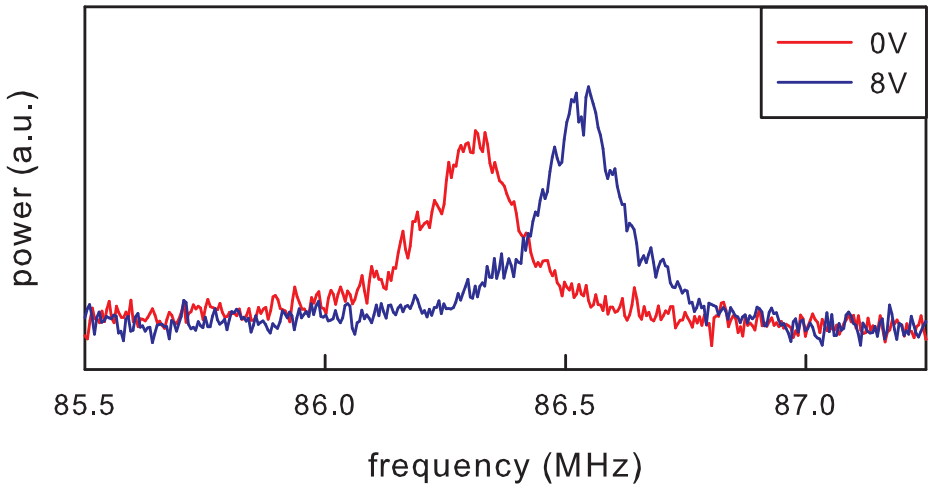

Figure 3.9: Using a varactor to change the frequency of the cyclotron amplifier. The tuning range is approximately 200 kHz.

The axial front end tuning is less of an issue because applied voltages set the axial frequency. However, with the high Q large axial amp, it is important to tune the pi-net to optimize the front end loading. To decrease loading, it is necessary to have the amplifier close to the minimum in the pi-net, but slightly above to avoid positive feedback. However, the effect of positive feedback has not been studied in detail, and more information on this can be quickly learned with a tunable pi-net. Figure 3.10 shows the amplifier noise resonance when the pi-net is tuned lower and

higher in frequency. The Q and effective resistance in the non-regenerating case is 9000 and 80 MOhm. For the case when the pi-net frequency is higher, the respective values are 24000 and 210 MOhm. The corresponding single proton dips, taken at the

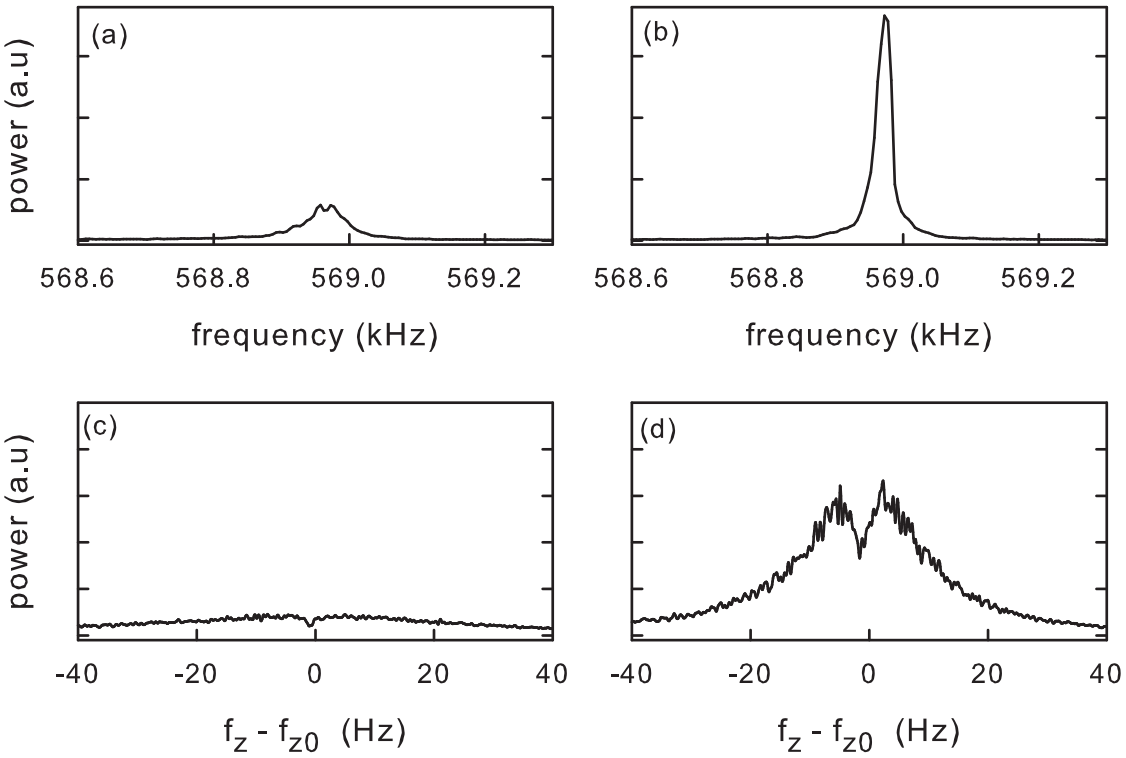

Figure 3.10: The large axial noise resonance (a, b) and corresponding proton dip (c, d) at different pi-net tuning voltages. On the left, a voltage of -10V tunes the pi-net below the front end resonance. On the right, 0V tunes the pi-net above the front end resonance and positive feedback increases the effective resistance, clear from the wider dip.

same settings, show a clear increase of the damping width that is expected from the higher Q. If the Q is increasing because of positive feedback, it would be interesting to verify that the temperature is also increasing. As discussed in Chapter 5, the axial temperature can be measured using sideband cooling in the magnetic bottle field in

the analysis trap.

It may also be useful to optimize the capacitive divider input to the FET to optimize signal-to-noise. Using the varactor, it is possible to change the tap ratio to see what the optimum tuning ratio is. Ideally, we would like to get the largest signal from the front end without loading down the tuned circuit with the parallel loads from the FET or gate bias resistance. Figure 3.11 shows the noise resonance and dip as a function of varactor tuning voltage. The Q starts to increase slightly for the

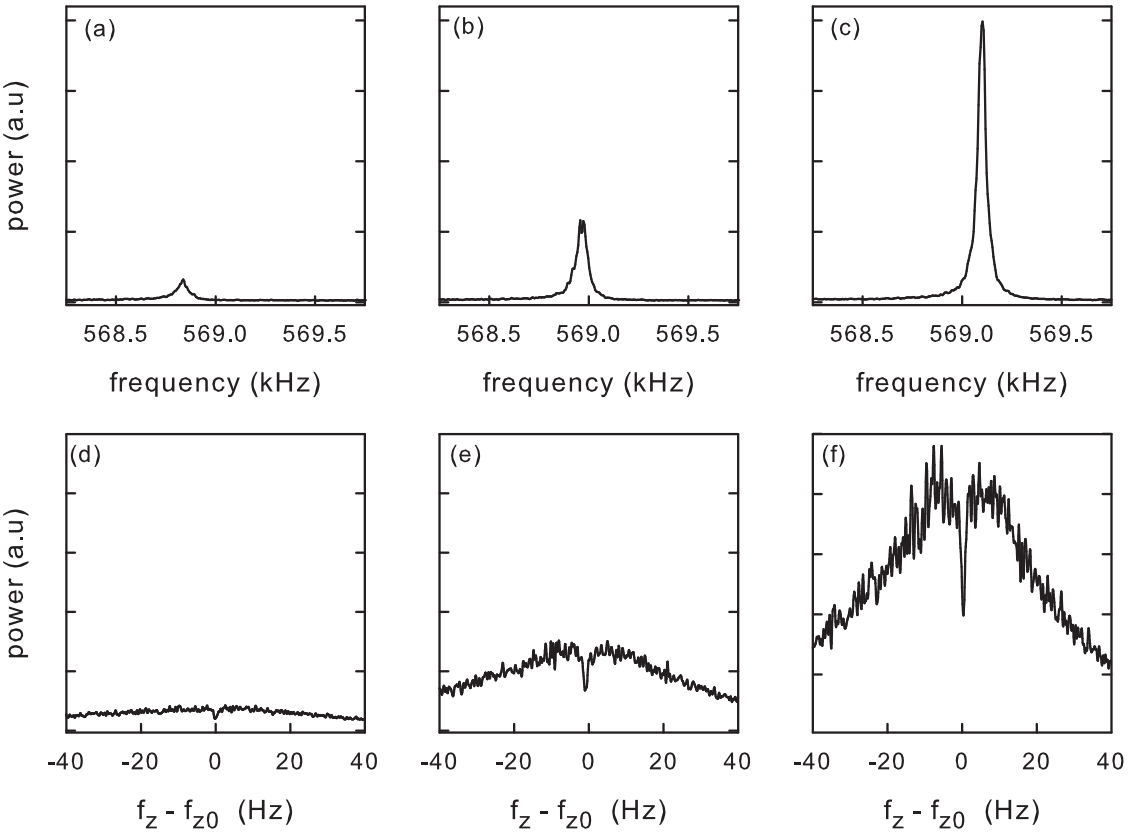

Figure 3.11: The large axial noise resonance (a, b, c) and corresponding proton dip (d, e, f) at different tuning voltages, 0V, 1.5V and 4V respectively. Increasing the voltage deceases C2, as a result there is more signal from the particle and noise resonance.

higher voltage, indicating possible feedback to the front end or decreased loss in the varactor. The effect of changing the capacitive divider has not be studied in detail yet, mainly due to the fact that the large axial amp is currently attached to the precision trap where signal-to-noise is not as important as in the analysis trap. It would be interesting to use this amp in the analysis trap for the increased signal-to-noise as well as to further optimize the amplifier circuit.

3.2 Axial Detection

The axial motion can be detected using a variety of methods. Given that the axial frequency is used to measure the spin and cyclotron frequencies needed for the magnetic moment measurement, much effort has been devoted to optimizing the axial frequency detection.

3.2.1 Axial Drives

The first technique for detecting the axial motion uses an axial drive. It is generally employed for finding the axial signal after a cooldown or transfer and initially reducing the trap anharmonicity. For this type of axial detection, an oscillating drive is applied to the trap at a fixed frequency, ω_d, and the driven axial response from the particle is measured. The resulting equation of motion is that of a damped, driven harmonic oscillator,

$$\ddot{z} + \gamma_z \dot{z} + \omega_z^2(A) z = F_d(t)/m. \tag{3.9}$$

While this is qualitatively the correct picture, in practice, applying a drive at $\omega_d = \omega_z$ would cause direct feedthrough of the drive to the amplifier, which would overwhelm the small signal from the particle. To avoid this, we typically apply two axial drives, one at an intermediate frequency, $f_I \approx 455$ kHz, and the other at $f_z - f_I$. This intermediate frequency is chosen to be that of a commercially available crystal filter.

Initially finding the axial response can require a substantial voltage adjustment, especially when characterizing a trap for the first time (see Sec. 3.2.4 for details on non-reversing voltages). In practice, the small changes from thermal cycling lead to changes comparable to machining tolerances at the parts per thousand level. In this case, the first method of choice is a driven axial scan with a cloud of ions. For this scan, the drive frequency is fixed on the center frequency of the amplifier and the ring voltage is stepped across a range of up to 0.6 V around a ring voltage of ∼1.5 V which should contain the axial response. Using fairly strong axial drives (for example -13 dBm at the hat), the signal from a cloud of ions can be seen in scan covering such a large voltage range. Figure 3.12(a) shows an axial response for the first antiproton axial signal in our trap.

After cloud resonances are seen, the trap depth is lowered to spill out all but one of the particles. This process is generally done by monitoring the cyclotron signals as discussed in detail in Section 3.3. After obtaining just one particle, the voltage sweep axial scan can be repeated to more precisely measure the voltage and tune the anharmonicity. The specific tuning procedure to reduce the trap anharmonicity is discussed in detail in previous work [37]. The essential feature of the process is that driven axial scans are repeated with different settings of the compensation electrode

voltage. Given the fact that a harmonic oscillator frequency is amplitude independent for a purely harmonic potential, the ratio is changed to minimize the width of the response. Sweeping the voltage both up and down is required to tune the anharmonic response.

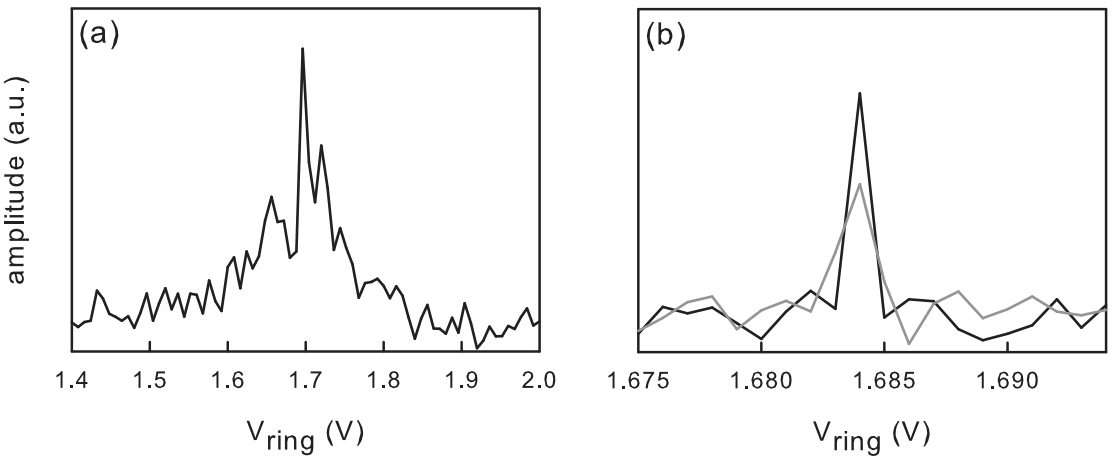

Figure 3.12: (a) The driven axial response for a cloud of antiproton measured using a fixed frequency axial drive and changing the ring voltage. (b) The same for a single antiproton, with a sweep up (black) and a sweep down (gray) in voltage. This response is 1 mV wide corresponding to 200 Hz for an axial frequency of 570 kHz in the precision trap.

The response for a single antiproton is shown using a greatly expanded span in Figure 3.12(b). The black and gray responses are the sweeps up and down in voltage. Figure 3.12(b) shows a response that is roughly 1 mV wide, or approximately 200 Hz. After this, it is possible to use a sweep where the ring voltage is fixed and the drive frequency is changed. Figure 3.13 shows the response for a well tuned frequency sweep with a width in the Hz range.

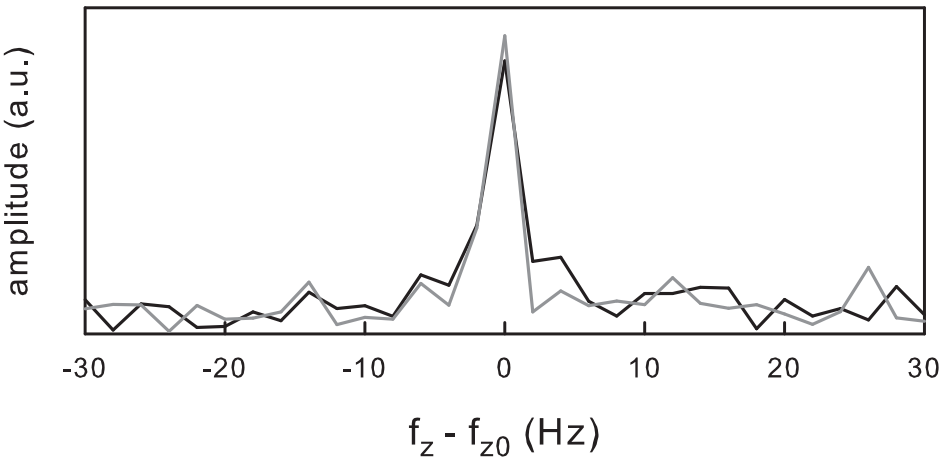

Figure 3.13: A driven axial response using a fixed ring voltage and changing the drive frequency. The response is narrow on the Hz level indicating good anharmonicity tuning. This data is taken in the precision trap with an axial frequency close to 930 kHz.

3.2.2 Dips

When the anharmonicity tuning is at the 200 Hz level or better for a driven response, it should be possible to see a dip, a shorting of the tuned circuit noise by the particle itself. It is essential to have clear signals from dips on the time scale of a minute or less for this to be a time efficient tuning option. The damping width of the particle should be at least $(2\pi) \cdot 1$ Hz for a dip to be clearly visible in approximately one minute. Once a dip is clear, further anharmonicity tuning may be necessary to reduce the width from an anharmonicity limited width to the damping width. The result of first finding the dip signal and improving the anharmonicity tuning is shown in Figure 3.14.

Using dips, the axial frequency can be measured to within about 100 mHz. Typ-

ically this requires an averaging time of about 80 seconds if we view a frequency span of 30 Hz. However, for higher signal-to-noise and hence faster axial frequency measurements, we use the self-excited oscillator (SEO). This is a feedback technique where the signal from the single particle is amplified and fed back to drive the particle to a steady state oscillation amplitude. The feedback is essentially used to cancel the damping from the amp.

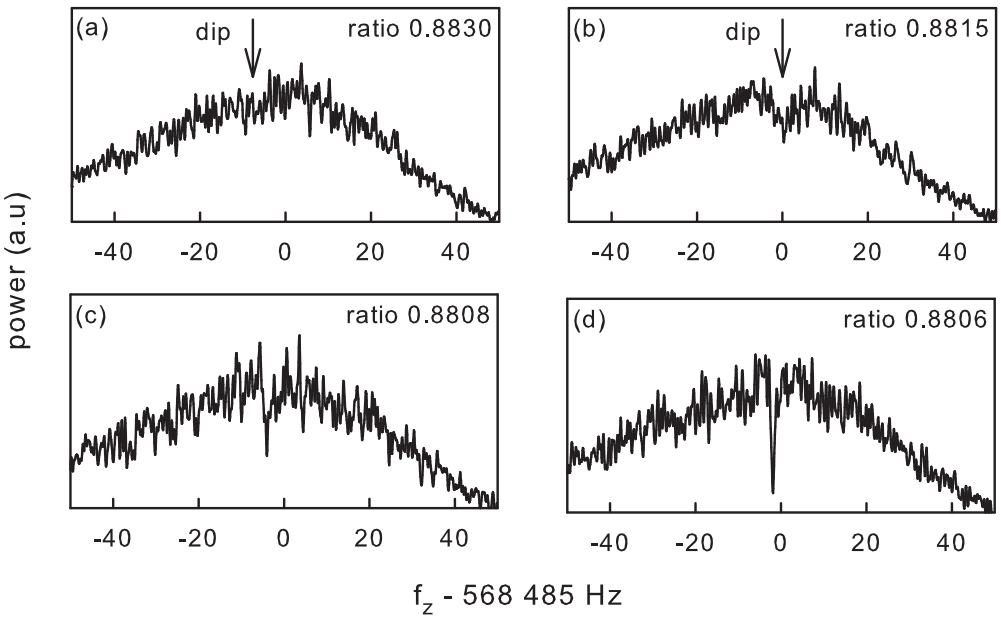

Figure 3.14: The axial frequency dip of a single antiproton as the anharmonicity is tuned by changing the ratio. From left to right, top to bottom, the compensation voltage is changed to decrease the anharmonicity, narrowing the dip width.

Figure 3.15(a) shows the SEO signal with a 16 second averaging time. Compared to the 80 second averaging time for the dip in Fig. 3.15(b), the signal-to-noise is substantially higher. As an added benefit, the width of the SEO is not limited by the damping width, this is because the feedback reduces this width by decreasing the

damping. An ideal undamped harmonic oscillator has a width limited by the Fourier time. In practice, the width is also limited by the instability of the axial frequency as averaging time increases.

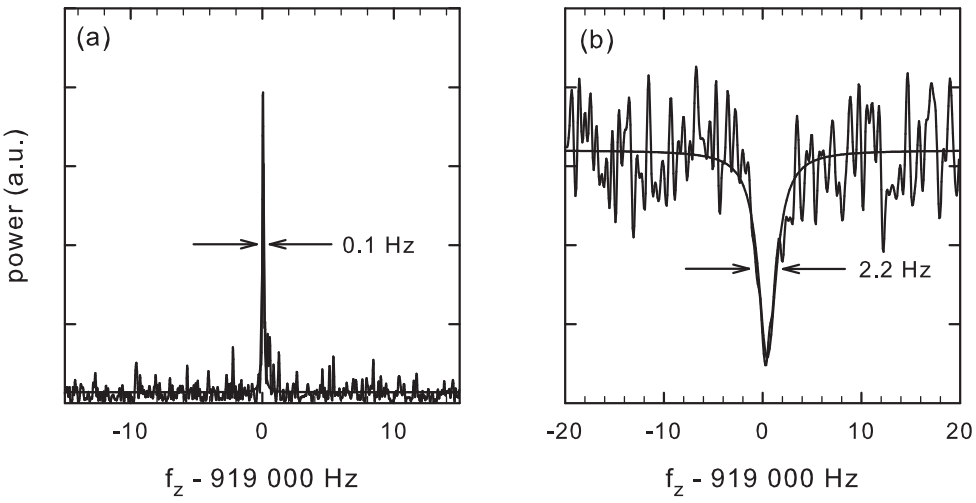

Figure 3.15: (a) The self-excited signal from a single proton averaged 16 seconds. (b) The dip signal averaged for 80 seconds.

3.2.3 Axial Feedback

The principle behind axial feedback is that the signal generated by the image current through the damping resistor is amplified, phase-shifted and sent back in to the experiment to then interact with the particle [55, 54, 4]. The schematic for applying feedback to the axial motion is shown in Fig. 3.16. The drive is given by $F_d(t)/m = G\gamma_z\dot{z}$. Inserting this in the axial equation of motion gives

$$\ddot{z} + (1-G)\gamma_z\dot{z} + \omega_z(A)^2 z = 0\,. \tag{3.10}$$

Using this equation of motion, it is possible to explain both the use of feedback to control the axial temperature as well as establish the self-excited oscillation [55, 54, 4].

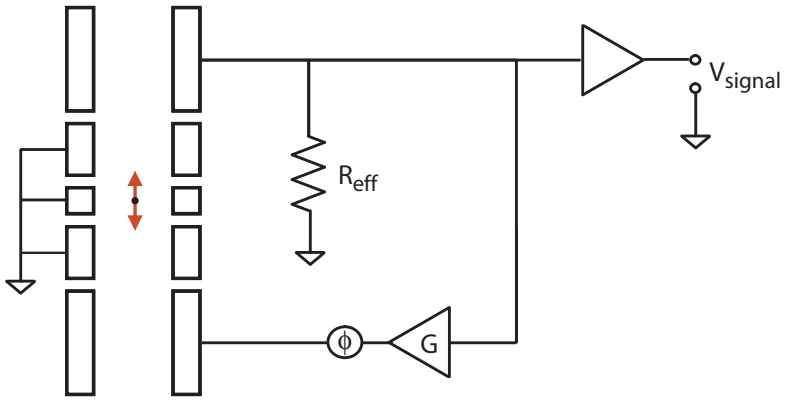

Figure 3.16: The schematic for applying feedback to the particle.

Temperature Control with Feedback

From Eq. 3.10, it is clear that feedback can change the effective damping rate of the particle. We see that for $G > 0$, the feedback effectively reduces the damping, and for $G < 0$, the damping is increased. This feedback consequently changes the effective temperature of the damping resistor [55]. In the noiseless limit, the effective temperature and damping are given by

$$T_{eff} = (1 - G)\, T, \tag{3.11}$$

$$\Gamma_{eff} = (1 - G)\, \Gamma. \tag{3.12}$$

This shows how the temperature can be controlled using feedback strength. Figure 3.17 shows the signal from a proton with feedback heating (a), no feedback (b) and feedback cooling (c). The increased damping width of 7 Hz, is more than a factor

of two greater than the case with no feedback. With feedback cooling, the dip width of 1.5 Hz indicates approximately a factor of two reduction in temperature.

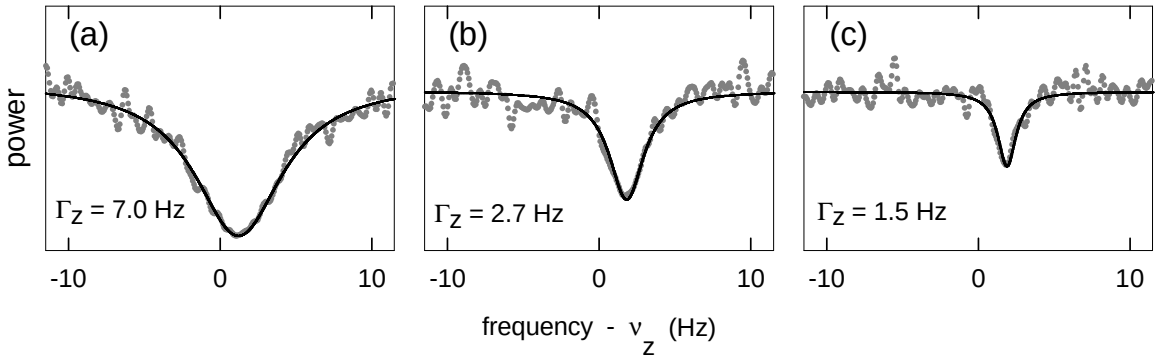

Figure 3.17: The proton dip with (a) feedback heating, (b) no feedback, and (c) feedback cooling. The change in width gives the temperature change, the result is verified using a sideband technique to directly measure the axial temperature (see Sec. 5.3.1).

To test the relationship between temperature and damping width, as well as to measure the absolute temperature, we use SB cooling of the magnetron motion in the magnetic gradient field, discussed further in Sec. 3.5 and Sec. 5.3.1 [4, 37]. Essentially, SB cooling equalizes the magnetron and axial quantum numbers and the magnetron quantum number is then read out by the axial frequency shift in the bottle field (see Sec. 2.3.1 for details on the magnetron state changing the axial frequency). This process is repeated many times and the axial temperature can be extracted from a histogram of the axial frequency shifts. The result is shown in Fig 3.18. The temperature with no feedback applied is 8 K and decreases linearly with feedback strength to a minimum value of 4 K. This minimum temperature is limited by technical noise in the feedback which impedes feedback cooling to lower temperatures [55]. Decreasing this limit can be achieved with improved low temperature amplification.

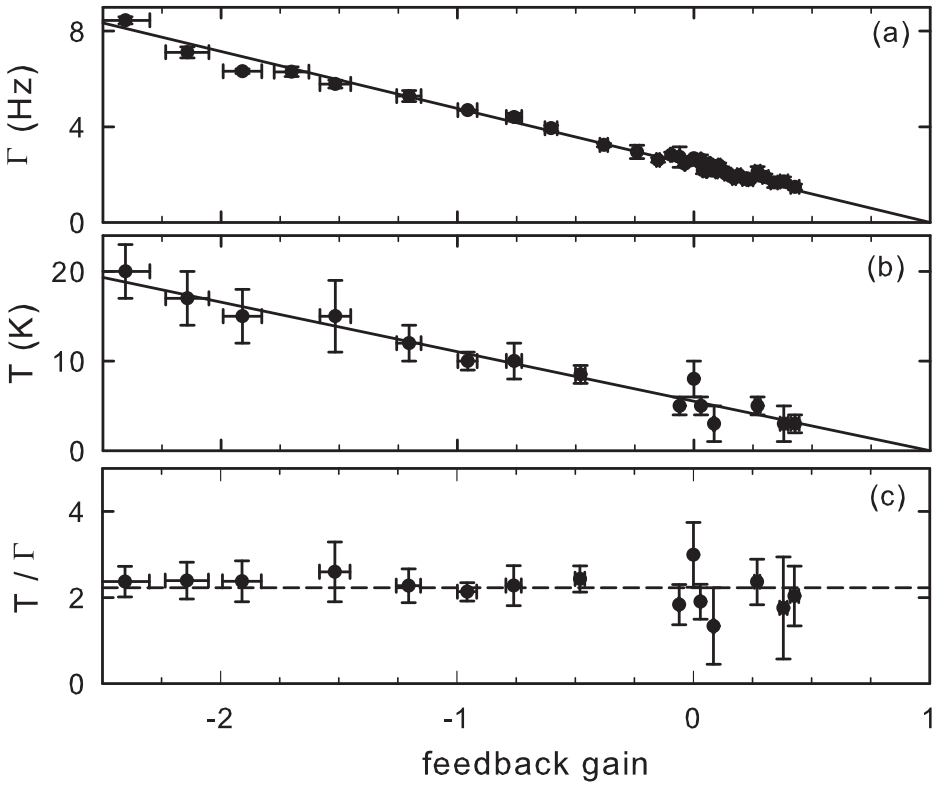

Figure 3.18: The proton dip width and temperature measured as a function of feedback strength. The axial temperature is measured independently using a sideband technique (see Sec. 5.3.1). The ratio of the two is constant, as expected from the fluctuation-dissipation theorem.

Installing a second stage amplifier decreased the technical noise that was limiting the minimum feedback cooling temperature. This allowed for improved feedback cooling and demonstrated dip widths of 0.5 Hz, narrower by a factor of 5 from the damping width with no feedback, corresponding to a temperature in the 1-2 K range. As shown in Fig. 3.19, this is an improvement over the previous feedback scheme using just the first stage amplifier. With only one stage of amplification, signals were not clear below widths of around 1.5 Hz. Decreasing the technical noise should also improve the signal-to-noise in the self-excited oscillator, but this has not yet been studied carefully.

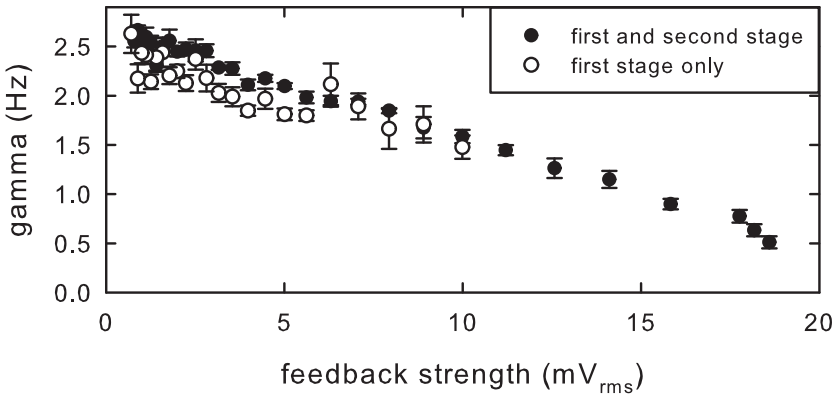

Figure 3.19: The proton dip width as a function of feedback strength with a lower technical noise using the second stage amp. The second stage allows for cooling to an axial temperature lower by a factor of three.

Self-Excited Oscillator

To fully explain the self-excited response, it is necessary to account for the phase dependence of the feedback, which is needed to offset the time delay introduced by the length of the feedback loop [52, 54]. The equation that must be satisfied for

self-excitation is

$$G\cos(\phi) = 1\ . \tag{3.13}$$

In the optimal phase tuning scenario, $\phi = 0$ and $G = 1$. This gives an equation of motion of a simple harmonic oscillator. However, it is important to note that the amplitude of the self-excited oscillator is exponentially sensitive to the feedback strength. That is to say, if a noise fluctuation slightly increases the damping, the oscillation amplitude exponentially damps, and conversely, a noise fluctuation that decreases the damping causes the oscillation amplitude to exponentially increase. To solve this problem, we employ a digital signal processor (DSP) to actively measure the axial amplitude and adjust the feedback strength to maintain a stable axial oscillation amplitude [52, 37].

The DSP is a dedicated device that performs a Fourier transform of the detected signal. It then determines the maximum amplitude in the frequency window and converts this amplitude to a voltage that is then applied to a voltage variable attenuator (VVA). Part of the feedback signal passes through the VVA before entering the experiment. A detailed schematic of the SEO feedback implementation can be found in Fig. 3.20. With the DSP controlled VVA, we establish a lock loop for the axial oscillation amplitude. The degree to which the axial amplitude is constant is important for the axial frequency stability because the trap anharmonicity changes the axial frequency as a function of amplitude.

Using the high signal-to-noise of the SEO, it is possible to further optimize the anharmonicity tuning of the trap. This is essential for improving the stability of the axial frequency. Figure 3.21 shows the Allan deviation of axial frequency data taken

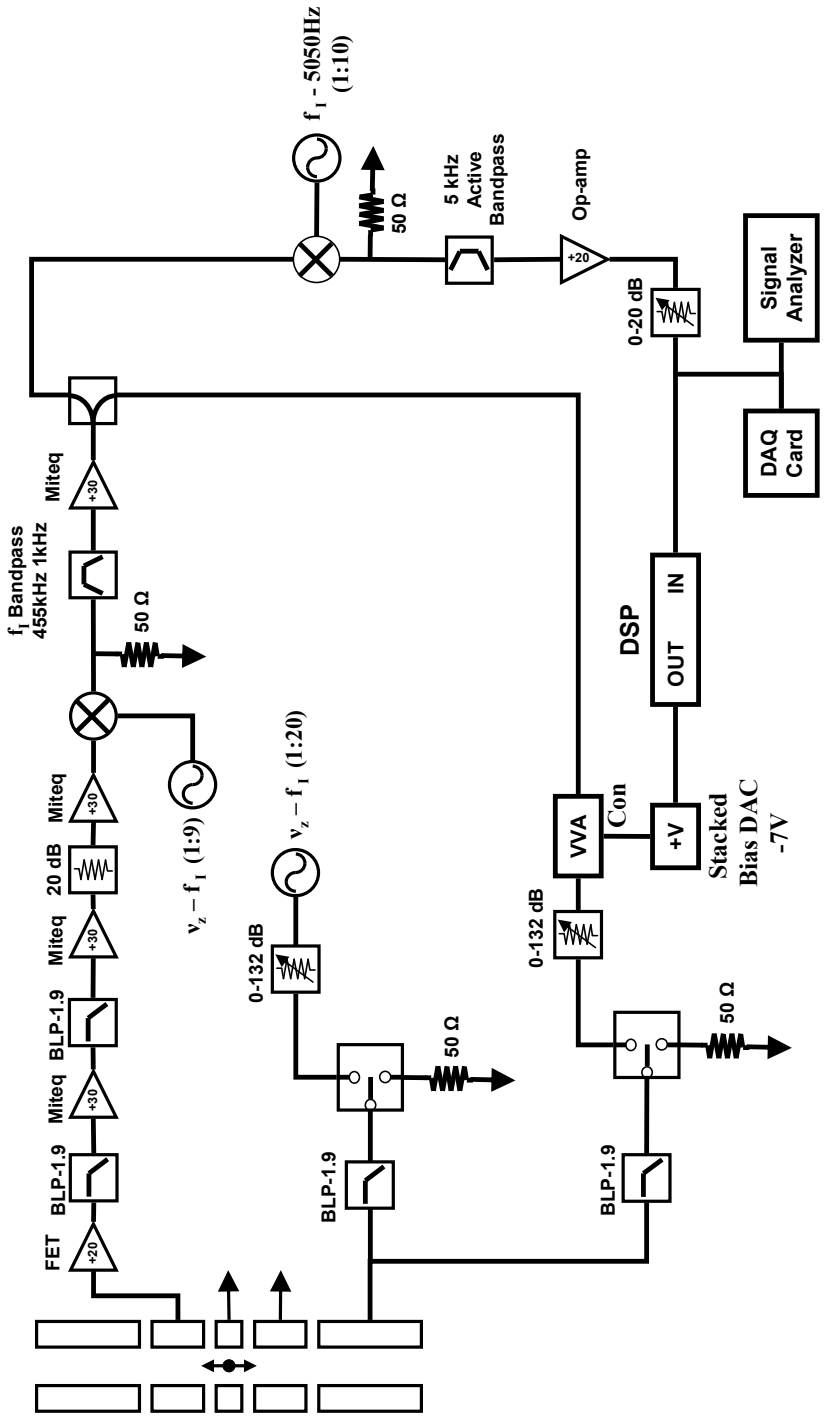

Figure 3.20: The schematic for the self-excited oscillator.

using the SEO. The ratio is optimized by measuring the Allan deviation at different ratios in steps of 4×10^{-5}. Ratio tuning is one of the largest contributors to the axial frequency stability, the other leading factor is the cyclotron state discussed more in Chapter 4.

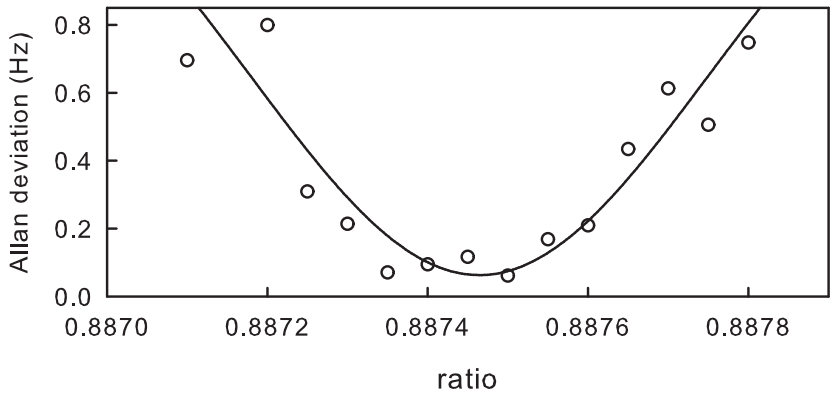

Figure 3.21: One of the largest contributors to the axial frequency stability is the ratio. This shows the Allan deviation for 8 sec averages of the self-excited oscillator as a function of the comp to ring ratio.

3.2.4 Non-Reversing Electric Fields

Initially finding the necessary ring voltage needed to establish an axial frequency can be challenging. Complicating this problem is the fact that to achieve the same axial frequency, the externally applied trapping potentials for protons and antiprotons are not equal and opposite. While initially troublesome, this effect has been characterized and can be accounted for at a high enough precision to facilitate finding the needed trap voltage for a given frequency.

To quantify the non-reversing electric field, we define the trap potential as a sum

of the externally applied voltage, V_{ext}, and a non-reversing voltage V_{nr},

$$V_0 = V_{ext} + V_{nr} \ . \tag{3.14}$$

There is a non-reversing electric field present in both the precision and analysis traps. In the precision trap, V_{nr} = -72 (3) mV. This is similar to previous experiments with copper electrodes, where a V_{nr} = -27 (5) mV has been measured in a trap with a small number of protons and antiprotons (see Eq. 10.9 of Chapter 10 in reference [47]).

In the analysis trap, the non-reversing voltage is substantially higher. Using data from a single proton and antiproton, we extract V_{nr} = +229 (5) mV. While the source of this voltage is unknown, the compiled trap voltages and frequencies are listed in Table 3.1. Further investigation of the temperature stability of this non-reversing voltage may be important for stabilizing the axial frequency.

Table 3.1: The axial frequencies and applied voltages for a proton and antiproton. Using the electrostatic calculation of the trap, a non-reversing voltage can be extracted.

Trap	Particle	ν_z (Hz)	V_{ext} (V)	V_{nr} (mV)
precision	p	568 485	-1.541 980	-70
precision	$\bar{p}$	568 485	1.684 950	-73
analysis	p	919 000	-1.278 405	224
analysis	$\bar{p}$	919 550	0.822 370	234

3.3 Cyclotron Detection

As for the axial motion, cyclotron motion induces an image current that can be damped and detected using a radially split electrode. Connecting a tuned circuit across the two halves of a split compensation electrode breaks the radial symmetry and forces the image current to dissipate energy in the tuned circuit (see Fig. 3.1). Driving the cyclotron motion produces strong signals that are readily detectable. Given the strong magnetic field, the cyclotron motion can be driven up to energies in the keV range before the cyclotron radius approaches the trap radius. Such a high energy and correspondingly large amplitude greatly increases the image current, which goes as $\dot{x} \sim R\omega_c$. Figure 3.22 shows the cyclotron signals from a cloud of less than 100 antiprotons, a few antiprotons and lastly a single particle.

3.3.1 Obtaining a Single Particle

The discrete peaks of the cyclotron signal provide a good way to reduce the number of particles down to one. As discussed further in Sec. 3.3.2, special relativity shifts the cyclotron frequency in an amount proportional to the cyclotron energy. As a result, there are distinct peaks for particles with different energies. After using a filtered noise drive to remove other positive ions loaded with protons [56], or pulsing out electrons loaded with antiprotons [39], the only particle species remaining in the trap is detectable at the proton or antiproton cyclotron frequency. Using the cyclotron signals to monitor the number of trapped particles, the axial potential can be iteratively lowered to spill out a few particles at a time. Monitoring the number of discrete cyclotron peaks gives a clear indication of the remaining particles.

Figure 3.22 shows the process of reducing the number of particles to one. We typically start with a cloud of antiprotons, corresponding to approximately 10-100 antiprotons, the cyclotron signals are dense enough so they are not individually resolved. After dipping the endcaps of the trap to nearly the ring voltage, only a few particles remain and discrete cyclotron peaks are clear. The voltage for dipping the well depends on how many particles are present initially, but a reasonable estimate is typically within 10 percent of the ring voltage.

After the endcaps are lowered and the particles are submitted to the low trapping potential for 1 to 10 seconds, the endcaps are restored to 0 V and the cyclotron peaks are counted. This process is repeated several times until only one peak remains. It may be necessary to excite the cyclotron motion by sweeping a strong drive down in frequency. This downward sweep is necessary to account for the cyclotron frequency change given by the relativistic mass change of the particle, discussed in Sec. 3.3.2. The cyclotron signal from a single antiproton is given by the lone peak in Fig. 3.22 on the right.

3.3.2 Cyclotron Decays

The energy in the cyclotron motion provides a clear example of special relativity [56]. The relativistic mass shift in the cyclotron frequency can be seen by comparing the rest mass, m_0, to the energy of an excited cyclotron motion. The increase in energy alters the effective mass of the particle by the Lorentz factor

$$\gamma = \frac{1}{\sqrt{1 - v^2/c^2}} \, . \tag{3.15}$$

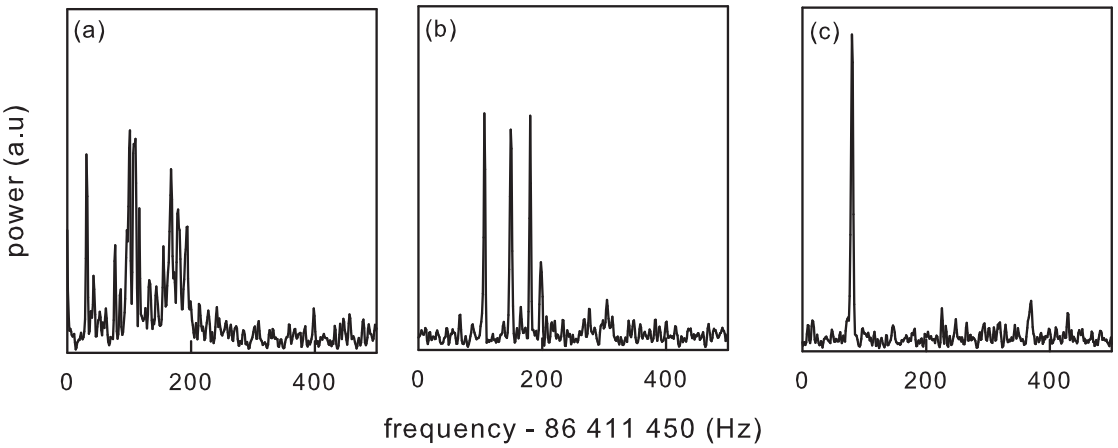

Figure 3.22: Cyclotron signals after repeatedly dipping the endcaps. From left to right, there are (a) <100 antiprotons, (b) 4 antiprotons and (c) just one.

The result is an energy dependent mass, $m = \gamma m_0$, that in turn changes the cyclotron frequency, giving a cyclotron frequency shift proportional to the energy of the motion

$$\frac{\Delta\nu_+}{\nu_+} = -\frac{E_c}{E_c + m_p c^2} \approx -\frac{E_c}{m_0 c^2} \; . \tag{3.16}$$

The rest mass of the proton is approximately 1 GeV. For a readily achievable cyclotron energy of 1 keV, the frequency shift is 1 ppm (approximately 100 Hz out of the approximately 100 MHz cyclotron signal). This frequency shift can be seen in Fig. 3.23.

The damping of the cyclotron motion is quite similar to the axial equation, using the notation of reference [40], the equation of motion is

$$\ddot{v}_x + \gamma_c \dot{v}_x + (\omega_+)^2 v_x = 0 \; . \tag{3.17}$$

Where γ_c is the cyclotron damping rate given by

$$\gamma_c = \left(\frac{e\kappa_c}{2\rho_0}\right)^2 \frac{R}{m} \,. \tag{3.18}$$

This expression is nearly identical to the axial damping rate, except the geometric factor, κ_c, which quantifies the difference between parallel plates and the split electrode, and the length scale is now given by the radius of the trap, ρ_0. It is important to note that the geometric factor for a split comp is higher than the split ring. If the amplifier Q and inductance is unchanged, the damping time decreases by nearly a factor of two with the cyclotron amp on a split comp. The energy decay in the cyclotron motion is given by

$$E_c = E_0 e^{-t/\tau_c} \,. \tag{3.19}$$

Using the fact that the energy of the cyclotron motion is given almost entirely by the kinetic energy of the motion, and the fact that the energy is proportional to A^2, the time constant for the energy decay is given by $\tau_c = 1/(2\gamma_c)$. Combining these factors, we now obtain the time dependence of the cyclotron frequency,

$$\nu_+ = \nu_+(0) - \Delta\nu_+ e^{-t/\tau_c} \,. \tag{3.20}$$

Where $\Delta\nu_+$ is the shift due to the relativistic mass increase in Eq. 3.16 and $\nu_+(0)$ is the zero energy trap modified cyclotron frequency. A typical decay can be seen in Fig. 3.23. This plot is generated by mixing the cyclotron signal down to 5 kHz, taking a Fourier transform using the DAQ card (as was done for the SEO), and tracking the peak frequency as the energy damps in the tuned circuit.

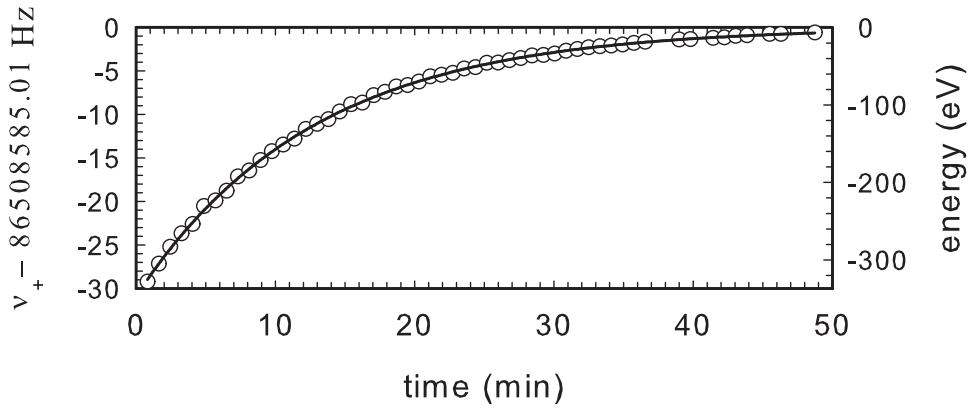

Figure 3.23: The change in cyclotron frequency as the energy damps in the detection circuit.

3.4 Electron Detection

With the cyclotron amplifier located on a split comp, not only is the proton cyclotron signal improved by the increased geometric factor, but the amplifier can also serve as an electron axial amplifier. Detecting electrons is quite useful for antiproton work, which requires electron loading to cool the antiprotons to 4 K. Having an axial amplifier also enables sideband cooling the electron cloud. Lastly, loading electrons is a quick test of the FEP and the trap, providing a useful diagnostic signal after a cooldown. Figure 3.24 shows the signal on the cyclotron amplifier from roughly 200k electrons.

Another way to detect electrons is with the proton axial amplifier, for ring voltages of approximately 1 V in the precision trap. This is a particularly fast and effective way to detect if electrons are still in the trap with antiprotons after electron cooling. We used this signal to test and optimize the electron pulsing technique. With a drive

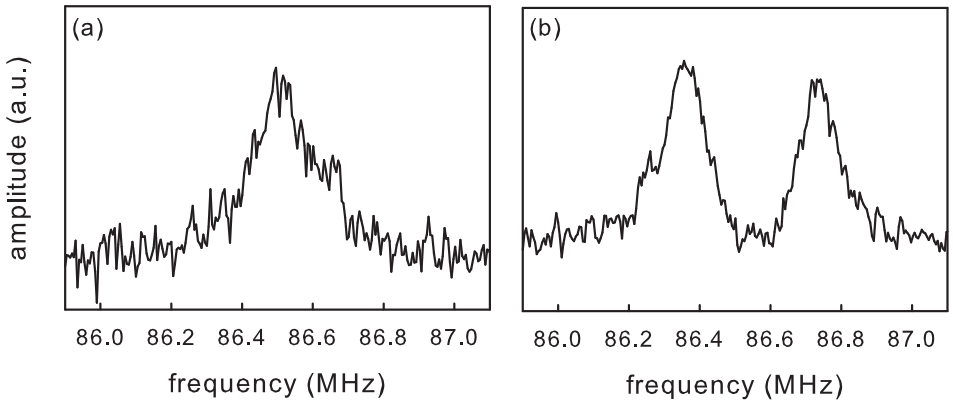

Figure 3.24: (a) The cyclotron amplifier noise resonance with no electrons in the trap. (b) An axial frequency dip from approximately 200k electrons.

at the proton axial amplifier frequency, a clear signal from electrons can be seen at low trap voltages. Figure 3.25(a) shows the driven response from electrons measured with the large axial amp. The cloud is driven at 568 485 Hz, the center of the tuned circuit resonance, producing an increasing response as the ring voltage is lowered.

This driven electron signal provides a relative measurement of electron number before and after pulsing the trap to remove them. Figure 3.25(b) shows the strong electron axial response with a ring voltage of 1 V. After the pulsing, there is no sign of electrons indicating many fewer electrons are in the trap. We have found this technique is sensitive to fewer electrons than the dip method shown in Fig. 3.24. Dips of less than 1000 electrons were visible, but took time to average and seeing fewer electrons was a challenge. However, even when there was no clear electron dip, this driven signal was quite strong, this was important for optimizing the pulsing process. Figure 3.25(c) shows the signal before and after a pulse is applied to remove the electrons. This pulse is then repeated ten times to remove any remnant electrons.

More details on this electron pulsing technique are given in Sec. 6.2.3.

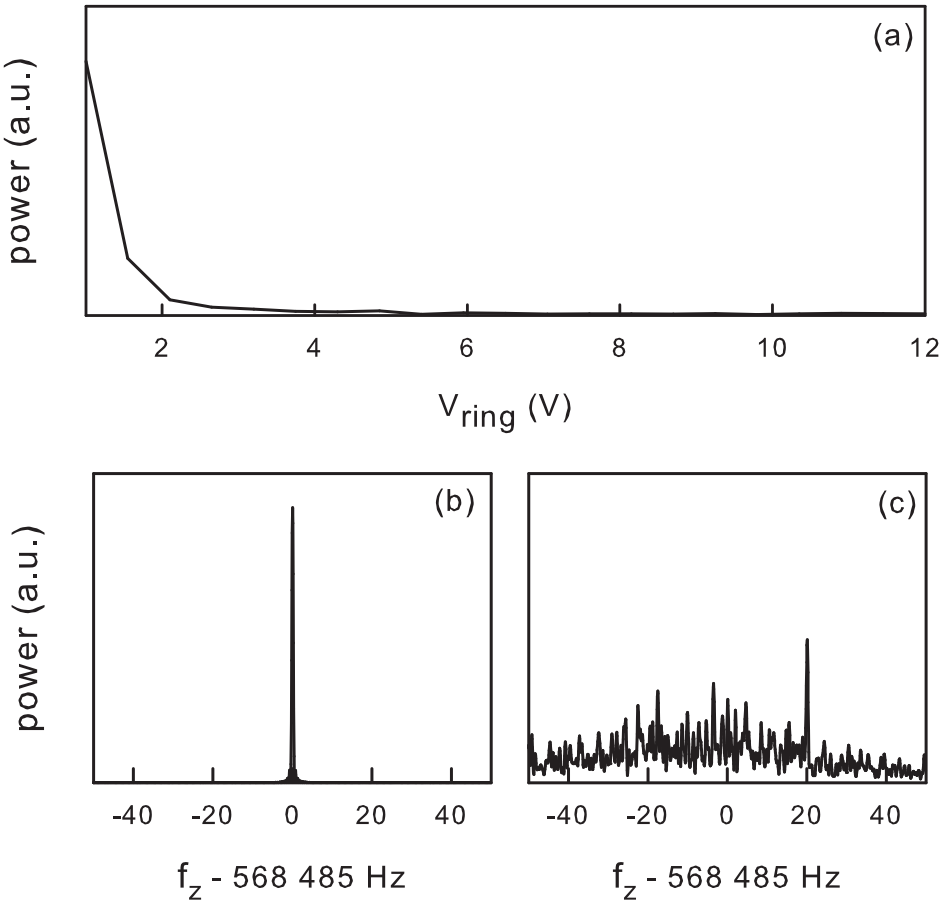

Figure 3.25: (a) The driven signal from electrons on the large axial amplifier as a function of ring voltage. (b) The signal with the ring voltage at 1 V before pulsing the electrons out. (c) The signal at 1 V after pulsing, this shows no signal from electrons.

3.5 Sideband Cooling the Magnetron Motion

Sideband cooling the magnetron motion is an important part of keeping a particle trapped for many months. While the magnetron motion is unstable, as discussed earlier, the radiative damping time is extremely long. However, care must be taken to avoid resistive damping of the magnetron motion, which would cause the radius to grow. In particular, resistive couplings at ω_- between sections of split electrodes must be carefully avoided. Furthermore, noise may drive the particle into a larger magnetron orbit. As a result, the particle is sideband-cooled often to ensure the magnetron radius is small.

Sideband (SB) cooling consists of an oscillating electric field drive, similar to the axial drive. A critical difference is that the SB drive is applied to an electrode that is radially split and offset axially from the center of the trap. This geometry, accomplished using a split comp, is necessary to couple the radial and axial motions [40]. Using this setup, the SB drive is applied at the magnetron sideband of the axial motion, $\nu_z \pm \nu_m$. The cooling drive, $\nu_z + \nu_m$, equalizes the axial and magnetron quantum numbers [40]. Given the frequency hierarchy, an axial temperature in the 4 K range with a frequency in the 1 MHz range translates to a magnetron temperature in the mK range.

The temperature and radius limits to magnetron SB cooling are given by [40, 57]

$$T_m = \left(\frac{\omega_m}{\omega_z}\right) T_z \,, \tag{3.21}$$

$$\rho_m = \sqrt{\frac{4k_B T_m}{m\omega_z^2}} \,. \tag{3.22}$$

Where, T_m and T_z are the magnetron and axial temperatures and k_B is the Boltzmann

factor.

3.6 Driving Spin Flips

A magnetic moment measurement requires driving spin transitions. An oscillating magnetic field perpendicular to the magnetic field of the Penning trap does the job. This field can be written in terms of a co-rotating and counter-rotating terms,

$$\mathbf{B}_1 = \frac{|B_1|}{2}\left(\hat{x}\cos(\omega_s t) - \hat{y}\sin(\omega_s t)\right) + \frac{|B_1|}{2}\left(\hat{x}\cos(\omega_s t) + \hat{y}\sin(\omega_s t)\right). \tag{3.23}$$

By driving current through the halves a split comp, shown in Fig. 3.26, we generate this perpendicular magnetic field at the particle.

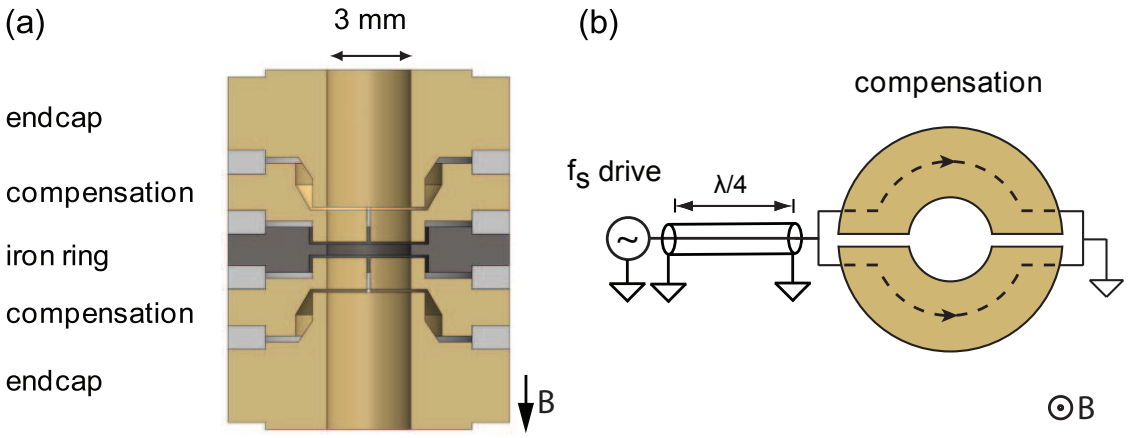

Figure 3.26: (a) The analysis trap with electrode labels. (b)The drive, matching network and current paths used to drive spin flips.

For a drive frequency resonant with the spin transition, the Rabi frequency is given by,

$$\Omega_R = \frac{|B_1|\mu_p}{\hbar}\,. \tag{3.24}$$

If the drive is applied for a certain length of time, t, the probability of a transition is given by the typical two-state Rabi flopping,

$$P_{\uparrow\downarrow} = \left(\frac{\Omega_R}{\Omega'_R}\right)^2 \sin^2\left(\frac{\Omega'_R t}{2}\right), \tag{3.25}$$

Where δ is the drive detuning from $\omega_s = 2\mu_p|B_0|/\hbar$, and $\Omega'_R = \sqrt{\delta^2 + \Omega_R^2}$.

In a Penning trap, the lineshape for the transition modifies this equation to give the approximate transition probability of [40],

$$P_{\uparrow\downarrow} = \frac{1}{2}\left(1 - \exp\left(\frac{-\pi\,\Omega_R^2\,\Delta t}{\Delta\omega_s}\right)\right). \tag{3.26}$$

Where, $\Delta\omega_s$ is the transition linewidth discussed in more detail in Chapter 5. The presence of this linewidth illustrates the challenge of driving spin transitions in the analysis trap. In the large magnetic gradient of the analysis trap, $\Delta\omega_s = 2\pi$ 25 kHz. This is compared to the Hz linewidth in the precision trap. Given the same Rabi frequency, which is set by the trap geometry, it is substantially harder to drive spin transitions in the analysis trap.

Despite this challenge, we have demonstrated the ability to saturate the spin transition. A transmission line transformer is used to minimize the impedance of the current path to the electrode, increasing the current for a fixed drive strength. Using a quarter wavelength line of 10 Ohm coax, the 50 Ohm synthesizer can be matched to a low impedance load. This improvement was important for making the magnetic moment measurement at CERN in the constrained time schedule.

Chapter 4

Axial Stability

4.1 Axial Stability and Averaging Time

As discussed in Chapter 2, the magnetic moment measurements rely on axial frequency stability at approximately the 100 ppb level. This stability is required because the signal from a spin flip is 130 mHz out of the ∼1 MHz axial frequency.

Axial frequency stability is characterized by the Allan deviation of a series of axial frequency measurements. For consecutive frequency measurements, f_i and f_{i+1}, the difference $\Delta_i = f_{i+1} - f_i$, determines the Allan deviation,

$$\sigma_{Allan} = \sqrt{\frac{1}{2N}\sum_{i=1}^{N}(\Delta_i)^2}\ . \tag{4.1}$$

Figure 4.1(a) shows the repeated axial frequency measurements taken using the self-excited oscillator with an averaging time of six seconds. The Allan deviation for longer averaging times comes from averaging these measurements, with the result in Figure 4.1(b). The stability improves until the Allan deviation reaches a minimum

value at an averaging time of roughly 30 seconds and then rises.

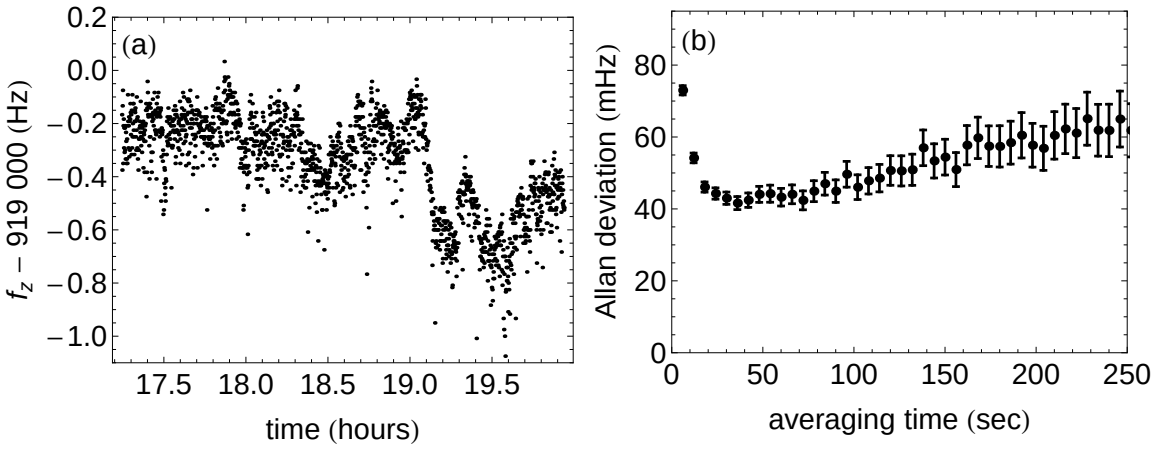

Figure 4.1: (a) Axial frequency measurement using the self-excited oscillator with 6 sec averaging time. (b) Allan deviation computed using the axial frequency measurements in (a) and different averaging times.

4.2 Axial Frequency Stability and Cyclotron Quantum Number

One of the leading contributors to axial frequency instability is the cyclotron quantum number. Figure 4.2 shows how the Allan deviation of the axial frequency increases as a function of cyclotron quantum number. This plot is generated by transferring a proton to the analysis trap before the cyclotron energy has fully thermalized with the tuned circuit in the precision trap. The cyclotron energy is determined in the analysis trap by the resulting axial frequency shift (Eq. 2.20). As illustrated by the dashed line in Fig. 4.2, the Allan deviation increases as the square root of the cyclotron quantum number. This is steepest at low cyclotron quantum numbers. For

reference, a 4 K cyclotron quantum number is $n = 1000$. The data was taken using axial frequency dips with an averaging time of 60 seconds.

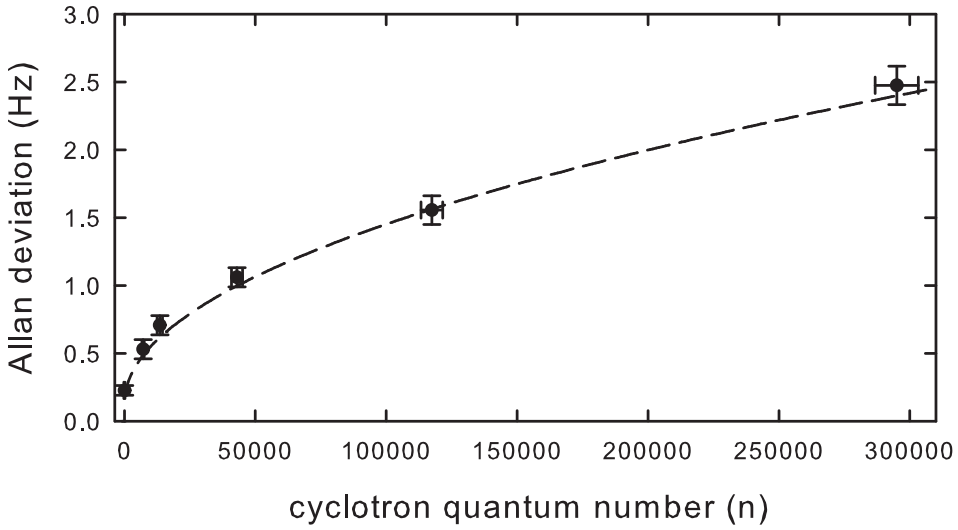

Figure 4.2: The Allan deviation as a function of cyclotron number, showing how the axial frequency stability decreases with increasing n as $\sqrt{n}$ (dashed curve).

4.2.1 Random Walk

The cyclotron quantum number dependence of the Allan deviation can be explained by cyclotron transitions that are driven by electric field noise, with even a small drive strength able to drive cyclotron transitions. The framework for evaluating transition rates for a quantum harmonic oscillator in the presence of a fluctuating uniform driving field has been explored in the neutral atom and ion trapping communities [58, 59]. For a harmonic oscillator in the presence of a fluctuating electric

field perturbation, the result follows from perturbation theory with the Hamiltonian

$$H(t) = H_0 - q\,\epsilon(t)x\,, \tag{4.2}$$

where, $\epsilon(t)$ is the fluctuating electric field and H_0 is the Hamiltonian of a harmonic oscillator at frequency ω [59]. The result from first order perturbation theory for the transition rate from the ground state, $|n=0\rangle$, to the first excited state, $|n=1\rangle$, is [58, 59]

$$\Gamma_{0\to1} = \frac{1}{\hbar^2}\int_{-\infty}^{\infty} \mathrm{d}\tau e^{i\omega\tau}\langle\epsilon(t)\epsilon(t+\tau)\rangle |\langle 0|\,qx\,|1\rangle|^2\,. \tag{4.3}$$

The transition rate can be expressed in terms of the spectral density of the electric field fluctuations is $S_E(\omega) \equiv 2\int_{-\infty}^{\infty}\mathrm{d}\tau e^{i\omega\tau}\langle\epsilon(t)\epsilon(t+\tau)\rangle$ in units of $(\mathrm{V/cm})^2\mathrm{Hz}^{-1}$. The resulting transition rate is [59]

$$\Gamma_{0\to1} = \frac{q^2}{4m\hbar\omega}S_E(\omega). \tag{4.4}$$

The resulting transition rate sets the behavior of the cyclotron quantum number in the presence of a fluctuating electric field. At 4 K, the cyclotron quantum number is ~ 1000. The rate for driving excitations to higher cyclotron quantum numbers is given by $n\Gamma_{0\to1}$, for a transition ending in the quantum number n. This comes from the fact that the dipole matrix element, $\langle n|\,qx\,|n-1\rangle$, grows as $\sqrt{n}$.

The time evolution of the cyclotron quantum number driven by electric field noise is a weighted random walk. The noise drives transitions both up the cyclotron ladder with a rate proportional to n, and down the ladder with a rate proportional to $(n-1)$. Each step in the random walk is more likely to increase n. The average time between transitions is inversely proportional to the transition rate, so we expect the average transition rate to increase as n.

A cyclotron random walk starting in the ground state $|n = 0\rangle$ is shown in Fig. 4.3(a). The cyclotron quantum number grows with time, and the number of transitions increases as n grows. The results of this simulation are shown in Figure 4.3. The data is generated using a weighted random number generator to select if the cyclotron transition is driven up or down. After a time inversely proportional to the cyclotron quantum number, the next transition is generated.

In Fig. 4.3(b), the axial frequency differences are shown for the axial frequency data in Fig. 4.3(a). The plot shows discrete jumps in axial frequency corresponding to one, two or three cyclotron transitions between axial frequency measurements. As expected, because the transition rate depends on the overall cyclotron quantum number, there are more cyclotron transitions for the later times when the cyclotron quantum number is larger.

Using this simulation, we can extract the Allan deviation as a function of averaging time. The result is shown in Fig. 4.4(a), where the simulation data is shown for the axial frequency data of proton starting in a cyclotron quantum number starting at $n = 300$, an experimentally realized quantum number corresponding to 1.5 K. Shown in Fig. 4.4(b) the Allan deviation of the axial frequency data is calculated for different averaging times. Matching the Allan deviation at longer times to the experimental data, we find that a cyclotron transition approximately every 50 seconds can explain the experimental axial frequency stability.

The solid line in the Allan deviation plot of Fig. 4.4(b) shows the expected behavior for cyclotron transitions contributing to the axial frequency instability. The average displacement between the initial and final position for a random walk scales as the

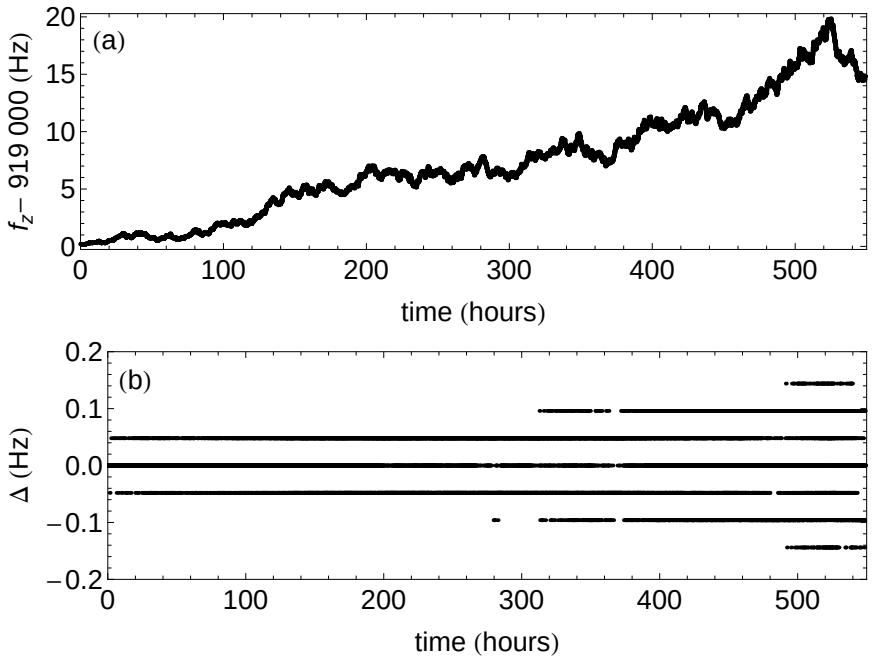

Figure 4.3: (a) The axial frequency in the analysis trap during a cyclotron random walk starting in the cyclotron ground state at t=0. (b) Axial frequency differences showing discrete jumps at integer values of the axial frequency shift from a single cyclotron quantum (50 mHz).

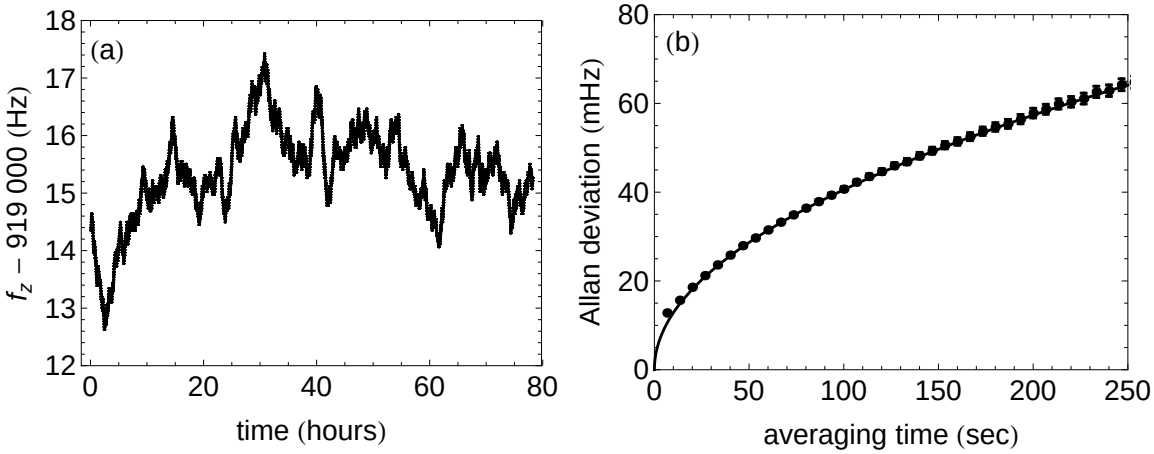

Figure 4.4: (a) The axial frequency for a cyclotron random walk starting at n=300. (b) The Allan deviation using different averaging times for the axial frequency data in (a).

square root of time, matching well with the observed time dependence of the Allan deviation.

4.2.2 Filtering

The cyclotron random walk illustrates the importance of eliminating electric field noise that drives cyclotron transitions. One possible driving field is from room temperature Johnson noise. This is coupled to the experiment through room temperature connections to drive lines, for example on the spin-flip drive line. To quantify the impact of room temperature Johnson noise on the particle, an external cyclotron drive is applied to the drive line. The goal is to compare the strength of the drive to the strength of room temperature Johnson noise, providing an estimate of the Johnson noise driven cyclotron transitions contributing to the axial frequency instability.

Figure 4.5 shows the results for applying a cyclotron drive to the spin flip line. Similar measurements were made using the SB and axial drive lines in the analysis trap, the only other drive lines connected to the analysis trap. While only the SB drive line has the proper symmetry to drive cyclotron transitions, we tested all drive lines in the analysis trap. The Allan deviation is used to quantify the additional cyclotron transitions. From this, it is clear that before filtering the line (the filter is discussed in more detail in the next paragraph), room temperature Johnson noise on the spin flip line was contributing to the background axial frequency instability. The strength of the Johnson noise is estimated using $\sqrt{4k_BTRB}$. Where k_B is the Boltzmann constant, T is the temperature (300 K), R is the resistance (50 Ohms) and B is the bandwidth (roughly 8 kHz using the cyclotron linewidth parameter discussed

in Sec. 5.3). This gives approximately 80 nV_{rms} which corresponds to about -130 dBm.

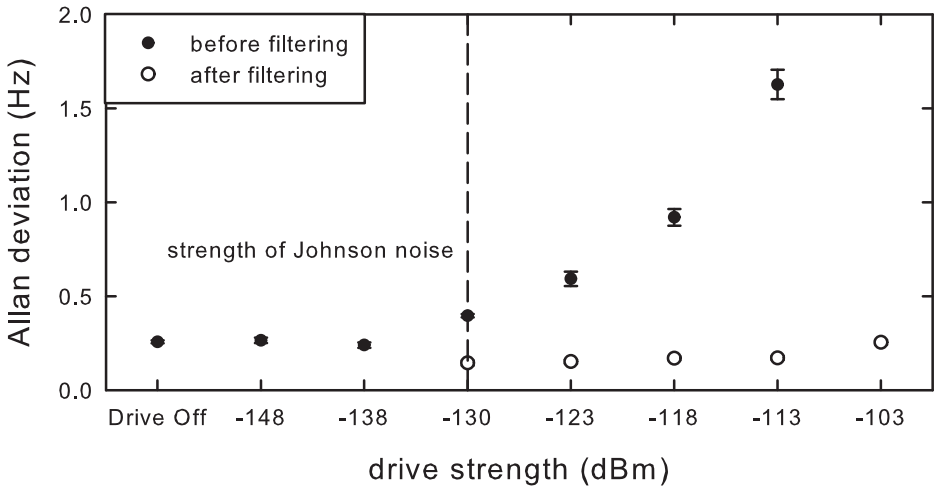

Figure 4.5: The effect of a cyclotron drive on axial frequency fluctuations before and after installing the filter on the spin flip line.

The filter used on the spin flip drive line is a Chebyshev high pass designed to have a 180 MHz corner with a 0.5 dB ripple [60]. The components of the filter are given in Fig. 2.6. A measurement of the attenuation through the filter using a network analyzer is shown in Fig. 4.6. The filter provides roughly 80 dB of attenuation at the cyclotron frequency while the impact on the spin frequency is minimal. The 180 MHz corner was selected because it has similar attenuation at the cyclotron frequency while it presents several dB less attenuation at the spin frequency.

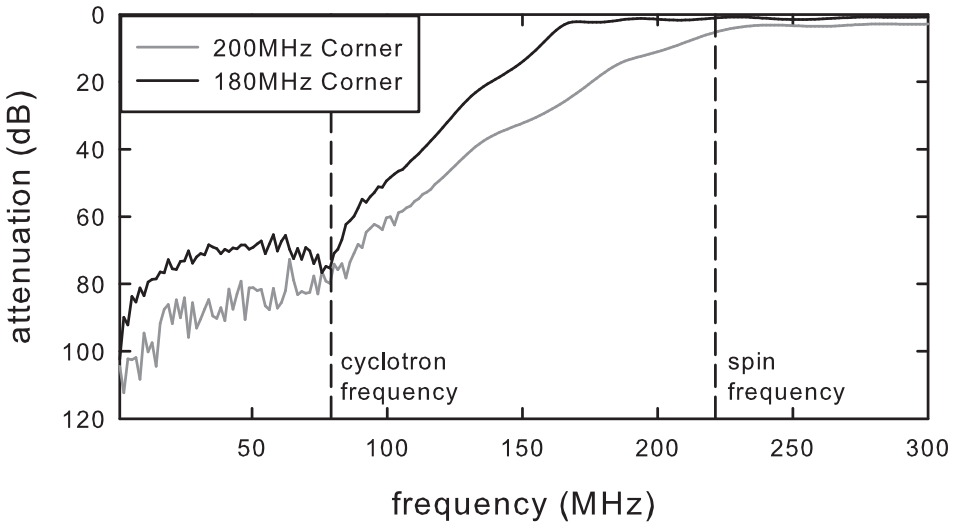

Figure 4.6: The attenuation through two filters for the spin flip drive line.

4.2.3 Comparison to the Quantum Information Community

Much work has been devoted to electric field noise driving unwanted transitions for quantum information studies using trapped ions [43]. Their concern is quite similar to ours, to prevent electric field noise from increasing the quantum number of the particle. In the quantum information experiments, this is in the context of the axial motion, and for our experiments we are interested in the cyclotron motion.

Much progress has been made in characterizing the electric field noise in ion traps [61, 62, 63]. The are several important features of the noise form these investigations. The first is the frequency scaling of the spectral density: S_E falls off as $1/f$ [63, 64]. Also observed is a product of the frequency and spectral density, ωS_E, that scales as d^{-4}, where d is the size of the trap [63, 64]. Another interesting feature is that the noise appears to be smaller for low temperature experiments [61, 63, 64].

Using the experimentally measured values from the quantum information community, we can scale the results to our experiment [63, 64].

An estimate of the spectral density observed for cryogenic experiments is $S_E = 10^{-6}$ V/m^2 for a trap size of 100 μm [63, 64]. Scaling this to our 80 MHz cyclotron frequency with trap radius 1500 μm, and using Eq. 4.4, for a cyclotron quantum number of 300 we obtain a transition rate of less than 1 mHz. While the extrapolation is a large one, it is used to get some comparison. This indicates less than 1 cyclotron transition in approximately 10^3 seconds. Our observed transition rate of approximately 1 cyclotron transition in 50 seconds is substantially higher than this. However, given the spread in cryogenic heating rates reported in reference [64], we cannot rule out that we are limited by the noise seen in the quantum information community. We are encouraged to further investigate this possible limit as well as investigate other noise sources that may be driving transitions on split electrodes.

Chapter 5

Proton Magnetic Moment Measurement

5.1 Observing Single Proton Spin Flips

For the magnetic moment measurement, it is necessary to measure the spin and cyclotron frequencies, as discussed in Sec. 2.2. We use the magnetic gradient created by the iron ring to couple the spin and cyclotron states to the axial frequency, Sec. 2.3.1. This allows us to detect changes in the proton's spin and cyclotron state from shifts in the axial frequency. Detecting a resonant spin drive is challenging because a flip between the two spin states shifts the axial frequency by only one part in ten million. The cyclotron frequency is relatively easier to detect because we can access many states in the cyclotron ladder, creating a larger shift in the axial frequency from a resonant cyclotron drive.

5.1.1 Measurement Sequence

The data taking procedure used to observe spin flips relies on repeated measurements of the axial frequency. The detection cycle of the axial frequency measurement is shown in Fig. 5.1. The axial frequency is measured three times, f_1, f_2, and f_3. Between f_1 and f_2, a spin flip drive is applied. The differences f_2-f_1 comprise the σ_f distribution. Between f_2 and f_3, a detuned drive is applied, and the differences f_3-f_2 make up the σ_0 control distribution. We measure the σ_0 distribution to determine the size of the background axial frequency scatter not caused by spin flips. The drives is detuned rather than off (50 kHz below resonance) to control for any possible effects of the strong drive other than flipping the spin state. At the end of the cycle, feedback cooling and sideband cooling are simultaneously applied to reduce the magnetron radius. Feedback cooling during SB cooling is applied to minimize the unwanted radial change associated with selecting a new magnetron state from the Boltzmann distribution. This effect is discussed further in Section 5.3 and reference [4].

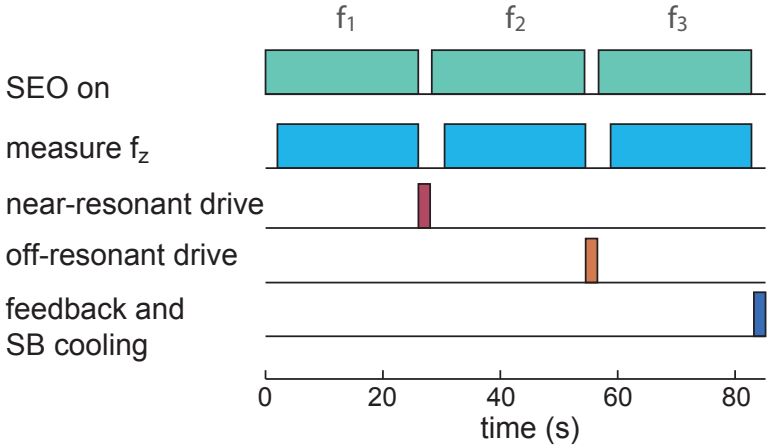

Figure 5.1: The measurement sequence for the spin line.

5.1.2 Resolving Spin Flips

To assess the possibility of observing spin flips and to extract the spin excitation fraction from the data, it is necessary to have a quantitative understanding of the time-averaged signal from spin flips. The technique used to detect spin flips relies on computing the differences between adjacent axial frequency measurements. The Allan deviation quantifies the axial stability. The Allan deviation increases when a resonant spin flip drive flips the spin between adjacent axial frequency measurements, compared to the differences measured when the off-resonant drive is applied.

The control Allan deviation, σ_0, when a control drive is applied for N measurement cycles is

$$\sigma_0 = \sqrt{\frac{1}{2N}\sum_{i=1}^{N}(\Delta_i^c)^2}\,. \tag{5.1}$$

The difference $\Delta_i^c = f_{3,i} - f_{2,i}$ is between adjacent axial frequency measurements for the control drive. For a near-resonant spin flip drive, $\Delta_i^s = f_{2,i} - f_{1,i}$, and the spin flip Allan deviation is given by

$$\sigma_f = \sqrt{\frac{1}{2N}\sum_{i=1}^{N}(\Delta_i^s)^2}\,. \tag{5.2}$$

To compare the off-resonant and near-resonant spin flip Allan deviations, we can use the control differences as the background axial frequency differences and add the corresponding spin flip shifts $\pm\Delta_s$ to spin flip events. If there are number of M_{up} spin flips up and M_{down} spin flips down, causing axial frequency shifts Δ_s and $-\Delta_s$ respectively, the spin flip Allan deviation is now

$$\sigma_f = \sqrt{\frac{1}{2N}\left(\sum_{i=1}^{M_{up}}(\Delta_i^c + \Delta_s)^2 + \sum_{i=M_{up}+1}^{M_{up}+M_{down}}(\Delta_i^c - \Delta_s)^2 + \sum_{i=M_{up}+M_{down}+1}^{N}(\Delta_i^c)^2\right)}. \quad (5.3)$$

Using the fact that there is approximately an equal number of spin flips up and down, and that for a total of N measurement cycles, the spin flip probability is $(M_{up} + M_{down})/N$,

$$\sigma_f \approx \sqrt{\sigma_0^2 + \frac{P}{2}\Delta_s^2}. \quad (5.4)$$

This gives an expression for the excitation fraction, P, in terms of the measured Allan deviations,

$$P = \frac{2(\sigma_f^2 - \sigma_0^2)}{\Delta_s^2}. \quad (5.5)$$

Under the assumption that the background distribution is Gaussian, we can assign uncertainty to the Allan deviations. This is given by

$$\delta\sigma_{Allan} = \frac{\sigma_{Allan}}{\sqrt{2N-2}}\,. \quad (5.6)$$

The difference $\sigma^2 = \sigma_f^2 - \sigma_0^2$ is the signal caused by flipping spins. The uncertainty is the quadrature sum of the uncertainties in the two Allan deviations (from Eq. 5.6).

The fractional uncertainty sets the number of axial frequency measurements needed for a statistically significant demonstration of spin flips. For a control Allan deviation of 70 mHz and a modest spin flip excitation fraction of 0.25, to achieve a four sigma measurement (i.e. $\sigma_f^2 - \sigma_0^2$ is four times the error), 400 detection cycles and 10 hours are needed.

Fig. 5.2(a) shows the axial frequency measurements and Fig. 5.2(b) shows the Allan deviation of all the previous frequency measurements as a function of time for

a resonant spin flip drive. The Allan deviations are σ_0 =62 (2) mHz and σ_f =77 (3) mHz for the off-resonant control and near-resonant drives respectively. This gives a spin flip probability of 0.25 (6), representing a four sigma demonstration of spin flips. For the spin drive below resonance, shown in Fig. 5.3, the Allan deviations are 69 (2) mHz and 69 (2) mHz for the σ_0 and σ_f respectively. This gives an excitation fraction of -0.01 (6), consistent with no spin flips.

Histograms of the differences Δ_i^c confirm the assumption of a Gaussian distribution for the background. Figure 5.4 shows the differences data for the axial data presented in Fig. 5.2 and Fig. 5.3. The control data is the gray histogram with the dashed line showing the Gaussian fit. The spin flip data is the outline histogram, with the solid line showing the Gaussian fit. In Fig. 5.4(a), the difference between the widths of the dashed and solid line fits indicates the presence of spin flips. This difference is the four sigma result discussed previously. In Fig. 5.4(b), the spin flip and control data display the same width, the two Gaussian fits give the same Allan deviation, consistent with no spin flips. Using this technique, it is possible to take data for a spin line shape by measuring σ^2 at different drive frequencies.

5.1.3 Drive Strength Systematic

When measuring the spin frequency, it is important to consider possible systematic effects. One concern is that the strong drive used to drive spin transitions causes a Bloch-Siegert shift of the spin frequency. However, this scales as Ω_s^2/ω_s^2, where Ω_s is the Rabi frequency and ω_s is the angular spin frequency [65, 40]. For the drive strength used here, this shift is several orders of magnitude below even the ppb level.

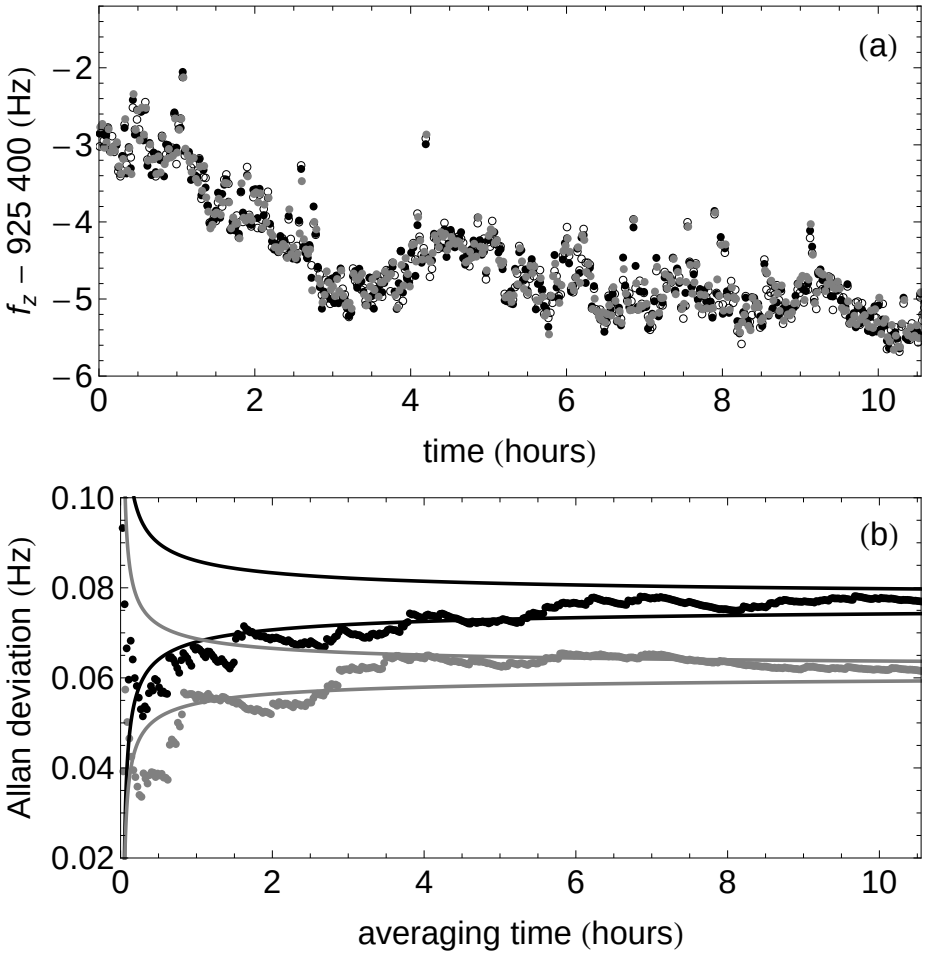

Figure 5.2: (a) The axial frequency measurement using a control drive and resonant spin drive. (b) The Allan deviation of all the previous axial frequency measurements as a function of time. The Allan deviation for the control drive in gray with the near resonant drive in black. There is a clear difference in the Allan deviations after 10 hours of averaging, yielding a 4σ demonstration of spin flips.

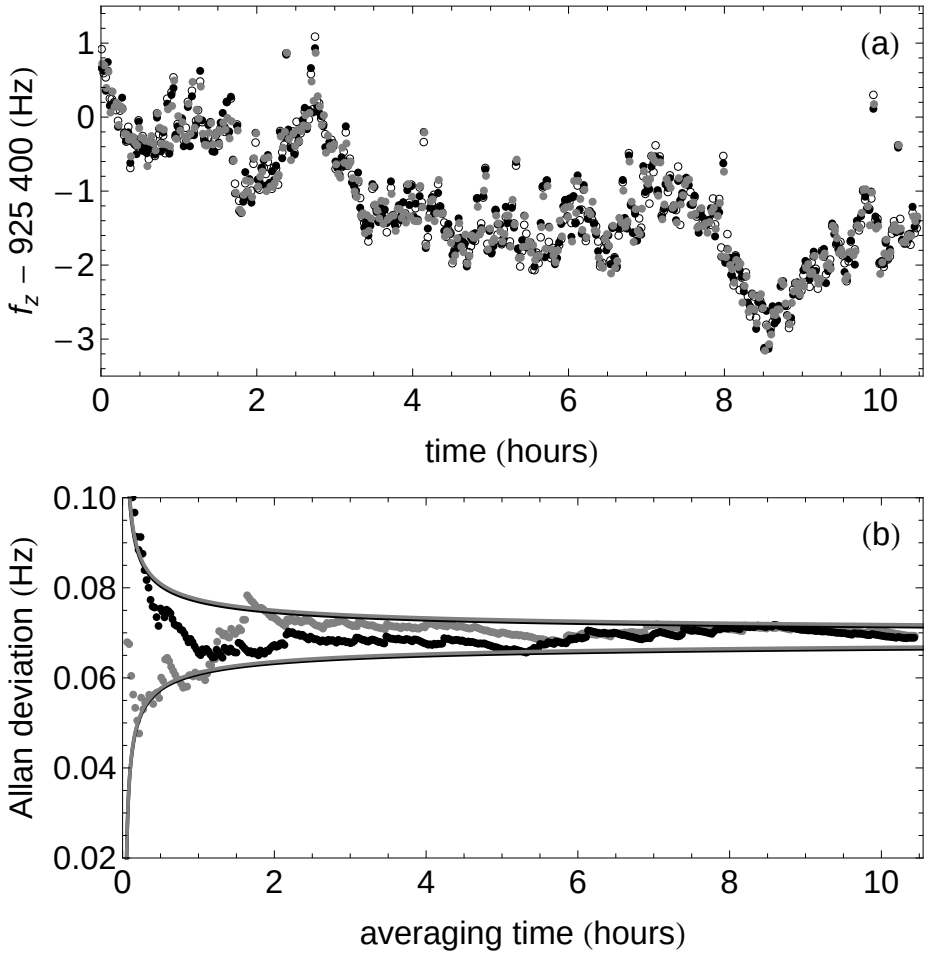

Figure 5.3: (a) The axial frequency measurements for a control drive and spin flip drive below resonance. (b) The Allan deviation of all the previous frequency measurements as a function of time. The Allan deviation for the control drive in gray with the non-resonant spin drive in black. There is no difference in the Allan deviations after 10 hours of averaging, indicating no spin flips.

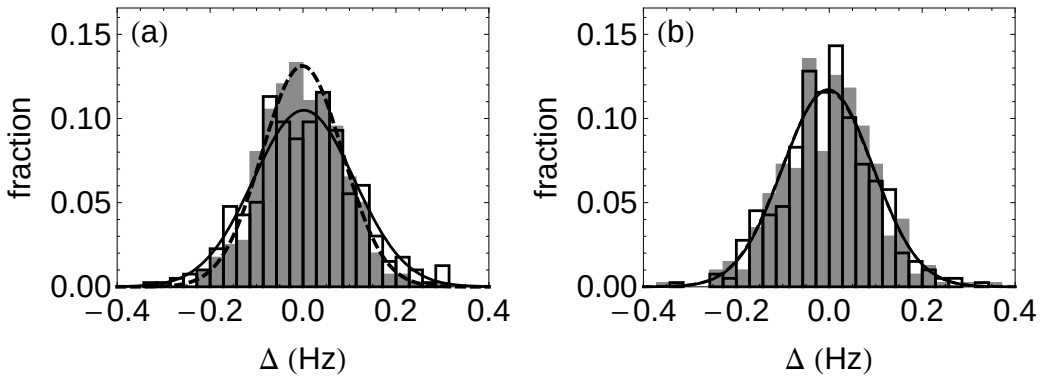

Figure 5.4: (a) The histograms of axial frequency differences for the control drive in gray and the near resonant spin drive in outline. The dashed Gaussian is a fit to the control drive data and the solid line is a fit to the near resonant drive data. (b) The histograms for the non-resonant spin drive data. The spin drive data is in outline and the control data in gray. The Gaussian fits to the control and spin drives are respectively shown by a dashed and solid line, the fits overlap showing a single solid line.

Another concern for the strong drive is an axial frequency shift while the spin drive is applied. Through the invariance theorem, such a shift would change the free space cyclotron frequency. As a result, the spin frequency would be measured at a shifted cyclotron frequency, adding a systematic shift to the magnetic moment measurement. Figure 5.5 shows the axial frequency shift measured using axial frequency dips as a function of spin drive strength. The axial frequency shifts decrease the frequency as the drive strength increases, presumably because the average trapping potential is slightly modified by the strong drive. Extrapolating the observed shift to the full drive strength gives an axial frequency difference of nearly 300 Hz. However, this offset shifts the free space cyclotron frequency by less than 50 ppb, well below the measurement uncertainty.

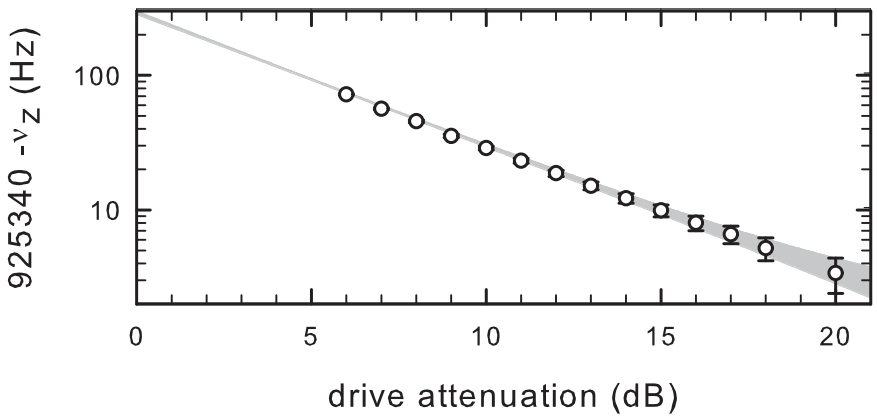

Figure 5.5: The axial frequency shift as a function of spin flip drive strength. The overall shift contributes 50 ppb uncertainty to the magnetic moment measurement, well below other uncertainties of the measurement.

5.2 Measuring the Cyclotron Frequency

In contrast to the spin frequency, the cyclotron frequency is comparatively easy to measure. To initially find the approximate cyclotron frequency, a relatively strong drive can be used. The drive is first detuned well below resonance, where it causes no cyclotron transitions. The drive is then stepped up in frequency while the axial frequency is monitored. When the drive is above the sharp edge of the line shape, the axial response shifts up significantly in frequency. This strong drive technique was used to initially find the cyclotron frequency to a precision of roughly 50 kHz or a part per thousand. The SEO is a good choice for this initial measurement because the high signal-to-noise provides a clear signal in seconds, rather than the minute it would take using an axial frequency dip.

A more precise initial knowledge of the cyclotron frequency is needed when the

precision goal of the magnetic moment measurement is at the ppm level. Therefore, an intermediate drive strength is used for a more precise measurement. It is important to note, this drive is stronger than the drive used for the actual line shape measurement. Using the intermediate drive, the process is similar to before: the drive starts below resonance and is stepped up in frequency while the axial response is monitored using dips.

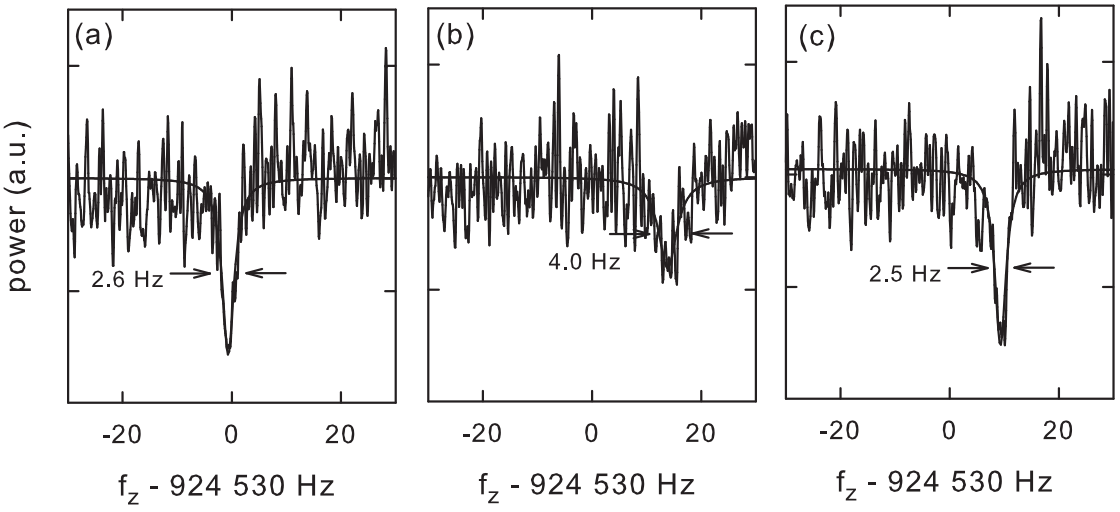

Figure 5.6: Monitoring a dip at different cyclotron drive frequencies. (a) The drive is several kHz below resonance causing no noticeable cyclotron transitions. (b) The drive is slightly above resonance, the clear shift up in axial frequency along with the wide dip indicate cyclotron transitions. (c) The drive is approximately 20 kHz above resonance, the dip is again narrow indicating few transitions at this drive frequency, but the cyclotron energy remains and the axial frequency is higher than initially in (a) because this dip is taken after (b).

As shown in Fig. 5.6(a), when the drive is below resonance, the dip width is given by the damping width and the response is centered in the window. When the drive is resonant, the dip width is substantially wider and the frequency is higher by about

15 Hz, indicating a change in cyclotron state by 300 quanta. When the drive is far above resonance, by approximately 20 kHz, the dip is again sharp with the expected width, but the added cyclotron energy remains and the axial frequency is higher than it was initially. Using this technique, the leading edge of the cyclotron resonance can be found to better than 1 kHz (roughly 10 ppm).

The cyclotron line shape measurement uses a still weaker drive, one that does not noticeably widen the dip or shift the axial frequency when applied continuously for several hours. The goal is to increase the cyclotron transition rate just enough to measure the resonance using axial frequency differences while keeping the proton in essentially the same cyclotron radius. The resolution of axial frequency differences allows us to measure the change in cyclotron state of just a few quanta (the change in axial frequency is 50 mHz per cyclotron quantum). Figure 5.7 shows the change in axial frequency between the first and last axial data points at each cyclotron drive frequency. The mean difference for a near-resonant drive, less than 5 kHz above resonance, translates to a change in cyclotron state of 30 ± 90 quanta. This corresponds to a change in cyclotron radius of 10 ± 25 nm for a 4 K proton. This radius change is much smaller than the typical change from magnetron sideband cooling which is 5 μm for a 4 K axial temperature.

5.3 Line Shapes

The line shape for the spin and cyclotron resonances [40] arise from the magnetic gradient and the axial temperature. In the magnetic field $B\hat{z}$, the iron ring creates a

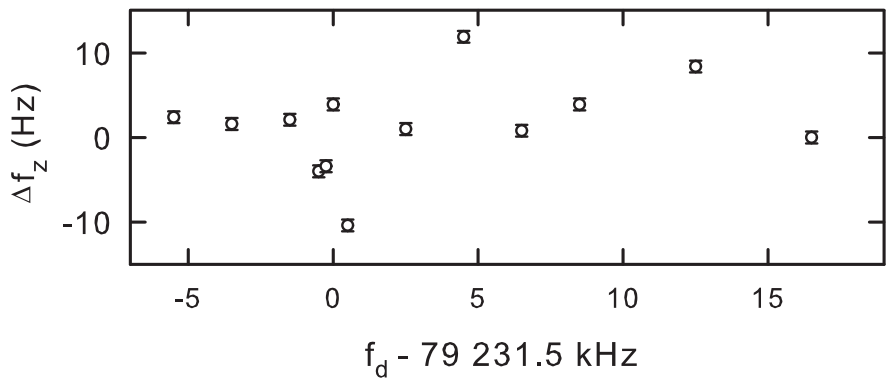

Figure 5.7: The difference between the first and last axial frequency data points for each cyclotron drive.

magnetic field gradient of the form

$$\Delta\mathbf{B} = B_2[(z^2 - \rho^2/2)\hat{z} - z\rho\hat{\rho}\,]. \tag{5.7}$$

In this gradient, changes in the particle's axial amplitude and radius change the magnetic field. As a result, thermal fluctuations in the axial oscillation amplitude from the coupling to the axial amplifier contribute a broadening to the spin and cyclotron lines. In addition, the axial thermal distribution is mapped to the magnetron radius during sideband cooling, contributing a broadening from the radial gradient.

Considering first the axial motion in the gradient, for a particle on axis, $\rho = 0$. In this case, the spin and cyclotron frequencies ω in the magnetic gradient are related to the gradient free frequencies ω_0 by

$$\omega = \omega_0(1 + \frac{B_2}{B}z^2)\ . \tag{5.8}$$

The broadening due to the magnetic gradient can be expressed as a linewidth parameter of the spin or cyclotron resonance. A linewidth parameter $\Delta\omega_z$ from the axial temperature comes from Eq. 5.8 and using the equipartition theorem, $\frac{1}{2}m\omega_z^2\langle z^2\rangle = \frac{1}{2}k_BT_z$:

$$\Delta\omega_z \equiv \omega_0 \frac{B_2}{B}\langle z^2\rangle = \omega_0 \frac{B_2}{B}\frac{kT_z}{m\omega_z^2}\,. \tag{5.9}$$

The linewidth is determined by the relative size of $\Delta\omega_z$ and other time scales. For example, if the axial damping rate γ_z is slower than the spin or cyclotron linewidth, that is $\gamma_z << \Delta\omega_z$, then the axial amplitude is essentially unchanged during the excitation [40]. In this case, the spin or cyclotron resonance is a narrow Lorentzian, located at a frequency determined by the axial amplitude. If the drive process is repeated many times, spaced out in time longer than γ_z^{-1}, the axial amplitude and hence spin or cyclotron frequency will be different. This identifies the basic features of the line shape, the minimum magnetic field is at zero axial amplitude, which is the most likely oscillation amplitude from the Boltzmann distribution. Therefore, the spin and cyclotron line shapes have an abrupt leading edge from the low frequency direction and the high frequency tail is set by an exponential decay specified by the Boltzmann distribution. From this we have the line shape in this limit, which applies for the experiments presented here with $\gamma_z/(2\pi) = 2$ Hz $<< \Delta\omega_z/(2\pi) = 25$ kHz. Further discussion of the line shapes, other limits and the general expressions can be found in references [40, 66, 67, 68].

The line shape for low drive intensity [40] is

$$\chi(\omega) = \frac{\theta(\omega-\omega_0)}{\Delta\omega_z}\exp\left(-\frac{\omega-\omega_0}{\Delta\omega_z}\right). \tag{5.10}$$

Where ω is the angular frequency of the spin or cyclotron motion, ω_0 is the zero axial amplitude spin or cyclotron frequency, $\Delta\omega_z$ is the previously defined linewidth

parameter, and $\theta(x)$ is the step function with

$$\theta(x) = 0 \quad \text{for } x < 0\,, \tag{5.11}$$

$$\theta(x) = 1 \quad \text{for } x > 0\,. \tag{5.12}$$

The magnetron motion also contributes to the line shapes because every application of sideband cooling equalizes the magnetron and axial quantum numbers. This effectively maps the axial Boltzmann distribution onto the magnetron distribution [4]. To account for this, we can derive the magnetron line shape using a similar calculation to the axial line shape. One key difference is that the magnetic field decreases as the radius increases (see Eq. 5.7), so the line shape will have an abrupt leading edge from the high frequency side and an exponential tail from the Boltzmann distribution. The other main difference is that the magnetron temperature is much lower than the axial temperature because of the frequency hierarchy [40]

$$T_m = \frac{\omega_m}{\omega_z} T_z. \tag{5.13}$$

This and a factor of two from the bottle term means the relative line widths for the magnetron and axial broadening are

$$\Delta\omega_m = \frac{2\omega_m}{\omega_z} \Delta\omega_z. \tag{5.14}$$

The line shapes are shown in Fig. 5.8. The axial line shape is on the left and the magnetron line shape is on the right. The expected total line shape is given by convolving the axial and magnetron line shapes with the proper linewidths. The combined line shape is

$$\chi(\omega) = \frac{1}{\Delta\omega_z + \Delta\omega_m} \left[\left(\frac{1 - \theta(\omega - \omega_0)}{\Delta\omega_m} \right) \exp\left(-\frac{\omega - \omega_0}{\Delta\omega_m} \right) + \frac{\theta(\omega - \omega_0)}{\Delta\omega_z} \exp\left(-\frac{\omega - \omega_0}{\Delta\omega_z} \right) \right]. \tag{5.15}$$

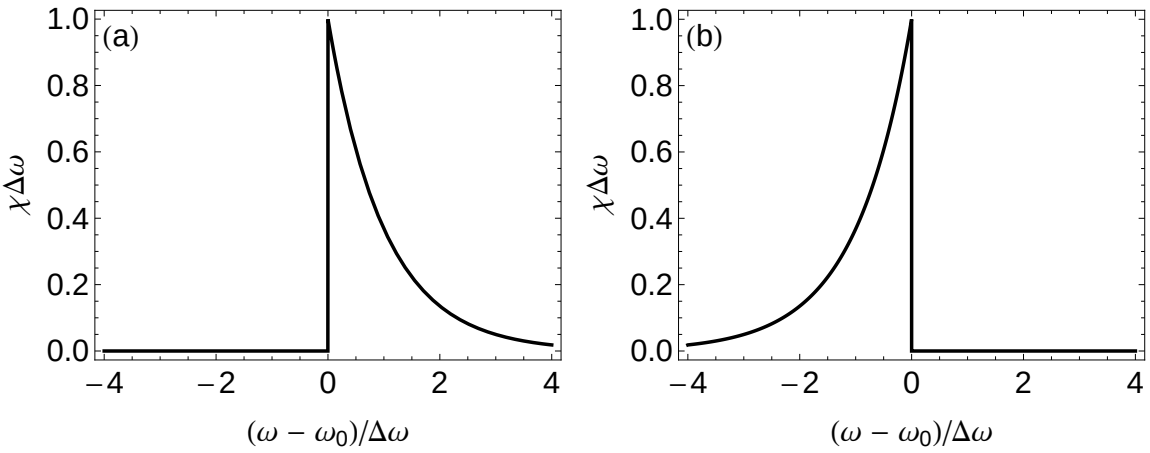

Figure 5.8: (a) The spin or cyclotron frequency line shape caused by the thermal axial motion in the bottle field. (b) The corresponding line shape caused by sideband cooling the magnetron motion in the bottle field.

The line shape predicted by this equation is shown in Fig. 5.9. The low frequency magnetron component to the line is for a 4 K axial temperature, established by feedback cooling while sideband cooling. The high frequency axial component to the line is for an axial temperature of 8 K. This axial temperature is higher because feedback is not used while the spin or cyclotron drive is applied.

5.3.1 Temperature Measurement

An important parameter for the line shape is the axial temperature during the drive and the sideband cooling sections. This can be measured using the axial frequency differences when a sideband drive is applied [4]. For example, the feedback cooling temperature can be extracted by using the differences $f_{3,i} - f_{1,i+1}$. The result from this difference gives the sideband cooling difference in the axial frequency. To extract the temperature of the differences, the line shape for the distribution is

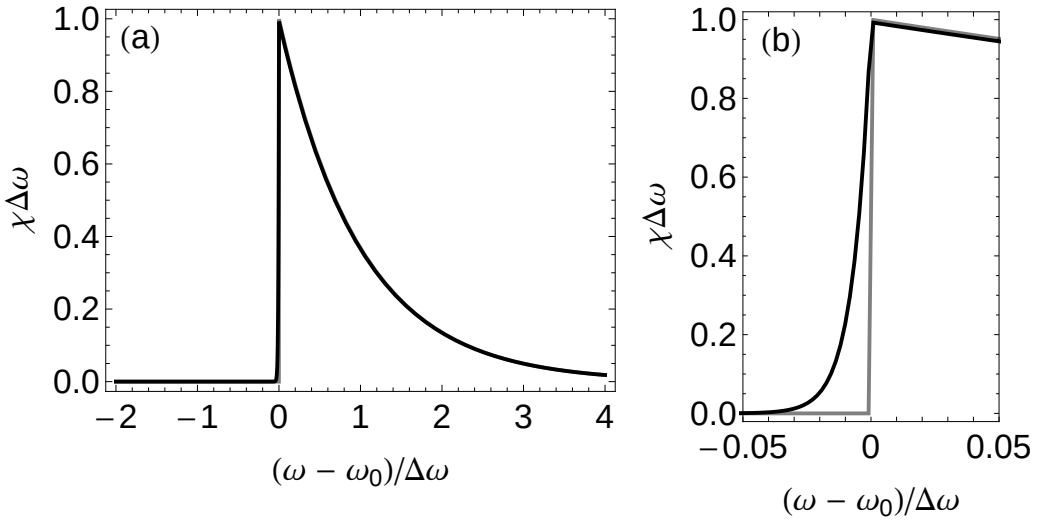

Figure 5.9: (a) The expected line shape of the spin and cyclotron frequency accounting for the thermal broadening from the axial and magnetron motions in the bottle field. (b) A closer view of the magnetron contribution to the leading edge of the line shape.

needed. In the limit of no background fluctuations, the expected line shape is simply given by the Boltzmann distribution. The gray line in Fig. 5.10 shows this result. To account for the background scatter, the Boltzmann distribution result must be convolved with a Gaussian of the appropriate width. This result is plotted in black.

The result of convolving the two line shapes yields an expression that can be numerically integrated to obtain the result in Fig. 5.10. While the difference between the more complicated model and the simple Boltzmann is not so important at this stage, it may be necessary when measuring lower axial temperatures achieved with improved feedback cooling.

The normalized probability of measuring a certain difference in magnetron quan-

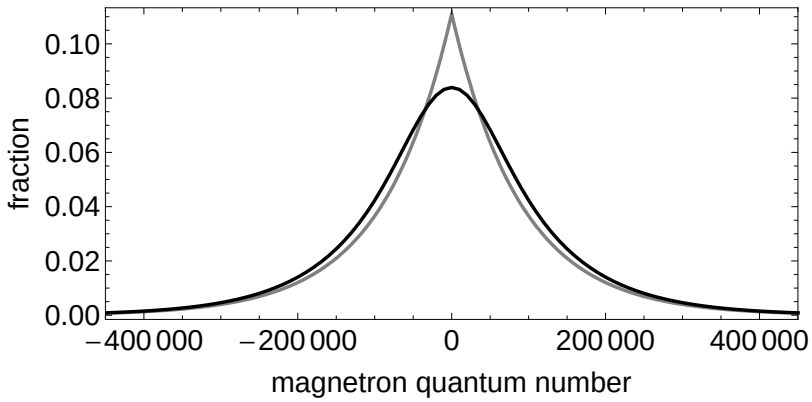

Figure 5.10: The expected line shapes for the axial temperature measurement. The simple Boltzmann result in gray and the result with the Gaussian background convolved with the Boltzmann distribution is in black. Both are plotted for an axial temperature of 4 K.

tum number is given by

$$P_{diff} = \frac{\sum_{\ell=0}^{\infty} P_\ell P_{\ell+diff}}{\sum_{\ell=0}^{\infty}\sum_{diff=0}^{\infty} P_\ell P_{\ell+diff}} \; . \tag{5.16}$$

Where ℓ is the magnetron quantum number and P_ℓ is the probability of measuring this magnetron quantum number. For the simple case of the Boltzmann distribution, defining $\alpha = \frac{h\nu_z}{kT_z}$, the probability is simply

$$P_\ell = \alpha \exp(-\alpha\ell) \; . \tag{5.17}$$

We have omitted the additional $1/2h\nu_z$ which doesn't have a large impact considering $\ell \approx 10^5$. Including the Gaussian background gives

$$P_\ell = \frac{\alpha}{2} \exp(-\alpha\ell + \alpha\kappa^2/2) \left[1 + \mathrm{Erf}\left(\frac{\ell - \alpha\kappa^2}{\sqrt{2}\kappa}\right)\right] . \tag{5.18}$$

Where κ is the standard deviation of the background fluctuation Gaussian, in units of magnetron quantum number. The error function Erf comes from convolving the

Gaussian with the exponential. The results from using these probability distributions in Eq. 5.16 is plotted in Fig. 5.10.

Figure 5.11 shows the result from data taken for the proton magnetic moment measurement. The gray histogram are the control differences while the outline histogram are the differences with the sideband cooling drive applied between the axial frequency measurements. The dashed line is the Gaussian fit used to account for the background scatter and the solid line is the result from convolving the background scatter with a 4 K Boltzmann distribution. This gives a magnetron linewidth axial temperature, corresponding to a broadening of 0.7 ppm. The axial temperature without feedback cooling was also measured using this technique to give a temperature of 8 K, roughly 100 ppm.

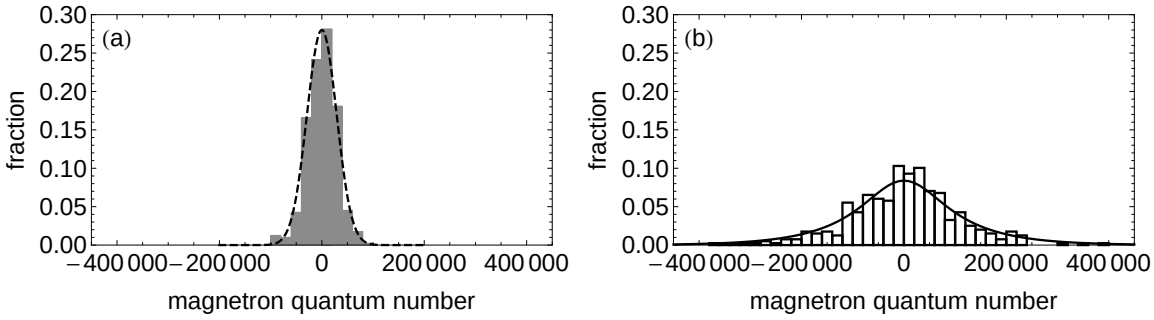

Figure 5.11: The histogram of axial frequency differences with no sideband cooling in gray (a) and sideband cooling in outline (b). The background fits well to a Gaussian shown by the dashed curve. Using the model, the differences match well to a 4 K temperature shown by the solid line.

5.4 Magnetic Moment Measurement

These techniques made possible the first single particle measurement of the proton magnetic moment [1]. The result is a 2.5 ppm measurement of the magnetic moment expressed in terms of nuclear magnetons, μ_N,

$$\frac{\mu_p}{\mu_N} \equiv \frac{g_p}{2} = 2.792\,846\,(7)\,[2.5\text{ ppm}]\,. \tag{5.19}$$

We have profited from parallel work of proton spin flips [9]. A proton magnetic moment measurement with a 8.9 ppm precision was consistent with our earlier measurement [10].

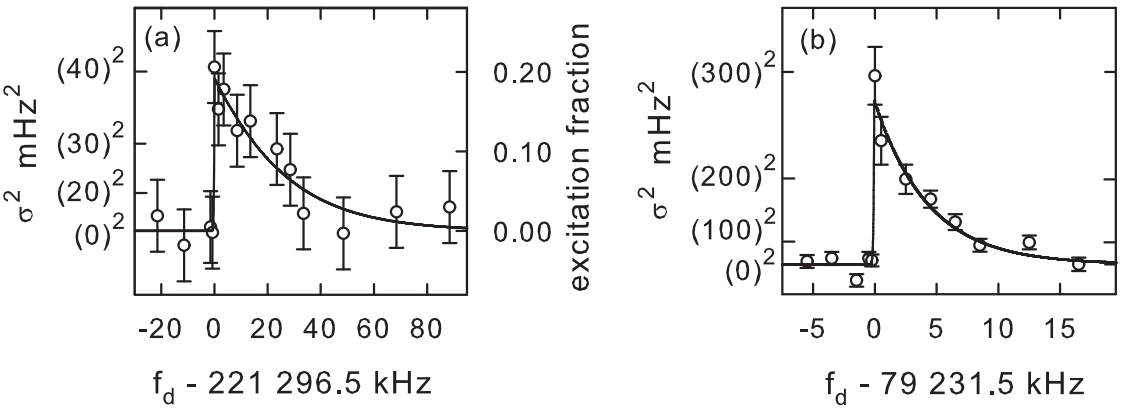

Figure 5.12: (a) The proton spin data. (b) The proton cyclotron data.

The magnetic moment result comes from the ratio of the spin and cyclotron frequencies extracted from the line shapes. Figure 5.12 shows the spin and cyclotron data used for the measurement. The magnetic moment is determined by the ratio of the spin and cyclotron frequencies,

$$\frac{\mu_p}{\mu_N} = \frac{g}{2} = \frac{f_s}{f_c}. \tag{5.20}$$

The spin frequency is taken to be the center of the sharp leading edge of the data. The uncertainty in the spin frequency is set by the half-width of the step. For the cyclotron frequency, the Brown-Gabrielse invariance theorem is needed to extract the free space cyclotron frequency from the three eigenfrequencies of the imperfect trap. Using measurements of the trap modified cyclotron frequency along with the axial and magnetron frequencies we obtain the cyclotron frequency

$$f_c = \sqrt{f_+^2 + f_z^2 + f_-^2}. \tag{5.21}$$

Table 5.1: Uncertainties for the proton magnetic moment measurement.

Resonance	Source	ppm
spin	resonance frequency	1.7
spin	magnetron broadening	0.7
cyclotron	resonance frequency	1.6
cyclotron	magnetron broadening	0.7
total		2.5

At the current precision, the uncertainty of the cyclotron data is dominated by the half-width of the step size in the cyclotron data. Uncertainties from the axial and magnetron frequencies contribute well below the ppm level. Table 5.1 lists the known uncertainties in the measurement. The resonance frequency uncertainty is given by the half-width of the leading edge to the data. The magnetron broadening is taken to be the linewidth from the magnetron Boltzmann distribution in the bottle field.

Chapter 6

Antiproton Magnetic Moment Measurement

For the antiproton magnetic moment measurement, it was necessary to modify the apparatus (to accept antiprotons) and move the experiment to CERN in Geneva, Switzerland. The Antiproton Decelerator (AD) at CERN is currently the sole world-wide source of low energy antiprotons. While the antiprotons at the AD are considered low energy from a particle physics perspective, the 5 MeV beam is still 10 orders of magnitude higher in energy than the 4 K antiproton used for the magnetic moment measurement. The methods developed by our group to slow, capture, cool and isolate a single antiproton [69] are well known and used for the antihydrogen experiments at CERN. Nevertheless, a substantial effort was needed to realize a single 4 K antiproton in our apparatus.

6.1 Loading Antiprotons

6.1.1 Detecting Antiprotons

The process of loading a single antiproton is greatly aided by the annihilation detection of small numbers of antiprotons. This sensitivity is crucial for the magnetic moment measurement because of the small electrode size of the trap. This is the smallest trap used to catch and hold antiprotons. As a result, detection of 10-100 antiprotons was required for the initial catching and trapping.

Annihilation detection is accomplished using scintillating paddles that surround the experiment magnet (see Fig. 6.1). A signal is generated when an antiproton annihilates, releasing charged pions with energies up to a few hundred MeV, that can then pass through the scintillating paddles. The charged pions give rise to scintillation light in the paddles that is detected using photo-multiplier tubes. The solid angle of the scintillating paddles and the multiple pions per annihilation together yield a detection efficiency of approximately 50 percent [70].

6.1.2 Energy Tuning and High Voltage Catching

The antiprotons are cooled to 4 K in stages, we first slow the beam from the initial 5.3 MeV to the keV range. Slowing in this stage is provided by a gas cell containing a mixture of SF_6 and helium, followed primarily by a 100 μm thick beryllium foil degrader. The gas cell allows for in situ energy tuning as the relative concentration of the gases determines the antiproton energy loss through the cell. Details of the cell dimensions and thicknesses are reported in reference [71]. The energy tuning range of

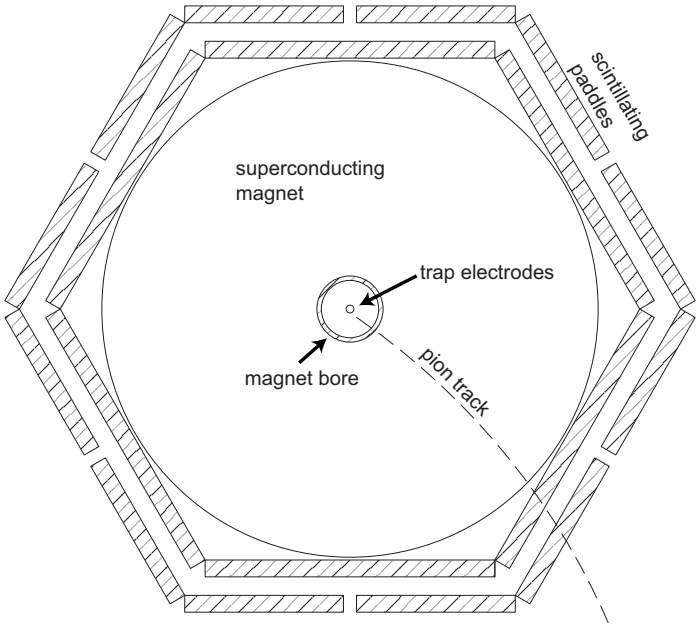

Figure 6.1: The annihilation detector schematic.

the cell is approximately 0.5 MeV. Using a computer code entitled Stopping and Range of Ions in Matter (SRIM) [72] to estimate the antiproton deceleration in the energy tuning cell, subsequent aluminized mylar layers and beryllium degrader, we chose an appropriate thickness of mylar to position the optimum cell tuning at approximately an equal mixture of He and SF_6 gas. Figure 6.2 shows the experimental results from catching antiprotons at different gas concentrations. The peak in the number of antiprotons caught corresponds well with the expected SF_6 fraction.

The antiprotons emerge from the degrader with energies in the keV range, low enough for high voltage (HV) catching. Using a turning potential of -300 V on T3, the antiprotons with less than 300 eV of energy are reflected back to the degrader (see Fig. 2.5). The HV trap is completed when the degrader is switched to -300 V before the antiprotons return. Using T3, the transit time is roughly 500 ns for 300 eV

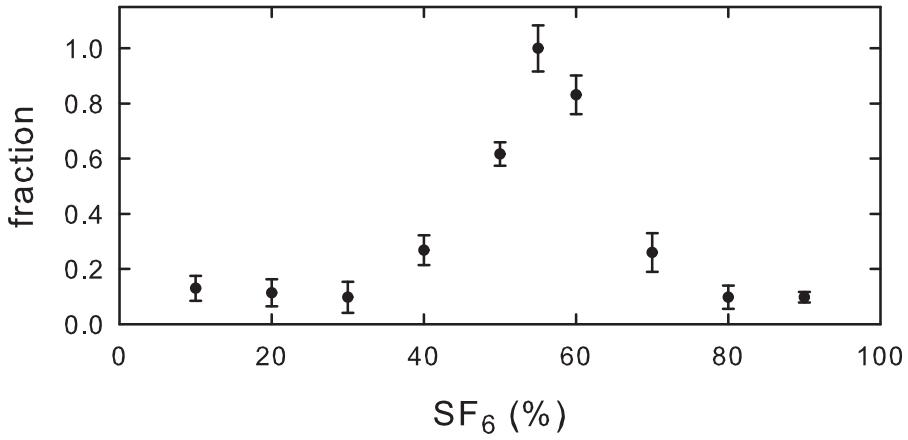

Figure 6.2: The fraction of antiprotons caught as a function of SF_6 precentage.

antiprotons. After the degrader voltage is quickly lowered, antiprotons with energies less than 300 eV are held in the trap.

The degrader voltage timing is referenced to a trigger from the AD, signaling the ejection of antiprotons from the ring to our experiment. After a fixed delay time of typically 4.4 μs, the antiprotons enter the trap. If the degrader voltage is switched before the antiprotons enter the trap, the antiprotons leaving the degrader will gain enough energy to pass through the turning potential. If the degrader voltage is switched after the antiprotons enter the trap, there is a clear signal of antiprotons held in the trap. However, if the voltage is switched after 5 μs, the higher energy antiprotons start to reach the degrader before the trap is established. This leads to decreased trapping efficiency at longer delay times (see Fig. 6.3). The high voltage switch used for the degrader is the same as developed for early antihydrogen experiments, described in detail in reference [73], though the voltage applied was ten times

lower here.

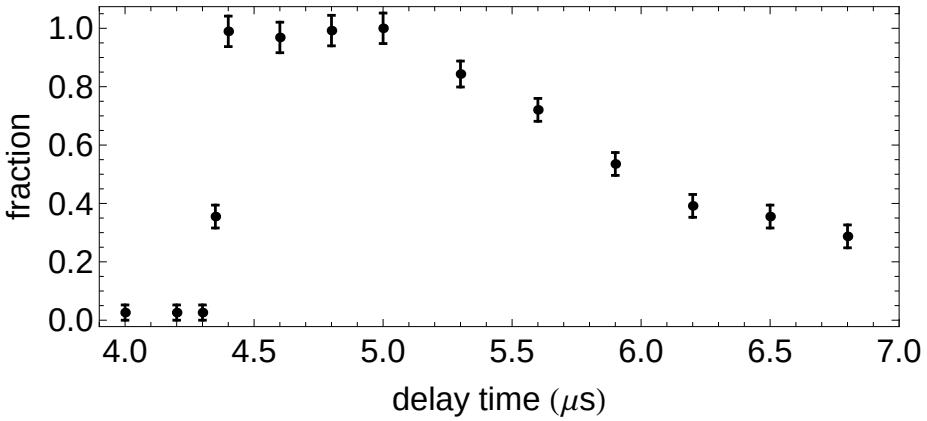

Figure 6.3: The fraction of antiprotons caught as a function of delay time from the CERN trigger.

The number of trapped antiprotons is limited by the cyclotron radius of the incoming antiprotons as they enter the magnetic field of our experiment. While the axial energy is decreased in the energy tuning cell and degrader, the cyclotron energy can be higher due to misalignment and also scattering in the cooling stages that converts some of the kinetic energy of the beam into radial energy. The trap radius sets an upper limit on cyclotron radius and therefore cyclotron energy. In Figure 6.4, we see a linear increase of trapped antiprotons up to 300 V, above which there is no gain with increased voltage. This behavior is consistent with earlier antihydrogen work from our group using trap electrodes with a 12 mm diameter trap, in comparison to the 6 mm diameter we currently use [39, 74].

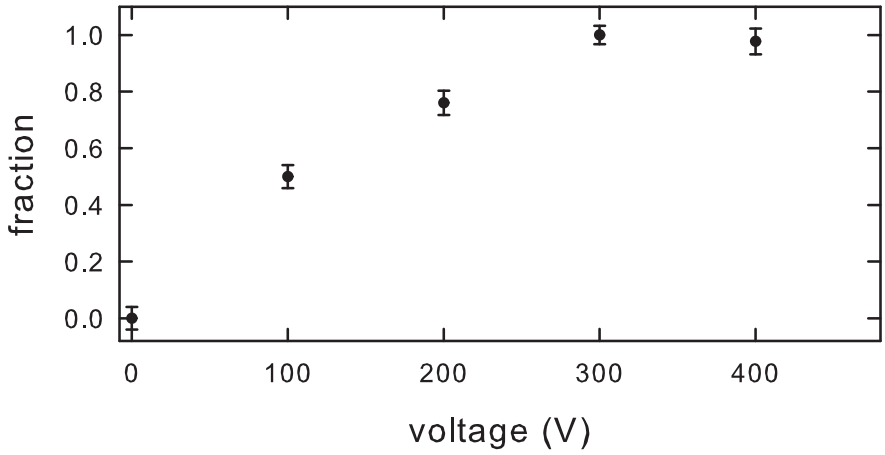

Figure 6.4: The fraction of antiprotons caught as a function of turning voltage.

6.2 Electron Cooling

The HV antiprotons are further cooled using collisions with co-trapped electrons [39, 74]. The synchrotron radiative cooling of the electrons in the ∼6 Tesla magnetic field provides a cooling mechanism with a timescale of 0.1 sec for the electron cyclotron motion. Collisions between the antiprotons and the electron cloud removes the remaining energy from the antiprotons.

6.2.1 Spherical Approximation, Plasma Density and Size

While a more detailed description of electrons in Penning traps can be undertaken [75, 76], for electron cooling in the antiproton magnetic moment experiment, understanding of the basic electron cloud properties can be gained using a spherical approximation [77]. This provides a basic framework for the cloud parameters and

scalings, giving a foundation for the experimental implementation of electron cooling.

The properties of an electron plasma can be approximated by assuming the electron cloud is spherical with radius r and uniform density n_e. The size of the cloud can be determined by equating the axial restoring force from the externally applied electric quadrupole potential and the internal repulsive force exerted by the electron cloud. Equating these forces is easiest along the z-axis at $\rho = 0$, giving

$$n_e = \frac{3\epsilon_0 C_2 V_0}{ed^2} \,. \tag{6.1}$$

Where C_2, V_0, and d are respectively the trap coefficient, voltage and length scale, introduced in Sec. 2.1.1. It is important to note that the units for this expression and those that follow are SI. The typical trapping potential for electrons is 20 V, used to bring the electron axial frequency into resonance with the cyclotron amplifier at roughly 86.5 MHz. At this voltage, the electron densities are in the 10^8 cm^{-3} range.

Using the electron density, the radius of the cloud can be extracted as a function of the total number of electrons in the plasma. Again employing the spherical approximation, we obtain

$$r = \left(\frac{3N_e}{4\pi n_e}\right)^{1/3} \,. \tag{6.2}$$

Where N_e is the total number of electrons and n_e is the electron density. For a 20 V potential, the radius is 0.5 mm for 100k electrons and 0.1 mm for 1k electrons. For a 1 V potential, the radius is 1.3 mm for 100k electrons and 0.3 mm for 1k electrons. The 1 V potential is relevant because it is used for pulsing out the electrons, discussed further in Sec. 6.2.3.

6.2.2 Electron Cooling Theory

The principle underlying electron cooling antiprotons is that the co-trapped electrons collisionally equilibrate with the antiproton cloud, while also emitting synchrotron radiation to equilibrate with the temperature of the bath, T_b, the temperature of radiation at the electron cyclotron frequency in the trapcan. This leads to two coupled rate equations for the electron and antiproton temperatures [78]

$$\frac{d}{dt}T_{\bar{p}} = -\frac{1}{\tau_{eq}}(T_{\bar{p}} - T_e) \ , \tag{6.3}$$

$$\frac{d}{dt}T_e = \frac{N_{\bar{p}}}{N_e}\frac{1}{\tau_{eq}}(T_{\bar{p}} - T_e) - \frac{1}{\tau_c}(T_e - T_b) \ . \tag{6.4}$$

In these equations, the temperature and number of the antiprotons and electrons are respectively $T_{\bar{p}}$, $N_{\bar{p}}$, T_e, and N_e. The timescales for the equilibration between the electrons and antiprotons and the synchrotron radiation of the electrons are τ_{eq} and τ_c. The synchrotron radiation timescale is approximately $\tau_c \approx 0.1$ sec in a magnetic field of $\sim$6 Tesla. The expression for τ_{eq}, is more involved and is discussed in more detail along with the Λ factor in references [79, 80]

$$\tau_{eq} = \frac{3m_{\bar{p}}m_e(4\pi\epsilon_0)^2}{8\sqrt{2\pi}n_e e^4 \ln\Lambda}\left(\frac{k_B T_{\bar{p}}}{m_{\bar{p}}} + \frac{k_B T_e}{m_e}\right)^{3/2} \ . \tag{6.5}$$

Two main features to note are that both the electron number and density determine the cooling rate. Fixing the number of antiprotons, as is experimentally realized given an idealized AD shot, increasing the number of electrons increases the antiproton cooling rate. In addition, increasing the density of the electrons decreases the equilibration time between the antiprotons and electrons. The experimental results of these implications can be seen in Fig. 6.5. Where the number of antiprotons leaving the high voltage well are counted as a function of time. Furthermore, the number

of higher energy antiprotons decreases faster when there are more electrons. Similar behavior can be seen with higher voltages, which create higher densities. Earlier work by our group has been done in connection to loading many more antiprotons for antihydrogen work, reported in reference [74].

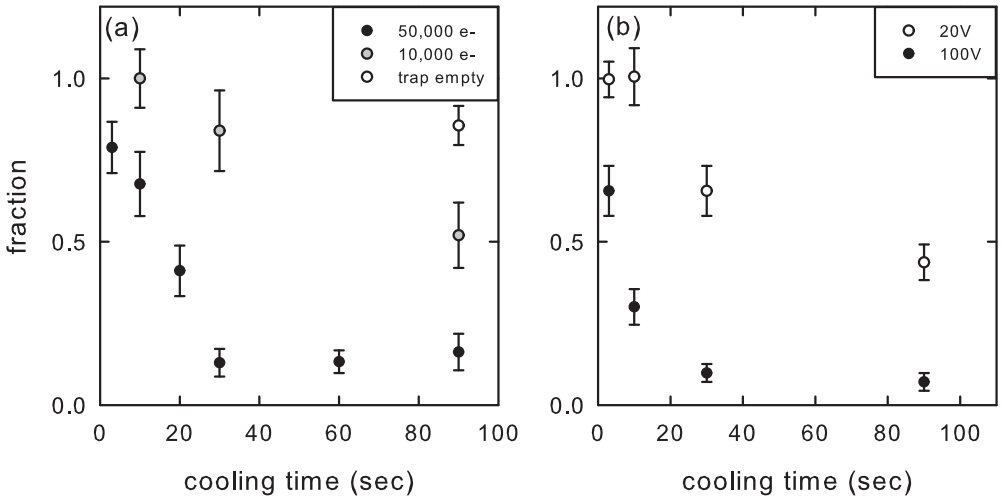

Figure 6.5: Fraction of antiprotons leaving the HV catching well as a function of time after electron cooling with (a) different numbers of electrons in the same trapping potential and (b) the same number of electrons in different in trapping potentials.

6.2.3 Experimental Implementation of Electron Cooling

The electrons used to cool the antiprotons are loaded from the antiproton beam itself. Using the appropriate degrader voltage timing, a 4.4 μs delay, the antiproton beam loads a substantial number of electrons as electrons are released from the degrader while antiprotons pass through it. These electrons are caught in the same HV well as the antiprotons and cool the antiprotons from the initial energy ($\sim$300 eV) to

a approximately 4 K ($\sim$ 0.3 meV).

The result of loading antiprotons with electrons is shown in Figure 6.6. The plots are generated by monitoring the annihilation counts of the detectors as the HV well is dumped by a linear ramp of the degrader voltage from -300 V to +150 V in 300 ms. For the initial cooling times of ten and twenty seconds, the antiproton energy distribution is largely unchanged. However, for 40 seconds, there is a clear low energy peak. After eighty seconds, the initial antiproton cloud is almost entirely in the low energy bins, indicating nearly complete thermalization. Using the integral of the detector signal, we can monitor antiproton loss during the cooling. Figure 6.7 illustrates no appreciable loss over the cooling time.

Only a few antiprotons are needed for the magnetic moment measurement. As a result, the antiproton loading well for electron cooling differs from previous work. In the past, long HV wells have been used [39]. We currently use a three electrode configuration for loading. The HV well consists of T5, the extension electrode and the degrader (see Fig. 2.5 and Fig. 2.9). The degrader is initially held at +200 V as the antiprotons enter the trap. The turning electrode, T5, is held at -300 V, and the trapping electrode, the extension electrode, is held at +100V. Using a 4.4 μs delay time, the degrader is switched to -300 V. This traps both electrons and antiprotons in the well. The round trip transit time for this shorter well is around 100 ns for 300 eV antiprotons. After 80 seconds of cooling the antiprotons and electrons are adiabatically transferred to the precision trap.

After cooling the antiprotons, the electrons are no longer needed and the next step is to eject them from the trap without losing the antiprotons [39]. To do so, the

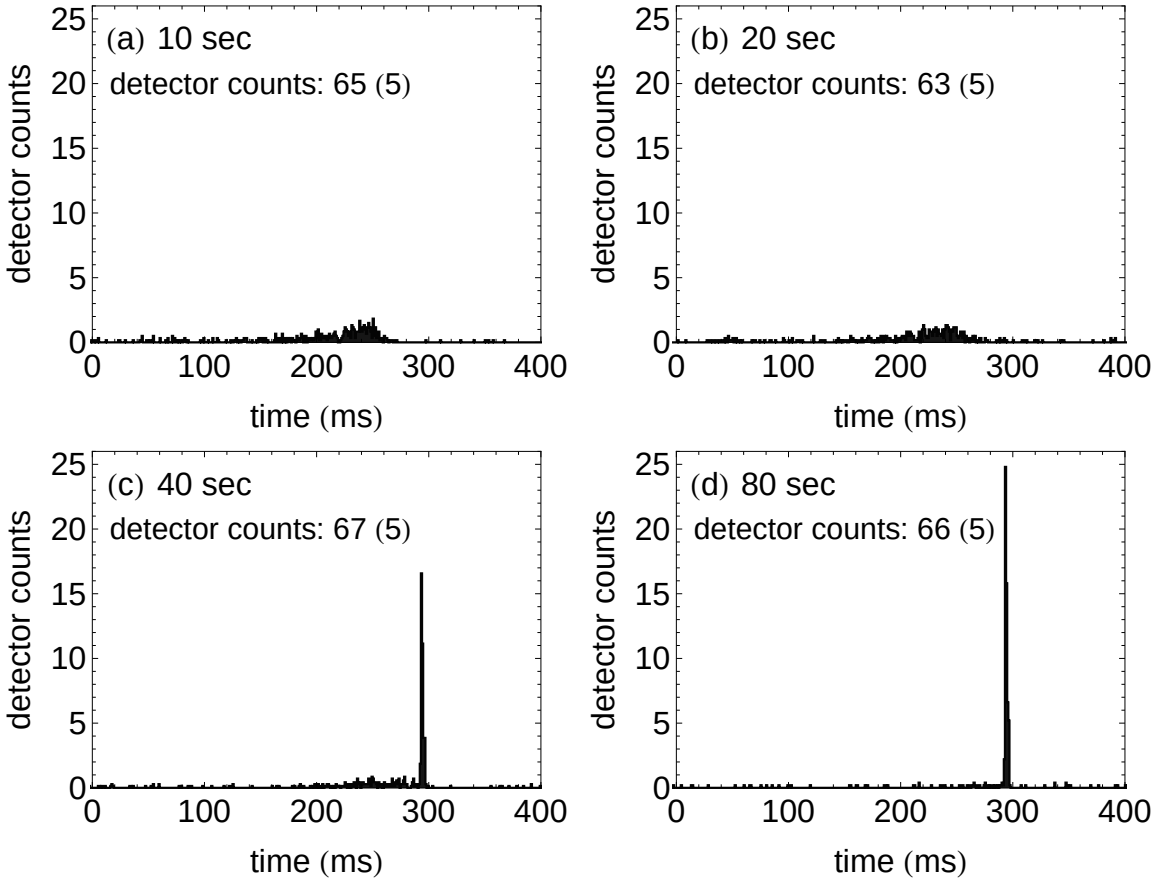

Figure 6.6: The detector signals from dumping the trap as a function of cooling time. There is a clear indication of electron cooling for the 40 sec and 80 sec cooling times. The large number of counts in a narrow window at 300 ms indicates a substantial number of antiprotons at low energies with a small energy spread, indicative of electron cooling.

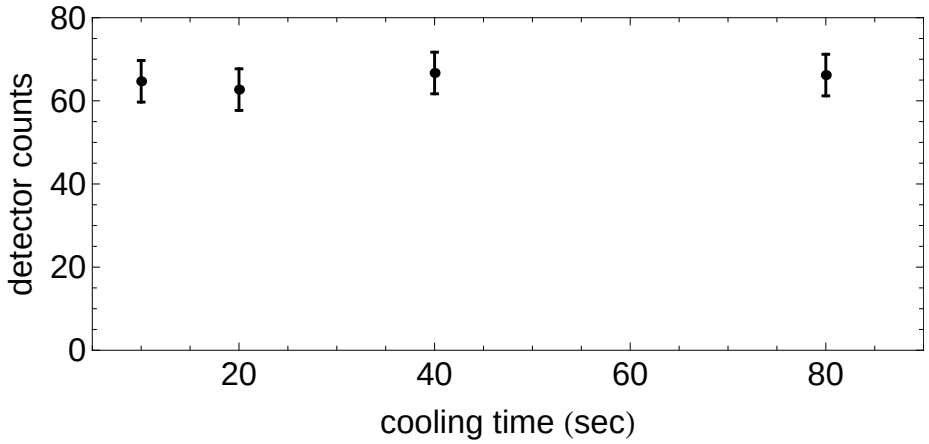

Figure 6.7: The integral of the detector counts in Fig. 6.6 as a function of cooling time. There is no sign of antiproton loss during the electron cooling process.

trapping potential is dipped to 1 V. At this trap potential, the electrons are pulsed out using a DG535 driven saturated switch (Avtech AV-144B1) to briefly lower the trap potential further. The pulse duration is 100 ns - a time short enough so that the heavier antiprotons cannot escape, while long enough to allow the less massive electrons to leave. To ensure there are no remaining electrons, the pulse is repeated ten times and the electron response is monitored both at low and high voltages discussed in more detail in Sec. 3.4. The amplitude of the pulse is roughly 10 V at the hat, which is subsequently attenuated in the twisted pair as well as at the capacitive divider at the pinbase. The pulse is applied to the endcap axial drive line. In addition, we establish a sloping the well to the degrader using 20 V, 40 V, and 80 V on T5, the extension and the degrader respectively, so that the electrons are guided away from the trapping region.

6.3 Magnetic Field Stability

The magnetic moment measurement relies on low magnetic field noise. To evaluate the magnetic field noise in the AD, we used antiproton cyclotron decays (see Sec. 3.3.2). The largest magnetic field shift we observed comes from the large, 50-ton crane. This crane is used by the different groups to bring in cryogens, large shipments, perform experiment installations and maintenance. Figure 6.8 shows the effect of the crane on the cyclotron decay. When the crane is directly overhead, the trap modified cyclotron frequency decreases by about 30 Hz or 0.35 ppm.

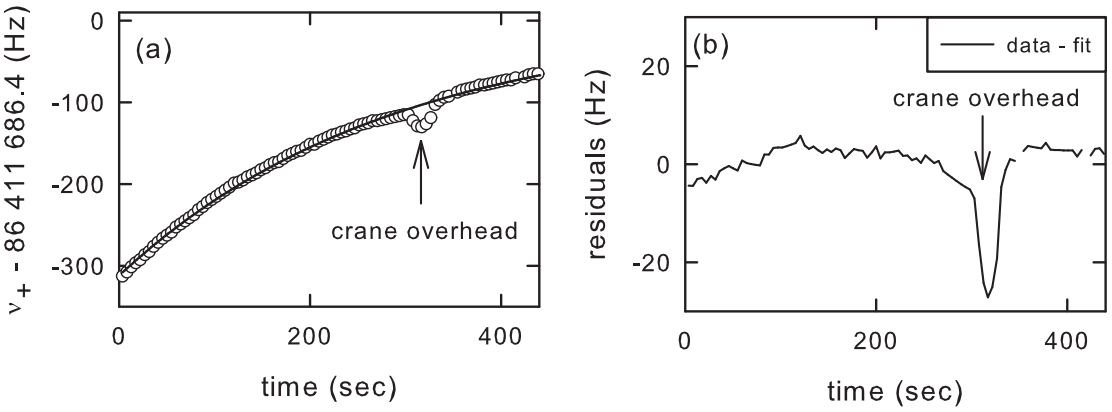

Figure 6.8: (a) An antiproton cyclotron decay when the crane moves overhead. (b) Residuals show a 30 Hz or 0.35 ppm shift when the crane is overhead.

As mentioned before, another source of magnetic field noise is the cycling magnets in the AD ring itself. The effect of the AD cycle on a cyclotron decay is clear in Fig. 6.9. This changes the cyclotron frequency by approximately 3 Hz or 35 ppb. While this is currently well below the measurement precision, it will be important to address in the next generation experiment. In the current trap configuration, the

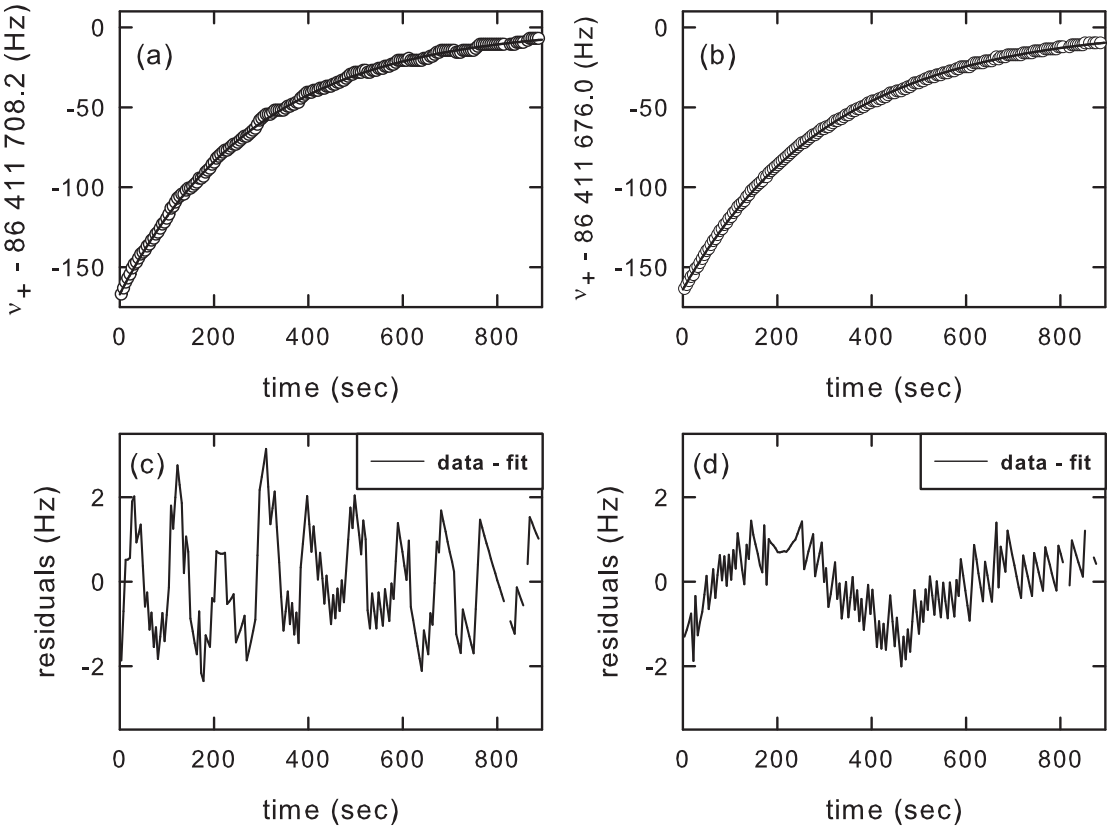

Figure 6.9: (a) An antiproton cyclotron decay with the AD cycle on. (b) A similar decay when the AD cycle is off. (c) Residuals with the AD on, the oscillation amplitude of 3 Hz in cyclotron frequency represent a shift of 35 ppb in magnetic field. (d) Residuals with AD off, show some improvement, but there is clearly still background magnetic field noise.

precision trap is below magnetic field center, to allow antiproton loading directly into this larger diameter trap. This avoids the constriction of the smaller analysis trap and the possible complication of the bottle field for loading antiprotons. The off-center precision trap lowers the amount of magnetic shielding from the self-shielding solenoid design [81, 82]. The shielding factor measured by comparing the field shift with the cyclotron decay to an external magnetometer indicate a factor of 10 reduction in magnetic field shift. In the same magnet, with the trap on field center, the shielding factor was previously measured to be 150 [35]. Future improvements in the magnetic field stability could be achieved by having the precision trap on field center.

6.4 Axial Frequency Stability

The magnetic moment measurement relies on resolving the small axial frequency shift from a spin flip, roughly 130 mHz out of the approximately 1 MHz axial frequency. This small shift sets a requirement on the axial frequency stability for resolving spin flips. Stability of the axial frequency at the 100 mHz level, roughly 100 ppb, translates to a required voltage stability of better than 0.5 μV. There were also concerns about the RF noise spectrum in the AD obscuring the relatively small signal from a single antiproton, diminishing the signal-to-noise of the axial frequency detection. This noise spectrum could also drive unwanted cyclotron or magnetron transitions, potentially limiting the axial frequency stability.

The main feature of the axial frequency stability at CERN was that it was sufficient for seeing spin flips and cyclotron jumps. Figure 6.10 show the typical SEO and dip signal for an antiproton at CERN. The signals themselves are quite similar to those

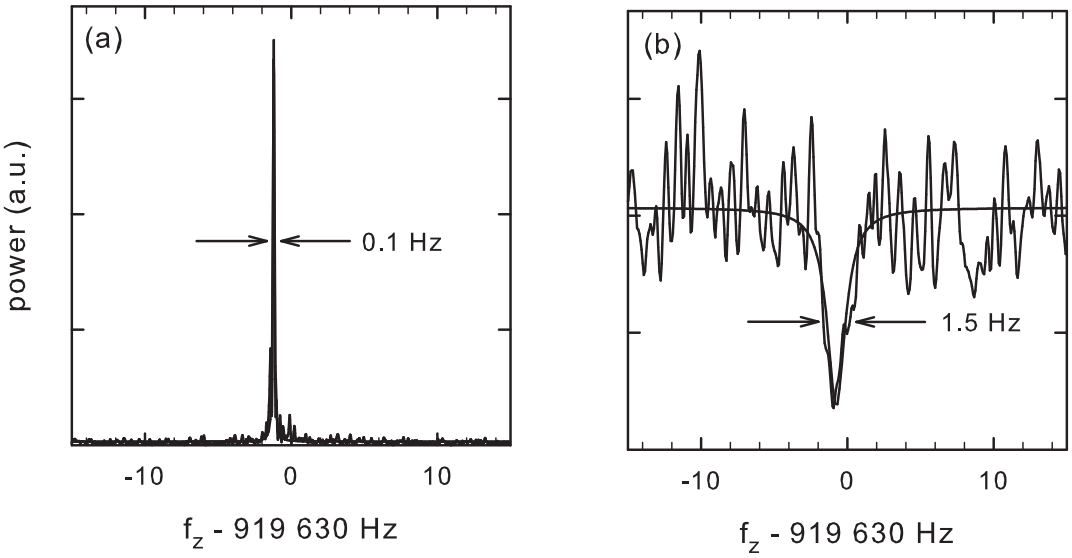

Figure 6.10: (a) The signal from an single particle antiproton self-excited oscillator. (b) The axial dip of a single antiproton dip.

at Harvard, encouraging us that the noise at CERN is not substantially detrimental. In fact, on some occasions, the stability was similar to the best stability seen at Harvard. However, good stability was not as consistent at CERN. This may be due to a changing noise background not under our control. Figure 6.11 shows data from two consecutive days at CERN. The frequency data is taken using a single 8 second averaging time.

The plots on the right show the Allan deviation at different averaging times, computed using the axial frequency data and averaging different numbers of data points together. The Allan deviation at an averaging time of 32 seconds is 54 (5) mHz and 81 (7) mHz. While this increase and repeatability will be important to address for the ppb antiproton measurement, both the stability and consistency was

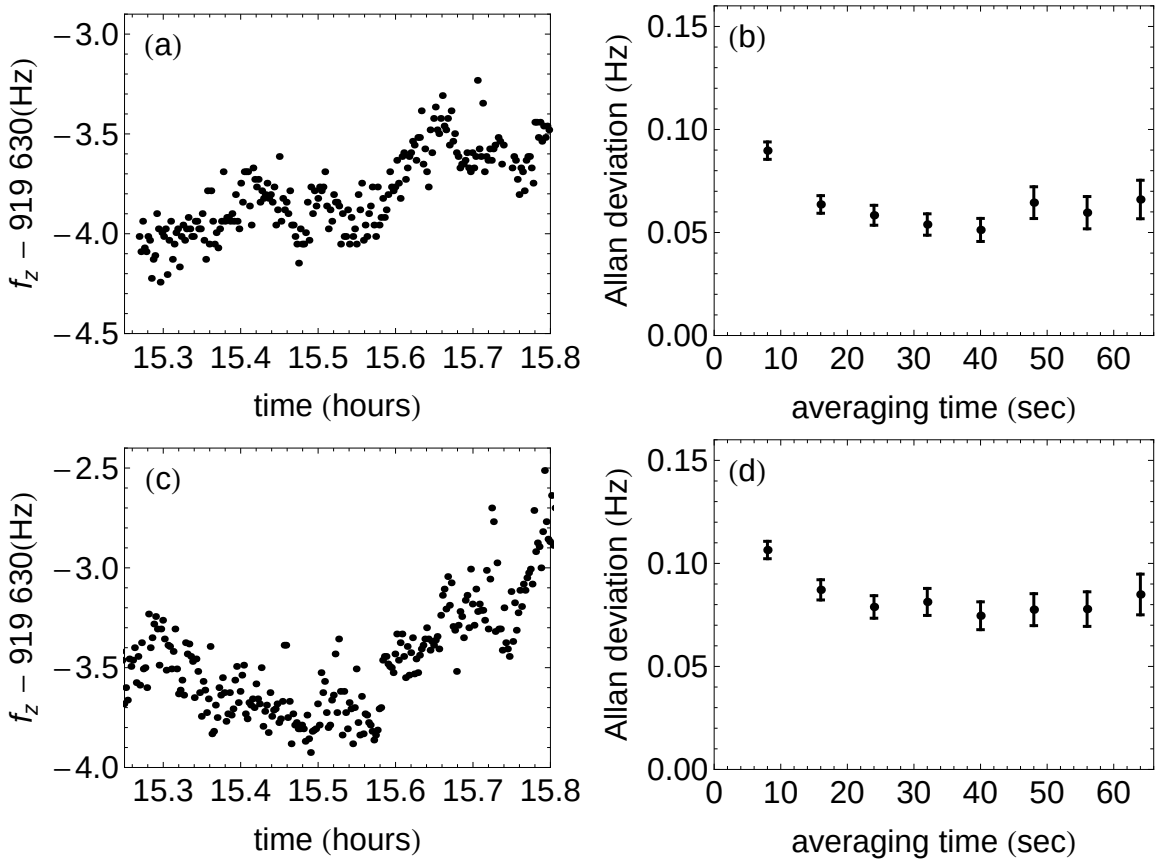

Figure 6.11: (a) and (c) show the axial frequency measurements using the self-excited oscillator with an 8 second averaging time on consecutive days. (b) and (d) show Allan deviation as a function of averaging time extracted from this data. The Allan deviation in (d) is elevated compared to (b), at 32 seconds the respective deviations are 81 (7) mHz and 54 (5) mHz. While this difference is currently unexplained, the overall level and consistency are sufficient for the ppm magnetic moment measurement.

sufficient for a ppm magnetic moment measurement.

6.4.1 Temperature Stability in the AD

In the process of obtaining sufficient axial frequency stability, we identified a large contributor to axial frequency shifts at the AD. The source was the primitive temperature regulation of the Faraday cage holding the electronics. The binary temperature lock caused substantial changes in the axial frequency shifts. The air conditioner was either on or off, when it was off a fan circulated the air. We found a large change in axial frequency when the air condition was on. The first pass solution to this was

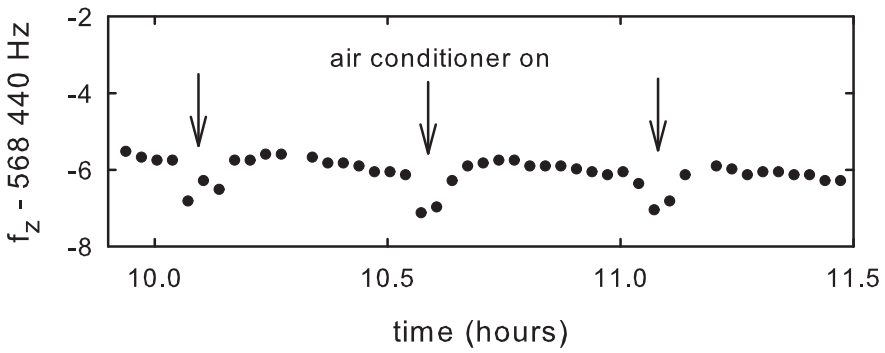

Figure 6.12: The axial frequency in the precision trap shows a clear shift when the air conditioner is turned on.

to only use the fan, but this suggests that better temperature regulation may further increase the axial frequency stability.

6.4.2 Noise in the AD

Another potential issue in the AD is noise from other experiments in close proximity. This may explain why the axial frequency stability is less consistent at CERN. An example of such a changing noise spectrum can be seen in the axial noise resonance amplitude. Figure 6.13 shows an example of such a background noise change. When the AEGIS experiment has patrolled their zone, as seen in Fig. 6.13(a), the noise level is substantially elevated. This can be compared to the typical background noise level when the AEGIS zone is open in Fig. 6.13(b). The cause of this difference is

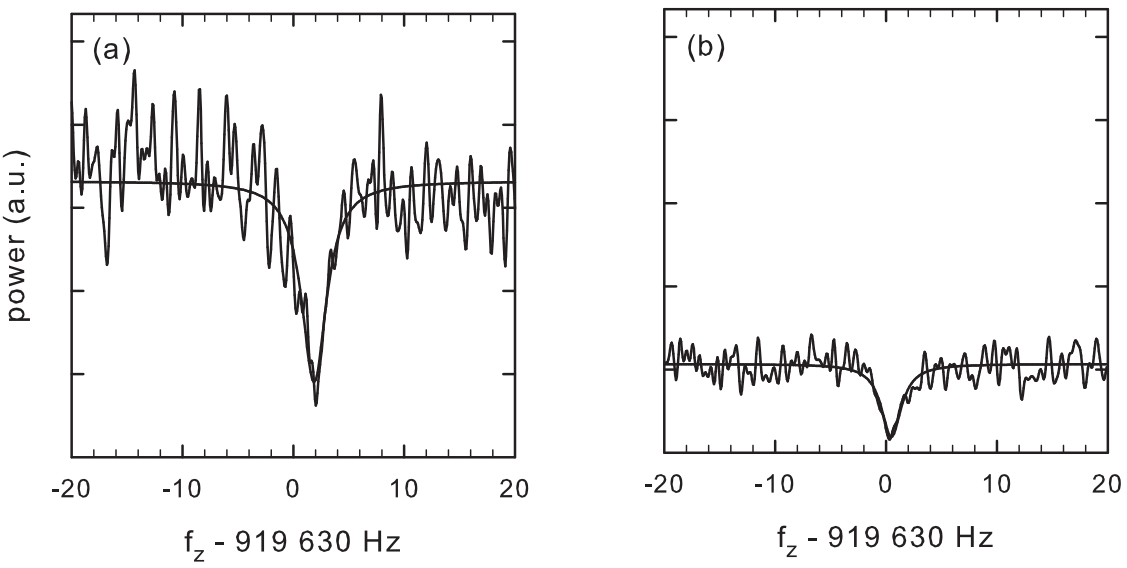

Figure 6.13: The changing noise level in the AD detected using the axial amplifier.

not currently known. In the future, it will be interesting to perform a more detailed investigation of the noise in the AD hall and its implications for the axial frequency stability.

6.5 Drive Strength Systematic

As with the proton magnetic moment measurement, we measured the drive systematic caused by the strong spin flip drive that shifts the axial frequency. In particular, we needed to measure the drive strength systematic using the transmission line transformer (see Sec. 3.6 and Fig. 2.6) that had been added after the proton measurement. This transmission line transformer is important because it allows us to saturate the spin transition, while it also decreases the drive strength systematic. Through the invariance theorem [40], a shift in the axial frequency changes the cyclotron frequency. If the axial frequency shift is large enough, it would impact the magnetic moment measurement because the spin frequency would be measured at an effectively different cyclotron frequency. Given the observed shift illustrated in Figure 6.14, the shift in cyclotron frequency is at the ppb level, far below the current precision.

6.6 Magnetic Moment Measurement

We can now report the first measurement of the antiproton magnetic moment using a single particle [2]. The result is a 4.4 ppm measurement expressed in terms of nuclear magnetons, μ_N,

$$\frac{\mu_{\bar{p}}}{\mu_N} \equiv \frac{g_{\bar{p}}}{2}\frac{q_{\bar{p}}/m_{\bar{p}}}{q_p/m_p} \approx -\frac{g_{\bar{p}}}{2} = -2.792\,845\,(12)\ [4.4\ \text{ppm}]. \tag{6.6}$$

The approximation comes from the ratio of the proton and antiproton charge to mass ratios. This is currently measured to better than 1 part is 10^{10} [35], so it does not contribute uncertainty at the ppm precision.

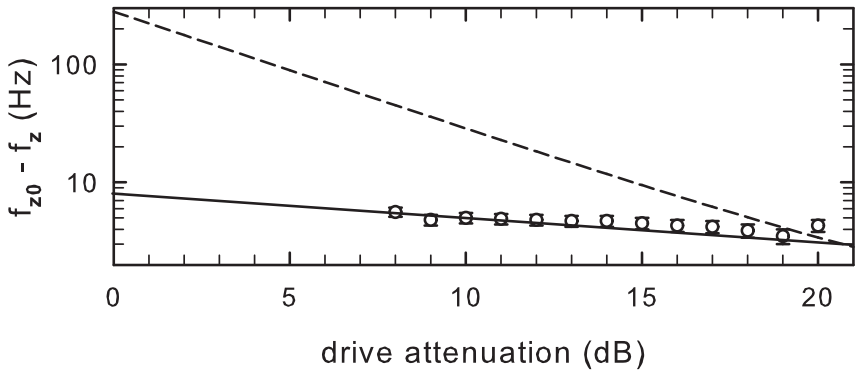

Figure 6.14: The axial frequency shift as a function of spin flip drive strength using the transmission line transformer and an antiproton. The fit to the proton data is shown by the dashed line, taken before the installation of the transmission line transformer. This shift corresponds to an uncertainty in at the ppb level, well below the measurement uncertainty.

The antiproton measurement is made using the same methods as the proton measurement. The spin and cyclotron frequencies are measured in the analysis trap using a time-averaged signal from spin flips and cyclotron jumps. The axial frequency stability is used to measure the frequencies. An increase in the Allan deviation indicates a resonant drive. This axial frequency stability is measured at different drive frequencies, sweeping out the spin and cyclotron resonance line shapes, which are shown in Fig. 6.15.

The spin frequency line shape relies on the SEO for axial frequency measurement. The high signal-to-noise of the SEO enables precise measurement of the axial frequency in the 24 seconds used in the measurement. With a resonant spin drive, we can at most cause a transition half of the time, leading to a relatively strict requirement on the axial frequency stability needed to resolve spin flips. The improved

matching network on the spin drive line allowed us to increase the excitation fraction to 0.5. This was important for making the measurement given the added time constraint of the beam run. The spin data is shown in Figure 6.15(a). Each point represents 24-48 hours of data, giving a total time of three weeks.

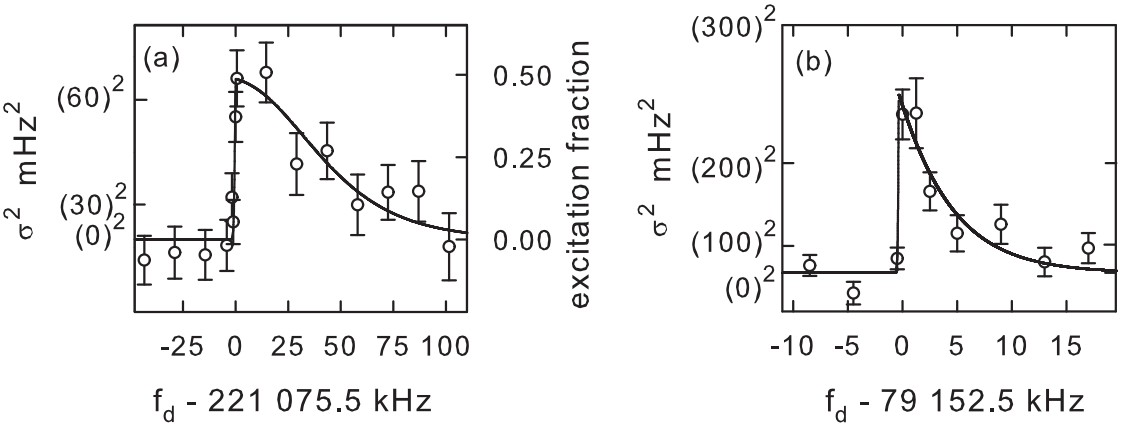

Figure 6.15: (a) The antiproton spin data. (b) The antiproton cyclotron data.

For the cyclotron frequency measurement, the strict requirement on the axial frequency stability is lowered because we are able to drive multiple cyclotron transitions. As a result, we use axial dips for the frequency measurement. However, there is another constraint, it is important to just barely drive the cyclotron motion to make sure the cyclotron radius does not increase. To ensure the radius does not change, a very weak drive is applied continuously to a split compensation electrode. While the drive is applied, axial frequency dips are measured, and as with the spin measurement, the Allan deviation of the dips determines whether the drive is resonant. The cyclotron data is shown in Fig. 6.15(b). Compared to the spin measurement, the cyclotron measurement is substantially aided by the ability to drive multiple cyclotron transitions.

The data for a resonant drive corresponds to roughly 8 cyclotron transitions between adjacent axial frequency measurements, corresponding to a frequency difference of roughly 400 mHz. The cyclotron data is taken for 2-4 hours at each point, giving a total time of 1.5 days.

Table 6.1: Uncertainties for the antiproton magnetic moment measurement.

Resonance	Source	ppm
spin	resonance frequency	2.7
spin	magnetron broadening	1.3
cyclotron	resonance frequency	3.2
cyclotron	magnetron broadening	0.7
total		4.4

The measurement uncertainties are similar to the proton measurement. The resonance frequency uncertainty is taken to be the half-width of the sharp leading edge of the data. These uncertainties are larger for the antiproton measurement because larger frequency steps were taken, given more time, it should be possible to take finer steps. The magnetron broadening is due to the radial distribution caused by sideband cooling the magnetron motion. The factor of two difference between the spin and cyclotron magnetron broadening comes from the use of feedback cooling when sideband cooling for the cyclotron data and not during the spin data.

Chapter 7

Single Spin Flip Detection

We made the proton and antiproton magnetic moment measurements using a time-averaged method to resolve spin flips [1, 2]. A precision beyond the ppm level will rely upon using quantum jump spectroscopy in the precision trap [54, 83]. This requires resolving individual spin flips, as opposed to the time-averaged signal. We now report the first observation of single spin flips with a proton [3]. A similar result was simultaneously reported by Mooser and colleagues [11].

The motivation for performing the magnetic moment measurement in the precision trap comes from the linewidth of the spin and cyclotron lines in the low magnetic gradient field of this trap. In the precision trap, where there is ideally no magnetic gradient, the linewidth of the transition should be below 10 ppb. As a result, a measurement made in the precision trap should be able to reach the ppb level. In contrast, the linewidth in the analysis trap is currently 100 ppm due to the large magnetic gradient from the iron ring.

7.1 Criteria for Single Spin Flip Detection

An important step to detecting single spin flips is achieving sufficient axial frequency stability to detect the tiny shift due to a spin flip. The Allan deviation, the rms difference between consecutive frequency measurements, quantifies the axial frequency stability. To first order, the expected condition for single spin flip detection is for the Allan deviation to be smaller than the spin flip size. To improve on this estimate, we will investigate the distributions more carefully.

For repeated axial frequency measurements we define Δ to be the difference between adjacent axial frequency measurements. With no spin flip drive we observe the background distribution of these differences to be Gaussian. Given the measured background Gaussian noise distribution $G(\Delta)$, normalized so $\int_{-\infty}^{\infty} G(\Delta)\,\mathrm{d}\Delta = 1$, and a spin flip probability, P, the expected probability density distribution for a sequence of spin flip drive applications is

$$s(\Delta) = (1-P)G(\Delta) + \frac{P}{2}G(\Delta+\Delta_s) + \frac{P}{2}G(\Delta-\Delta_s). \tag{7.1}$$

The first term represents the probability $(1-P)$ that the spin state will not change, and gives the axial frequency difference from the Gaussian distribution centered around zero. The next two terms are for the probability P that a spin flip is driven in between the adjacent axial frequency measurements. Half of the spin flips represent changes in spin state from up to down, in which case the axial frequency is selected from a Gaussian centered around $-\Delta_s$ (given by the second term in Eq. 7.1). The third term denotes the spin flips where the spin state changes from down to up. Using this distribution, it is possible to define the resolution criteria for a single spin flip.

In Sec. 7.2, we will also use this distribution to evaluate the fidelity of a spin flip assignment. For a resonant spin flip drive strong enough to saturate the spin transition, the probability that a drive will flip the spin is $P = 0.5$. In our first demonstration experiment, we operate in this limit, so the distributions will be shown for $P = 0.5$.

In Fig. 7.1, we see this distribution for two different background stabilities of the axial frequency. In red, the Gaussians are plotted for the spin flip transitions and in blue the background noise distribution is shown for the unsuccessful spin flip attempts. In black, the sum of the Gaussians represents the measured distribution of axial frequency differences. From this, it is clear that the contrast between a spin flip and a non flip increases as the width of the background noise decreases. This sets an estimate for identifying single spin flips. Roughly speaking, it is possible to distinguish spin flip events from background fluctuations when the half-width-half-maximum (HWHM) of the background is less than the size of the spin flip. While this is qualitatively correct and sets the approximate axial frequency stability needed to detect spin flips, an associated efficiency and fidelity better quantify the spin flip identifications (Sec. 7.2).

The definitions of the Allan deviation and the HWHM relate the two,

$$\text{HWHM} = 2\sqrt{\ln 2} \cdot (\text{Allan deviation}) < 130 \text{ mHz}. \tag{7.2}$$

The distributions in Fig. 7.1 illustrate HWHM = Δ_s=130 mHz and HWHM = $\Delta_s/2$= 65 mHz respectively. These are chosen because in our experiment the size of a spin flip is $\Delta_s = 130$ mHz. The Allan deviations of these Gaussians are respectively 78 mHz on the left and 39 mHz on the right.

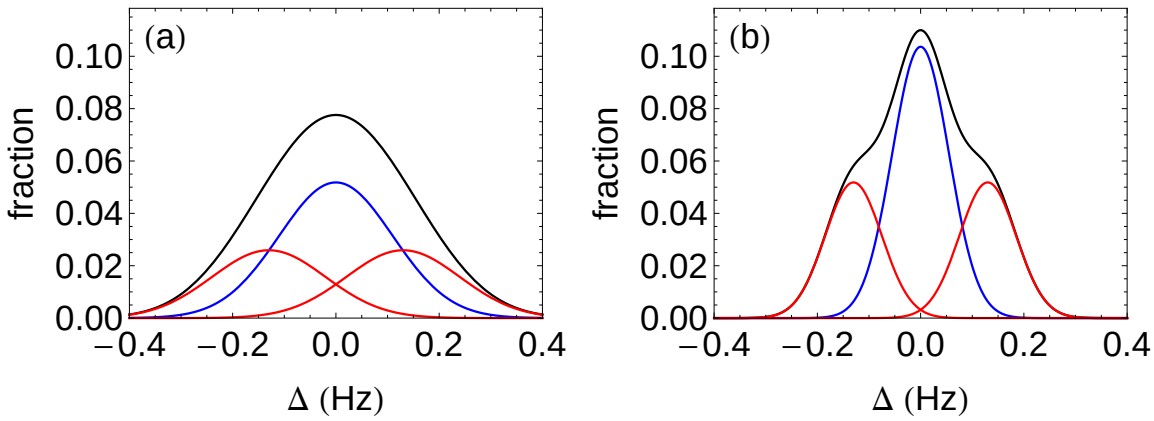

Figure 7.1: In red, the Gaussians are plotted for the spin flip transitions, in blue the background noise distribution is shown for the unsuccessful spin flip attempts, and in black, the sum of the Gaussians represents the expected distribution of axial frequency differences. On the left, the background Allan deviation is 78 mHz and on the right 39 mHz, corresponding to a HWHM of $\Delta_s = 130$ mHz and $\Delta_s/2 = 65$ mHz respectively.

7.1.1 Measured Frequency Shifts for the Single Spin Flip Measurement

The axial frequency measurements for the single spin flip measurement are taken with a similar sequence as was used for the magnetic moment measurements, Fig. 5.1. The only difference is that axial frequency integration times of 32 seconds were used instead of 24 seconds (because more time was invested to select a lower cyclotron state, which allowed a longer averaging time). Figure 7.2(a) shows the axial frequency measurements taken using the measurement sequence. Figure 7.2(b) shows the differences when a resonant saturated spin flip drive is applied and Figure 7.2(c) shows the differences for a control drive, detuned 50 kHz below resonance. While the overall drift during is not particularly low ($\sim$ 5 Hz over 12 hours, as illustrated in Fig. 7.2(a)) the Allan deviation of the axial frequency measurement for a far detuned

spin flip drive is 44 mHz. This translates to a HWHM of 74 mHz, satisfying the criterion of being substantially below the spin flip size of 130 mHz. As seen in Fig. 7.2, the differences for the resonant spin drive are clearly larger than for the off-resonant drive.

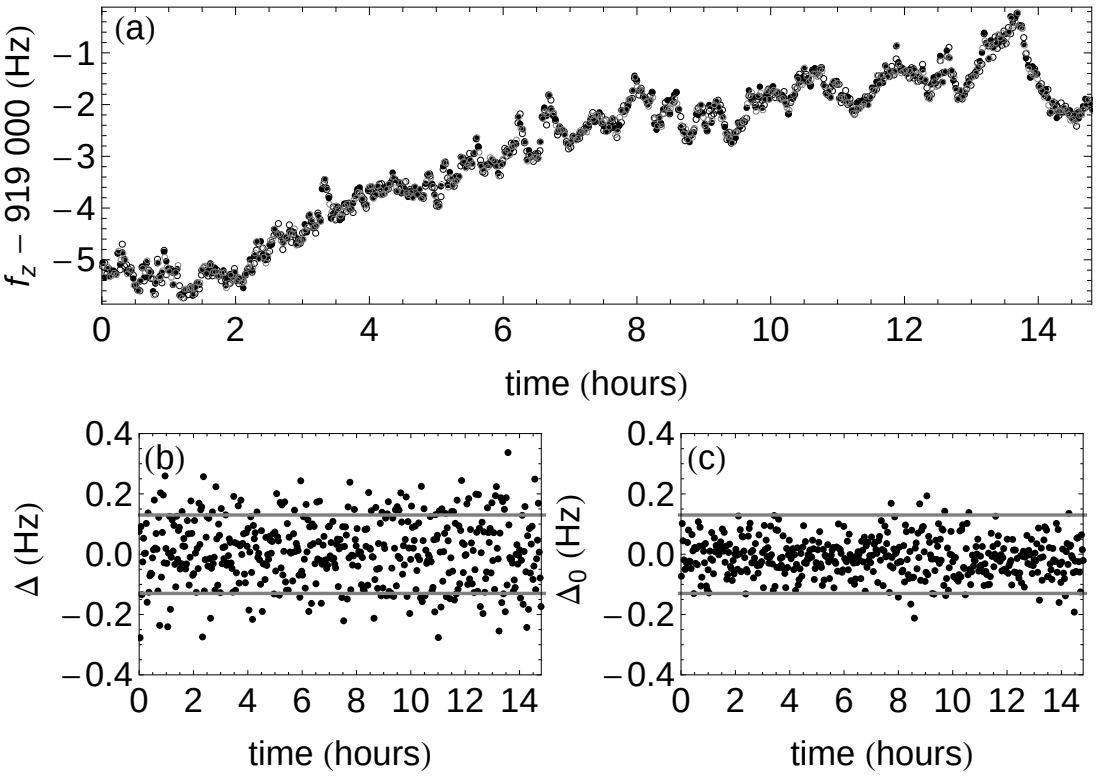

Figure 7.2: We repeat the measurement sequence several hundred times to measure the axial frequency differences. (a) shows the axial frequency measurements for the single spin flip data set. (b) and (c) show the axial frequency differences for the resonant and off-resonant spin-flip drive respectively.

The histograms of the differences are shown in Fig. 7.3. The differences for the off-resonant drive are shown in gray and for the resonant spin flip drive are shown in outline. The dashed line shows a Gaussian fit to the control data and the solid line represents the prediction for a saturated spin flip drive and the measured the Allan

deviation for the Gaussian distribution.

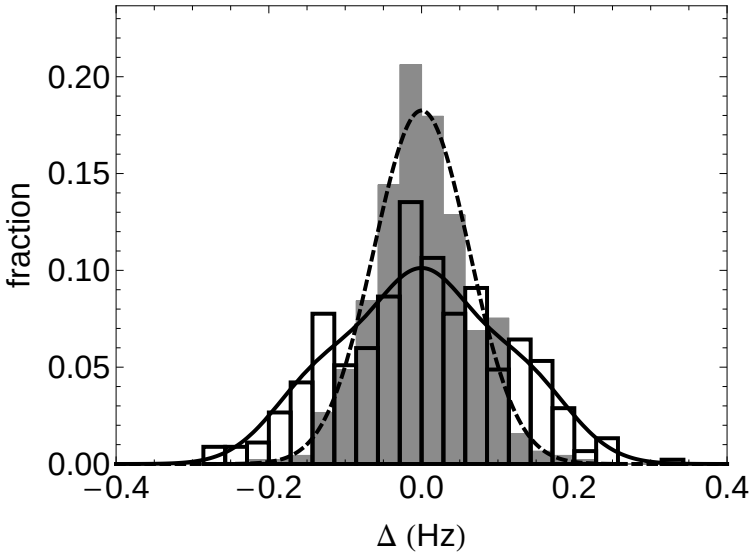

Figure 7.3: The histograms of the axial frequency differences with the control data in gray and the spin flip data in outline. The distributions given by the control standard deviation (dashed) and a spin flip probability of 50% (solid).

7.2 Efficiency and Fidelity

To determine the spin state of the particle, we employ a simple analysis using a threshold difference Δ_t [3]. A spin state is assigned if the measured difference is greater in magnitude than the threshold. The sign of the difference indicates the direction of the spin state.

It is useful to define three properties for a given detection threshold, the efficiency, inefficiency and fidelity. The efficiency E is defined as the fraction of events where the above threshold event leads to a correct identification of the spin state. The inefficiency I is given by the fraction of events where the other spin state caused the

above-threshold event. The fidelity F represents the number of correctly identified events divided by the total number of events.

For a positive threshold magnitude Δ_t, we define four probabilities

$$P_{\downarrow\uparrow}(\Delta_t) = P\int_{\Delta_t}^{\infty} G(\Delta - \Delta_s, \sigma_0)\,\mathrm{d}\Delta, \tag{7.3}$$

$$P_{\uparrow\uparrow}(\Delta_t) = P_{\downarrow\downarrow}(\Delta_t) = (1-P)\int_{\Delta_t}^{\infty} G(\Delta, \sigma_0)\,\mathrm{d}\Delta, \tag{7.4}$$

$$P_{\uparrow\downarrow}(\Delta_t) = P\int_{\Delta_t}^{\infty} G(\Delta + \Delta_s, \sigma_0)\,\mathrm{d}\Delta. \tag{7.5}$$

In this case, the largest probability is given by a spin flip from down to up, expressed by $P_{\downarrow\uparrow}(\Delta_t)$. The probabilities $P_{\downarrow\downarrow}(\Delta_t) = P_{\uparrow\uparrow}(\Delta_t)$ are smaller, corresponding to the probability that a noise fluctuation rather than a spin flip caused the above threshold event. The probability $P_{\uparrow,\downarrow}(\Delta_t)$ is smaller still, representing the chance that a spin flip in the other direction paired with an even larger noise fluctuation caused the above threshold event.

Using these probabilities, the efficiency, E, inefficiency, I, and fidelity, F, are given by

$$E = P_{\downarrow\uparrow}(\Delta_t) + P_{\downarrow\downarrow}(\Delta_t), \tag{7.6}$$

$$I = P_{\uparrow\uparrow}(\Delta_t) + P_{\uparrow\downarrow}(\Delta_t), \tag{7.7}$$

$$F = E/(E+I), \tag{7.8}$$

all three of which are a function of the choice of threshold, Δ_t. To evaluate the spin flip detection, we calculate the efficiency and fidelity as a function of threshold choice. Figure 7.4 shows the results for a spin flip probability of fifty percent (for a saturated drive) and the Allan deviation to 44 mHz (standard deviation, $\sigma_0 = 63$ mHz) to match the measured axial frequency data.

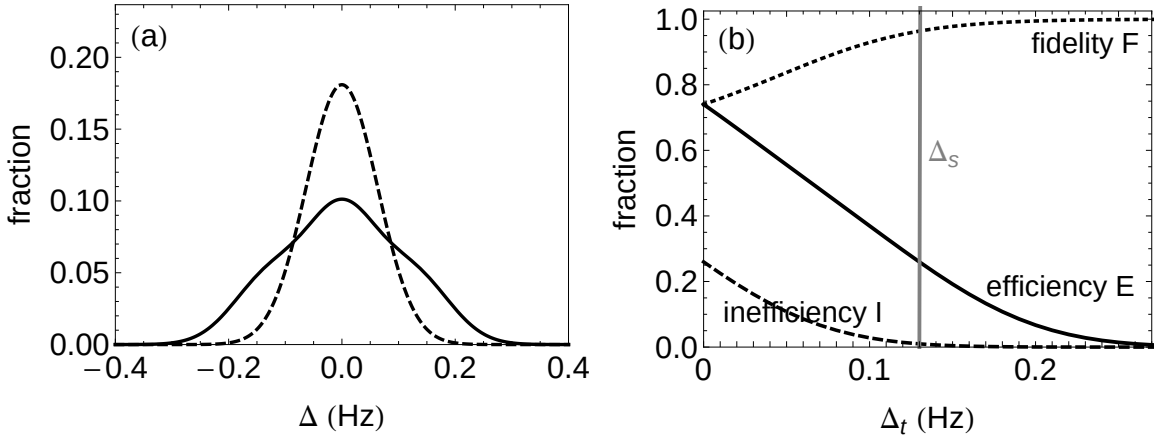

Figure 7.4: (a) Distributions for an off-resonant control spin drive (dashed) and for a saturated spin drive (solid). (b) The corresponding efficiency, inefficiency and fidelity are shown as a function of threshold.

Fast and accurate single spin state detection takes place when both the efficiency and fidelity are near unity. While this initial demonstration experiment does not fully achieve this goal, it is still possible to detect single spin flips with a high fidelity. The caveat to this statement is that a high fidelity F= 96% is realized only for 1 in 4 attempts, for a threshold choice of 130 mHz, the shift from a spin flip. If a lower fidelity suffices the efficiency is much higher, with $F = 0.88$ and $E = 0.48$, for example.

Figure 7.5(a) shows the axial frequency differences for three hours of the 15 hour data set. The gray lines indicate the 130 mHz threshold used to assign spin flips. In Fig. 7.5(b), the spin state after the spin flip is denoted for events above or below the threshold. The fidelity of the assignment is 96% and the efficiency is 26%.

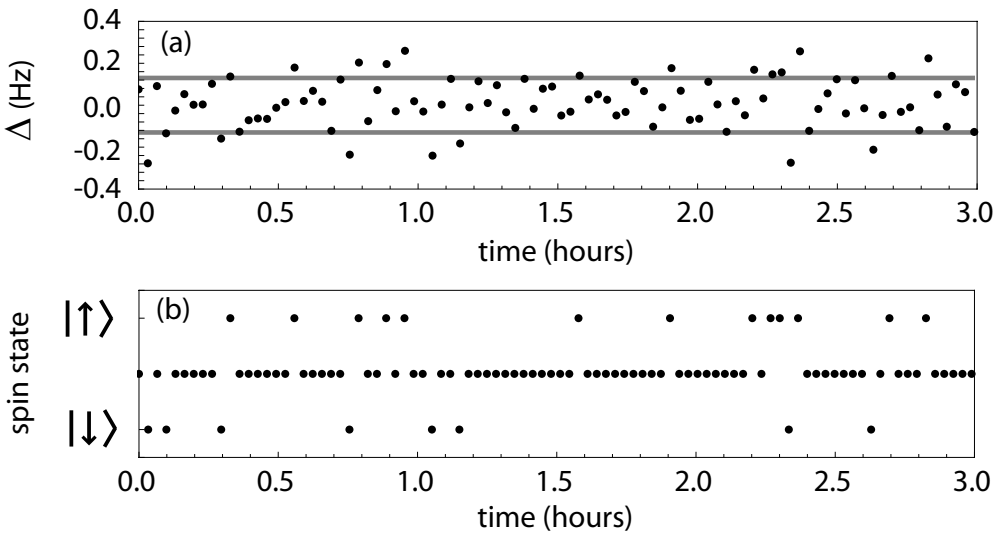

Figure 7.5: (a) Three hours of the axial frequency differences with a resonant, saturated spin drive. The 130 mHz threshold used to assign spin states is shown in gray. (b) Spin states can be identified with a fidelity of 96% for 1 in 4 events.

7.2.1 Correlations of the Differences

To further demonstrate the clear signature of spin flips, we use correlations of the frequency differences. In Fig. 7.6(a), we plot the measured differences $\Delta_2 - \Delta_1$ that come from a detection cycle that produces an above-threshold Δ_1, followed immediately by a second detection cycle that also produces an above-threshold Δ_2. We expect a histogram of these differences to have half of the entries below -$2\Delta_s$ (for a spin that flips from up to down in the first cycle and down to up in the next). The other half of the entries should be above $2\Delta_s$ (for a spin that flips from down to up in the first cycle and up to down in the next). Ideally, there should be no entries between the peaks since correlations near zero would require a spin to switch from either up to down or down to up in both cycles and this is not possible.

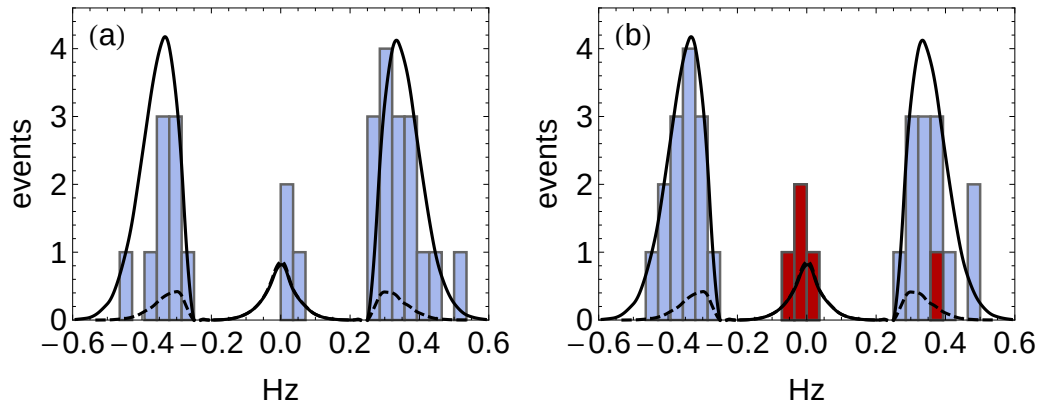

Figure 7.6: (a) The experimental data from the spin state correlation when two consecutive differences are above the threshold. (b) Correlation histogram for the simulation data showing the accidentals in red.

To better quantify the experimental correlation histogram, employ a simulated data set. Using the three Gaussian distributions shown in Fig. 7.1, it is possible to generate a data set of the axial frequency differences while keeping track of the spin state of the particle. This allows us to understand the correlations, test the statistics, and identify so-called accidental spin flip assignments when the spin state is incorrectly assigned because of a noise fluctuation.

To generate a simulated data set, an initial spin state is chosen. If the length of the data set is sufficiently long, in this case 450 measurement sequences like our measured sample, the initial choice does not have a noticeable impact. After the initial choice, there is a 50 percent chance that a spin flip drive will cause a transition. This is simulated using a random number generator to determine the outcome of the drive, which determines the next axial frequency data point. If the spin is flipped, the axial frequency is selected from the corresponding Gaussian distribution. If the spin is not flipped, the axial frequency is selected from Gaussian distribution centered around

zero. This process is iterated to generate the axial frequency data for the simulated data set.

The correlations for the experimental data are shown in Fig. 7.6(a), while the correlations for a simulation data set are in Fig. 7.6(b). The solid line is generated using many more events in the simulation. For the simulation, we can also show so-called accidental events, which occur when at least one of the above threshold events is caused by a large background noise fluctuation and is misidentified as a spin flip. The accidental events for the simulation are shown in red in Fig. 7.6(b). The dashed line shows the expected accidentals, also calculated using the simulation.

The simulation allows us to analyze the statistics of the measured data. First, to check that the number of above threshold events is as expected, given an efficiency of 26% we should see $E^2 450 \approx 30$ events. From the simulation, we see that there are 30 ± 7 events in the side peaks where 2 ± 2 of these events are from accidentals. There are 2 ± 2 events in the central peak from accidentals. The error bars come from running the simulation with 450 events many times and taking the standard deviation of the number of events. In the experimental data, we see 25 events in the side peaks and 3 events in the central peak, in good agreement with the simulation. With this simulation, we have strong evidence that the events we are seeing are the first clear identification of individual spin flips with a single proton.

7.2.2 Application to Quantum Jump Spectroscopy

With the current apparatus and level of axial frequency fluctuations, it should be possible to make a magnetic moment measurement in the precision trap using

quantum jump spectroscopy, opening the path to a measurement at the ppb level. To make such a measurement, the spin state of the particle is first prepared in the analysis trap. We initialize the experiment by determining the spin state from an above-threshold axial frequency difference. After this, the particle would be transferred to the precision trap, where a near-resonant spin flip drive is applied. To determine if this drive has flipped the spin of the particle, the particle would be transferred back to the analysis trap where another spin flip detection cycle is applied to readout the final spin state. By comparing the initial and final spin states, we can determine if the drive in the precision trap was successful in flipping the spin. Repeating this process many times allows us to measure the excitation fraction at each drive frequency, giving a measurement of the spin line shape and hence the spin frequency in the precision trap.

7.3 Adiabatic Fast Passage

A potential improvement of the our current approach is to increase the spin flip probability above 50%. For example, if we could eliminate the background distribution centered around zero, the remaining spin flip identification criterion would be whether the spin was flipped up or down. Adiabatic fast passage (AFP) is a well known technique that can be used to flip the spin state with a probability near 100% [16]. The principle of AFP is that as a drive is swept adiabatically through the transition frequency of the resonance, the population of the state coherently transfers entirely from the initial state to the final state. This technique has been successfully applied to a single electron in a Penning trap [84, 85].

7.3.1 Adiabatic Fast Passage Efficiency and Fidelity

Similar to the previous section, we can calculate the efficiency and fidelity for a given threshold using the expected differences distribution. In the case of AFP, the distribution remains the same as before, but we note that the probability can exceed 1/2. As illustrated in Fig. 7.7, in the limit of $P = 1$, we are left with only two Gaussians centered around $\pm\Delta_s$. The increase in separation by a factor of 2 allows for a lower threshold, increasing the efficiency without compromising the fidelity. For example, using a threshold $\Delta_t = 0$, the efficiency increases to 98% for a high fidelity of 98%.

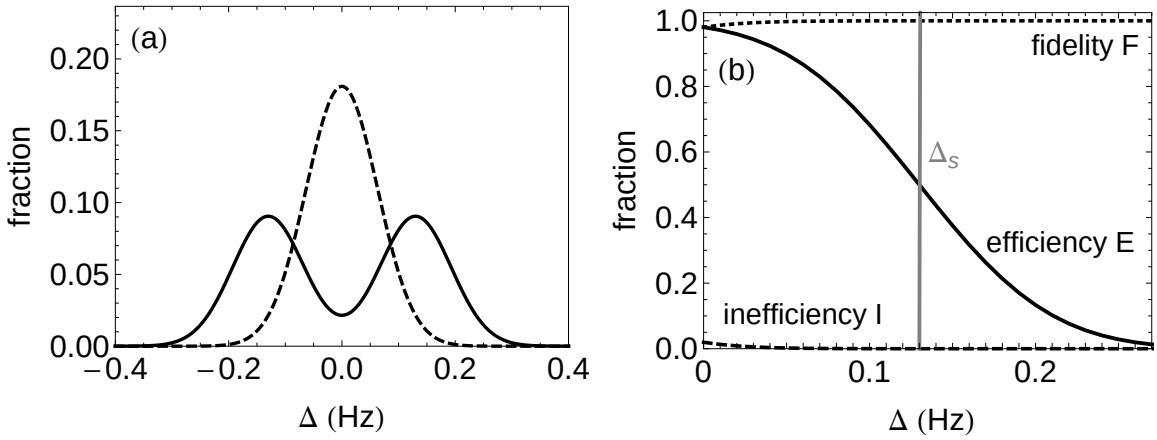

Figure 7.7: (a) Distributions for a control drive (dashed) and for adiabatic fast passage (solid) where there is no central peak in the spin flip data because the transition probability is 100%. (b) The efficiency, inefficiency and fidelity are shown as a function of threshold.

7.3.2 Adiabatic Condition

To successfully implement AFP, the adiabatic condition must be satisfied by sweeping the drive slowly enough to allow the spin population to follow the rotating

field. The adiabatic condition for a linear sweep is determined by the Landau-Zener parameter. Essentially, the sweep rate of the drive has to be slow compared to the Rabi frequency squared [86].

Another possible contributor to the adiabatic condition is the large magnetic gradient in the analysis trap. The gradient by itself is not a particular problem because the high axial frequency ($\sim$1 MHz) is much larger than the spin linewidth ($\sim$25 kHz), so the axial motion effectively averages the magnetic field on the timescale of a spin flip [40]. However, the axial motion is coupled to the amplifier, which causes thermal fluctuations in the amplitude. As a result, the average magnetic field changes as the amplitude changes. The timescale of this change must be slow compared to the sweep rate.

One way to satisfy this limit is to have the axial damping time be much longer than the sweep time. However, the actual criteria may be much less restrictive than this, and numerical modeling is currently being performed to study this limit more carefully. This can be accomplished by detuning the axial frequency from the amplifier by several linewidths of the amplifier. However, this is challenging because to read out the spin flip, the axial frequency, and hence detuning voltage, have to be retuned to better than 50 mHz or so.

Chapter 8

Conclusion

The primary accomplishments of this thesis work were reported in a series of four reports published in Physical Review Letters [1, 2, 3, 4]. These results include the first single particle measurement of the proton magnetic moment [1]. After moving a modified experiment to CERN and loading a single antiproton, we measured the antiproton magnetic moment 680 times more precisely than had been possible [2]. We also reported the observation of a single proton spin flip [3], which opens the path to the ppb level in precision, representing another factor of 10^3 or 10^4 improvement in precision.

8.1 Single Particle Measurement of g_p

Using a single proton, we have performed the first direct measurement of the proton magnetic moment [1]

$$\frac{\mu_p}{\mu_N} = \frac{g_p}{2} = 2.792\,846\,(7)\ [2.5\ \text{ppm}]. \tag{8.1}$$

This result opens the path to both an improved measurement of the proton and antiproton magnetic moment, providing a precise test of CPT invariance.

Our measurement uses a Penning trap to hold a single particle for many months. The magnetic moment measurement is enabled by the high signal-to-noise detection of the proton axial motion with a self-excited oscillator [4]. Using this detection technique, we observe a time-averaged signal that reveals spin flips. Combined with a measurement of the cyclotron frequency by a similar method, we can report the proton magnetic moment as a ratio of the two frequencies

$$\frac{\mu_p}{\mu_N} = \frac{g_p}{2} = \frac{\nu_s}{\nu_c} \, . \tag{8.2}$$

In our research, we profited from parallel work on proton spin flips [9]. This independent effort yielded a proton magnetic moment measurement with a 8.9 ppm precision consistent with our earlier measurement [10] and a simultaneously reported detection of a single proton spin flip [11].

8.2 A 680-fold Improved Measurement of $g_{\bar{p}}$

In the eight months after the proton measurement was reported [1], we modified the apparatus and electrodes to allow for antiproton catching, shipped and installed the experiment at CERN, and performed the antiproton magnetic moment measurement. The result is the first single particle measurement of the antiproton magnetic moment

$$\frac{\mu_{\bar{p}}}{\mu_N} = -\frac{g_{\bar{p}}}{2} = -2.792\,845\,(12)\ [4.4\ \text{ppm}]. \tag{8.3}$$

The precision is improved by a factor of 680 [2] over previous methods, for which the precision has remained essentially unchanged for 25 years [5, 6].

Initial work at CERN's Antiproton Decelerator focused on slowing, catching and loading a single antiproton at 4 K from the 5 MeV beam. We then performed the antiproton measurement using techniques developed for the proton work, overcoming the challenges of making a precision measurement in the AD accelerator hall. The experiment is currently installed and operational at CERN, and work is being performed with protons to prepare for the 2014 antiproton beam run.

Comparing the proton and antiproton magnetic moment measurements yields a new precision test of CPT invariance, providing a result consistent with the CPT theorem prediction that the magnetic moments have the same magnitude and opposite sign:

$$\mu_{\bar{p}}/\mu_p = -1.000\,000\,(5)\ [5.0\ \text{ppm}], \tag{8.4}$$

$$\mu_{\bar{p}}/\mu_p = -0.999\,999\,2\,(44)\ [4.4\ \text{ppm}]. \tag{8.5}$$

The first is a direct comparison using the μ_p measured using the same trap electrodes as the antiproton measurement [1]. The second comparison is indirect, using the more precise μ_p deduced indirectly from three measurements (currently not possible with $\bar{p}$) and two theoretical corrections [7, 8].

8.3 Observation of a Single Spin Flip

In addition to making the magnetic moment measurements at the ppm precision, we have demonstrated the ability to prepare and measure the spin state by detecting a

single spin flip [3] (An independent observation was published at the same time [11]). This opens the path to making improved magnetic moment measurements of both the proton and antiproton with precision at the ppb level, representing a further improvement of 10^3 or 10^4.

Bibliography

[1] J. DiSciacca and G. Gabrielse, Phys. Rev. Lett. **108**, 153001 (2012).

[2] J. DiSciacca, M. Marshall, K. Marable, G. Gabrielse, S. Ettenauer, E. Tardiff, R. Kalra, D. W. Fitzakerley, M. C. George, E. A. Hessels, C. H. Storry, M. Weel, D. Grzonka, W. Oelert, and T. Sefzick, Phys. Rev. Lett. **110**, 130801 (2013).

[3] J. DiSciacca, M. Marshall, K. Marable, and G. Gabrielse, Phys. Rev. Lett. **110**, 140406 (2013).

[4] N. Guise, J. DiSciacca, and G. Gabrielse, Phys. Rev. Lett. **104**, 143001 (2010).

[5] A. Kreissl, A.D. Hancock, H. Koch, Th. Köehler, H. Poth, U. Raich, D. Rohmann, A. Wolf, L. Tauscher, A. Nilsson, M. Suffert, M. Chardalas, S. Dedoussis, H. Daniel, T. von Egidy, F.J. Hartmann, W. Kanert, H. Plendl, G. Schmidt, and J.J. Reidy, Z. Phys. C: Part. Fields **37**, 557 (1988).

[6] T. Pask, D. Barna, A. Dax, R.S. Hayano, M. Hori, D. Horváth, S. Friedrich, B. Juhász, O. Massiczek, N. Ono, A. Sótér, and E. Widmann, Phys. Lett. B **678**, 55 (2009).

[7] P. Frank Winkler, Daniel Kleppner, Than Myint, and Frederick G. Walther, Phys. Rev. A **5**, 83 (1972).

[8] Peter J. Mohr and Barry N. Taylor, Rev. Mod. Phys. **72**, 351 (2000).

[9] S. Ulmer, C. C. Rodegheri, K. Blaum, H. Kracke, A. Mooser, W. Quint, and J. Walz, Phys. Rev. Lett. **106**, 253001 (2011).

[10] C .C. Rodegheri, K. Blaum, H. Kracke, S. Kreim, A. Mooser, W. Quint, S. Ulmer, and J. Walz, New Journal of Physics **14**, 063011 (2012).

[11] A. Mooser, H. Kracke, K. Blaum, S. A. Bräuninger, K. Franke, C. Leiteritz, W. Quint, C. C. Rodegheri, S. Ulmer, and J. Walz, Phys. Rev. Lett. **110**, 140405 (2013).

[12] R. Frisch and O. Stern, Z. Phys. A: Hadrons Nucl. **85**, 17 (1933).

[13] I. Estermann and O. Stern, Z. Phys. A: Hadrons Nucl. **85**, 4 (1933).

[14] Hans G. Dehmelt, Nobel Lecture: Experiments with an Isolated Subatomic Particle at Rest, 1989.

[15] J. M. B. Kellogg, I. I. Rabi, N. F. Ramsey, and J. R. Zacharias, Phys. Rev. **56**, 728 (1939).

[16] F. Bloch, W. W. Hansen, and Martin Packard, Phys. Rev. **69**, 127 (1946).

[17] E. M. Purcell, H. C. Torrey, and R. V. Pound, Phys. Rev. **69**, 37 (1946).

[18] H. M. Goldenberg, D. Kleppner, and N. F. Ramsey, Phys. Rev. Lett. **5**, 361 (1960).

[19] Than Myint, Daniel Kleppner, Norman F. Ramsey, and Hugh G. Robinson, Phys. Rev. Lett. **17**, 405 (1966).

[20] Peter J. Mohr, Barry N. Taylor, and David B. Newell, Rev. Mod. Phys. **84**, 1527 (2012).

[21] D. Hanneke, S. Fogwell, and G. Gabrielse, Phys. Rev. Lett. **100**, 120801 (2008).

[22] J. Verdú, S. Djekić, S. Stahl, T. Valenzuela, M. Vogel, G. Werth, T. Beier, H.-J. Kluge, and W. Quint, Phys. Rev. Lett. **92**, 093002 (2004).

[23] G. Lüders, Ann. Phys. **2**, 1 (1957).

[24] C. S. Wu, E. Ambler, R. W. Hayward, D. D. Hoppes, and R. P. Hudson, Phys. Rev. **105**, 1413 (1957).

[25] J. H. Christenson, J. W. Cronin, V. L. Fitch, and R. Turlay, Phys. Rev. Lett. **13**, 138 (1964).

[26] T. D. Lee and C. N. Yang, Phys. Rev. **104**, 254 (1956).

[27] L. D. Landau, Nuc. Phys. **3**, 127 (1957).

[28] A. Alavi-Harati *et al.*, Phys. Rev. Lett. **83**, 22 (1999).

[29] B. Aubert *et al.*, Phys. Rev. Lett. **87**, 091801 (2001).

[30] Makoto Kobayashi and Toshihide Maskawa, Progress of Theoretical Physics **49**, 652 (1973).

[31] A. D. Dolgov and Ya. B. Zeldovich, Rev. Mod. Phys. **53**, 1 (1981).

[32] A. D. Sakharov, J. of Exp. and Th. Phys. **5**, 24 (1967).

[33] J. Beringer *et al.*, Phys. Rev. D **86**, 010001 (2012).

[34] R. Carosi *et al.*, Phys. Lett. B **237**, 303 (1990).

[35] G. Gabrielse, A. Khabbaz, D. S. Hall, C. Heimann, H. Kalinowsky, and W. Jhe, Phys. Rev. Lett. **82**, 3198 (1999).

[36] R. S. Van Dyck, Jr., P. B. Schwinberg, and H. G. Dehmelt, Phys. Rev. Lett. **59**, 26 (1987).

[37] N. Guise, Ph.D. thesis, Harvard University, 2010.

[38] G. Gabrielse, X. Fei, K. Helmerson, S. L. Rolston, R. L. Tjoelker, T. A. Trainor, H. Kalinowsky, J. Haas, and W. Kells, Phys. Rev. Lett. **57**, 2504 (1986).

[39] G. Gabrielse, X. Fei, L. A. Orozco, R. L. Tjoelker, J. Haas, H. Kalinowsky, T. A. Trainor, and W. Kells, Phys. Rev. Lett. **63**, 1360 (1989).

[40] L. S. Brown and G. Gabrielse, Rev. Mod. Phys. **58**, 233 (1986).

[41] G. Gabrielse, L. Haarsma, and S. L. Rolston, Intl. J. of Mass Spec. and Ion Proc. **88**, 319 (1989), ibid. 93:, 121 (1989).

[42] G. Gabrielse, X. Fei, L. A. Orozco, R. L. Tjoelker, J. Haas, H. Kalinowsky, T. A. Trainor, and W. Kells, Phys. Rev. Lett. **65**, 1317 (1990).

[43] D. J. Wineland, C. Monroe, W. M. Itano, D. Leibfried, B. E. King, and D. M. Meekhof, J. Res. Natl Inst. Stand. Technol. **103**, 259 (1998).

[44] H. Häffner, N. Hermanspahn, H.-J. Kluge, W. Quint, S. Stahl, J. Verdú, and G. Werth, Phys. Rev. Lett. (2000).

[45] H. Häffner, T. Beier, S. Djekić, N. Hermanspahn, H.-J. Kluge, W. Quint, S. Stahl, J. Verdú, T. Valenzuela, and G. Werth, Eur. Phys. J. D **22**, 163 (2003).

[46] G. Werth, J. Alonso, T. Beier, K. Blaum, S. Djekic, H. Häffner, N. Hermanspahn, W. Quint, S. Stahl, J. Verdú, T. Valenzuela, and M. Vogel, Int. J. Mass Spectrom. **251**, 152 (2006).

[47] R. L. Tjoelker, Ph.D. thesis, Harvard University, 1990.

[48] B. Odom, D. Hanneke, B. D'Urso, and G. Gabrielse, Phys. Rev. Lett. **97**, 030801 (2006).

[49] B. Odom, Ph.D. thesis, Harvard University, 2004.

[50] D. Wineland, P. Ekstrom, and H. Dehmelt, Phys. Rev. Lett. **31**, 1279 (1973).

[51] D. J. Wineland and H. G. Dehmelt, J. Appl. Phys. **46**, 919 (1975).

[52] B. D'Urso, Ph.D. thesis, Harvard University, 2003.

[53] H. Dehmelt, W. Nagourney, and J. Sandberg, Proc. Natl. Acad. Sci. USA **83**, 5761 (1986).

[54] B. D'Urso, R. Van Handel, B. Odom, D. Hanneke, and G. Gabrielse, Phys. Rev. Lett. **94**, 113002 (2005).

[55] B. D'Urso, B. Odom, and G. Gabrielse, Phys. Rev. Lett. **90**, 043001 (2003).

[56] G. Gabrielse, D. Phillips, W. Quint, H. Kalinowsky, G. Rouleau, and W. Jhe, Phys. Rev. Lett. **74**, 3544 (1995).

[57] D. J. Wineland, J. Appl. Phys. **50**, 2528 (1979).

[58] T. A. Savard, K. M. O'Hara, and J. E. Thomas, Phys. Rev. A **56**, R1095 (1997).

[59] Q. A. Turchette, Kielpinski, B. E. King, D. Leibfried, D. M. Meekhof, C. J. Myatt, M. A. Rowe, C. A. Sackett, C. S. Wood, W. M. Itano, C. Monroe, and D. J. Wineland, Phys. Rev. A **61**, 063418 (2000).

[60] *The 1988 ARRL Handbook for the Radio Amateur*, edited by Mark J. Wilson (American Radio Relay League, Connecticut, 1988).

[61] Jaroslaw Labaziewicz, Yufei Ge, Paul Antohi, David Leibrandt, Kenneth R. Brown, and Isaac L. Chuang, Phys. Rev. Lett. **100**, 013001 (2008).

[62] Guang Hao Low, Peter F. Herskind, and Isaac L. Chuang, Phys. Rev. A **84**, 053425 (2011).

[63] N. Daniilidis, S. Narayanan, S. A. Möller, R. Clark, T. E. Lee, P. J. Leek, A. Wallraff, St. Schulz, F. Schmidt-Kaler, and H. Häffner, New Journal of Physics **13**, 013032 (2011).

[64] D. A. Hite, Y. Colombe, A. C. Wilson, K. R. Brown, U. Warring, R. Jördens, J. D. Jost, K. S. McKay, D. P. Pappas, D. Leibfried, and D. J. Wineland, Phys. Rev. Lett. **109**, 103001 (2012).

[65] F. Bloch and A. Siegert, Phys. Rev. **57**, 522 (1940).

[66] L. S. Brown, Phys. Rev. Lett. **52**, 2013 (1984).

[67] L. S. Brown, Ann. Phys. **159**, 62 (1985).

[68] D. Hanneke, Ph.D. thesis, Harvard University, 2007.

[69] G. Gabrielse, Adv. At. Mol. Opt. Phys. **50**, 155 (2005).

[70] G. Gabrielse, N. S. Bowden, P. Oxley, A. Speck, C. H. Storry, J. N. Tan, M. Wessels, D. Grzonka, W. Oelert, G. Schepers, T. Sefzick, J. Walz, H. Pittner, T. W. Hänsch, and E. A. Hessels, Phys. Rev. Lett. **89**, 213401 (2002).

[71] P. Yesley, Ph.D. thesis, Harvard University, 2001.

[72] James F. Ziegler, M.D. Ziegler, and J.P. Biersack, Nuc. Inst. and Meth. B **268**, 1818 (2010).

[73] J. Estrada, Ph.D. thesis, Massachusetts Institute of Technology, 2002.

[74] G. Gabrielse, N. S. Bowden, P. Oxley, A. Speck, C. H. Storry, J. N. Tan, M. Wessels, D. Grzonka, W. Oelert, G. Schepers, T. Sefzick, J. Walz, H. Pittner, and E. A. Hessels, Phys. Lett. B **548**, 140 (2002).

[75] A. Speck, Ph.D. thesis, Harvard University, 2005.

[76] D. H. E. Dubin and T. M. O'Neil, Rev. Mod. Phys. **71**, 87 (1999).

[77] D. S. Hall, Ph.D. thesis, Harvard University, 1997.

[78] S. L. Rolston and G. Gabrielse, Hyperfine Interact. **44**, 233 (1988).

[79] L. Spitzer, Jr., *Physics of Fully Ionized Gases* (Dover, New York, 1962).

[80] David K. Geller and Jon C. Weisheit, Physics of Plasmas **4**, 4258 (1997).

[81] G. Gabrielse and J. Tan, J. Appl. Phys. **63**, 5143 (1988).

[82] J. N. Tan, Ph.D. thesis, Harvard University, 1992.

[83] W. Quint, J. Alonso, S. Djekić, H.-J. Kluge, S. Stahl, T. Valenzuela, J. Verdú, M. Vogel, and G. Werth, Nucl. Inst. Meth. Phys. Res. B **214**, 207 (2004).

[84] G. Gabrielse, H. Dehmelt, and W. Kells, Phys. Rev. Lett. **54**, 537 (1985).

[85] C. H. Tseng, D. Enzer, G. Gabrielse, and F. L. Walls, Phys. Rev. A **59**, 2094 (1999).

[86] C.J Hardy, W.A Edelstein, and D Vatis, J. Magn. Reson. **66**, 470 (1986).